Dissertation

submitted to the
Combined Faculty for the Natural Sciences and for Mathmatics
of the Ruperto-Carola University of Heidelberg, Germany
for the degree of
Doctor of Natural Sciences

by
Diplom-Physikerin Miriam A. Schwentker
born 13.07.1977 in Augsburg

oral exam: **06.06.2007**

Gelänge uns doch
der Griff aus dem Dunkel
nach den wirklichen Dingen!
(Heinz Czechowski)

Parallelized Ground State Depletion

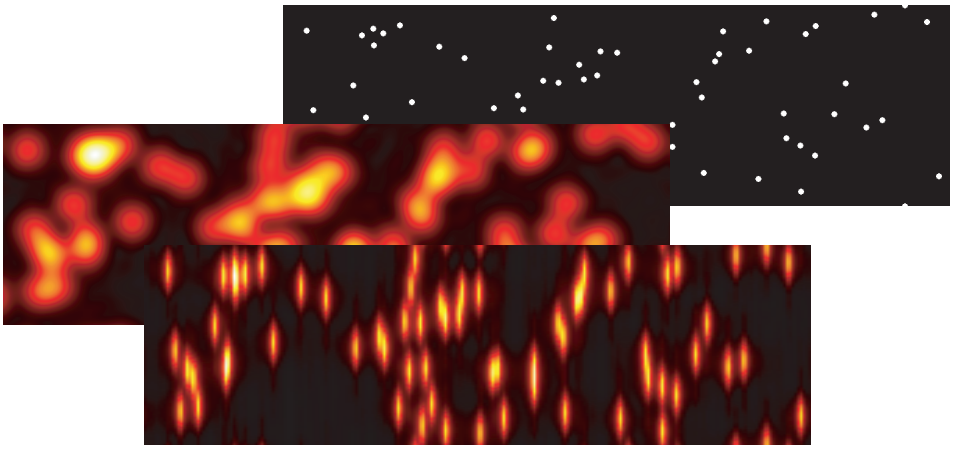

Gutachter: Prof. Dr. Stefan W. Hell
Prof. Dr. Josef Bille

Abstract

RESOLFT was introduced to break the limited resolution in fluorescence microscopy given by thephysical limit of diffraction. RESOLFT needs saturable fluorescence depletion and illumination with spatial regions of zero intensity. Improvements in RESOLFT are still essential since (i) photobleaching restricts the use of large intensities obligate for high resolution, (ii) long acquisition times emerge from single-point scanning, and (iii) RESOLFT puts ahead special requirements on the dye´s photophysical properties. To counteract these problems, this work presents a RESOLFT-type microscope implementing parallelized ground state depletion (GSD). Parallelization allows rather fast image acquisition applying structured illumination combined with widefield detection on a camera. The depletion of the fluophore´s ground state, and thus the fluorescence, is realized using a pump-probe illumination scheme. To increase photostability, the sample was evacuated and cooled to approximately $80\ K$. Since the population of the triplet state is an intrinsic property of almost every dye and is enhanced by evacuation and low temperatures, parallelized GSD is generally applicable to a wide range of fluorescent markers. Applying parallelized RESOLFT an enhancement in resolution was proven for a bead sample as well as inside a cell. Parallelized GSD microscopy further prevents photostress on both fluorescent label and sample, since it encounters moderate illumination intensities $< kW/cm^2$.

Zusammenfassung

Das RESOLFT-Konzept wurde entwickelt, um die Auflösungsgrenze in der Fluoreszenzmikroskopie zu überwinden. RESOLFT benötigt einen sättigbare Fluoreszenzauslöschungmechanismus und eine räumliche Beleuchtung mit dunklen Bereichen. Verbesserungen sind notwendig, da (i) starkes Photobleichen den Einsatz hoher Laser-Intensitäten verbietet, die jedoch für eine hohe Auflösung notwendig sind, (ii) die bisherigen RESOLFT-Verfahren Laserraster Methoden einsetzen und lange Aufnahmezeiten bedingen, und (iii) spezielle Anforderungen an die eingesetzten Farbstoffe gesetzt sind. Um diese Problemen zu beheben, wurde in der vorliegenden Arbeit ein neues RESOLFT-Mikroskop entwickelt, welches den sättigbaren Fluoreszenunterdrückungsprozeß durch Entleerung des Grundzustandes über die Bevölkerung des Tripletzustandes realisiert. Die Bildaufnahme ist durch die parallelisierte Aufnahme mit Hilfe von strukturierter Beleuchtung und großflächiger Fluoreszenzdetektion über eine Kamera wesentlich beschleunigt. Die Entleerung des Grundzustandes eines Farbstoffmoleküles und Löschung der Fluoreszenz geschieht durch ein Zwei-Puls Beleuchtungsschema. Um die Photostabilität der Farbstoffe zu erhöhen, wurde die Probe evakuiert und auf $80\ K$ gekühlt. Da Tripletbevölkerung eine Eigenschaft fast jeden Farbstoffs ist und durch Kühlung verstärkt wird, ist das vorgestellte RESOLFT-Konzept weitreichend einsetzbar. Die vorgestellte Mikroskopiemethode erzielte Auflösungen unterhalb der Beugungsgrenze sowohl für punktförmige Farbstoffproben, als auch innerhalb von Zellen. Die dabei verwendeten Intensitäten von $< kW/cm^2$ üben kaum Photostreß auf die Probe aus.

Contents

1 Introduction

During the last centuries microscopy has increasingly become an important tool in many different scientifc areas, especially in the field of biology. The most commonly used microscopy technique in biology is optical microscopy, using fluorescent markers to identify certain structures or proteins. One demand on microscopy is high resolution - that is, the smallest distance at which two objects can still be resolved. In 1873 Ernst Abbe uncovered the physical limit of resolution (the so-called *diffraction limit*), which is approximately half of the wavelength of the light used for imaging [1]. With the use of visible light ($400 - 800\,nm$), a far-field microscope cannot discern alike objects less than $\approx 200\,nm$ apart. As most of the interesting cellular features are in the range of a few nm there is a need for higher resolution. Because of phototoxicity it is not feasible to reduce the applied wavelength further to the ultraviolet (wavelength $< 350\,nm$, [2]) for resolution enhancement.

The diffraction limit derived by Abbe was perceived as being fixed for a long time, but throughout the last century different approaches in high resolution microscopy have been pursued, e.g. electron microscopy (EM) [3], atomic force microscopy (AFM) [4] or scanning near-field optical microscopy (SNOM) [5]. But all these methods have features, which reduce their applicability to life sciences. EM samples have to be prepared laboriously, that is dehydrated, cut in very thin slices and even coated with metal, because of the high absorption of electrons. Three dimensional images from cellular compounds are possible, but need extensive resonstruction using a PC due to the poor labelling possibilities in comparison to fluorescence microscopy. AFM is restricted to surfaces and very much depends on the interactions between scanning tip and sample. SNOM takes advantage of the broad range of fluorescent markers, but is restricted to surfaces as well. All these techniques feature very high resolution in the range of few nm, but their preparation is very elaborate and does not allow live cell imaging, and three-dimensional imaging is hardly possible without huge effort.

Eventually, the interest in biological microscopy is the imaging of living cells with high resolution and good contrast. Therefore, fluorecence micropscopy is still the best candidate, partly because of the range of fluorescent labels, from organic dyes to fluorescent proteins. Confocal microscopy even allows very fast acquisition of three dimensional images of a cellular structures ([6]). The issue of overcoming the diffraction barrier is addressed by a new concept using **R**eversible **S**aturable **O**ptical (**F**luorescence) **T**ransitions, **RESOLFT** ([7], [8], [9], [10]).

The RESOLFT technique exploits a saturable nonlinear relationship between illumination light and resulting fluorescence, using a transition between two states one of which should be fluorescing. This light-driven saturable transition is used to restrict fluorescence emission to spots or lines of minimized size. So far, RESOLFT has been implemented

in **ST**imulated **E**mission **D**epletion (STED) microscopy ([11],[12], [13]), photoswitchable chromophores ([14]) and photoswitchable proteins ([15], [16]). Another saturable process is **G**round **S**tate **D**epletion (GSD) as theortically suggested by Hell et.al. ([17]) which will be used in this project. Contrary to previously reported sub-diffraction resolution techniques, it relies both on modest continuous wave (CW) illumination intensities and on standard fluorescent markers. However, it is challenged by photobleaching, which accounts for the fact, that, although GSD microscopy has been suggested over ten years ago ([17]), experimental realization has not been pursued. The present work discovers optimized conditions for GSD microscopy realizing its experimental implementation. Large illumination intensities and thus high saturation of fluorescence depletion is made possible by evacuating and cooling of the sample, which is known to reduce bleaching ([18]). A setup will be adapted allowing subdiffraction fluorescence imaging on evacuated and frozen samples.

Usually RESOLFT is applied to decrease the size of the confocal scanning spot in one, two or even three dimenstions. To cover the same image area as in regular confocal micrsocopy RESOLFT-microscopy has to perform comparativey more scanning steps, each with a longer dwell time, since the reduced spot covers a smaller region, eliciting less fluorescence signal. To counteract the longer image acquisition time, parallelization by structured illumination and camera-based detection will be introduced.

The presented work depicts the experimental implementation of parallelized GSD at low temperatures. The following chapter will explain the concept of resolution enhancement using RESOLFT and outline the principle of GSD. The third chapter introduces the experimental realization and challenges of parallelization and imaging at low temperatures. Chapter four describes the experimental setup and and outlines a resolution enhancement of a factor of up to 3 with the present setup of parallelized GSD at low temperatures.

2 The RESOLFT concept

In this chapter the nature of the diffraction limit will be explained and how RESOLFT allows imaging with greater detail than imposed by this diffraction limit. Ground state depletion will be presented as one method for RESOLFT imaging, which was used in this project, and the general problems of the technique will be adressed.

2.1 Resolution Enhancement with RESOLFT

Every image taken of an object using light misses small details of that object, either telescopic images of the stars, photographs of our surroundings or micrsopsopic images of cells – even with perfect lenses. This is due to the wave nature of light. Imaging light emitted from one point does not result in one single point but a blurred spot. An object can be taken as a series of point-like light emitters, resulting in a series of blurred spots, and therefore the image of an object will be blurred and lack details.

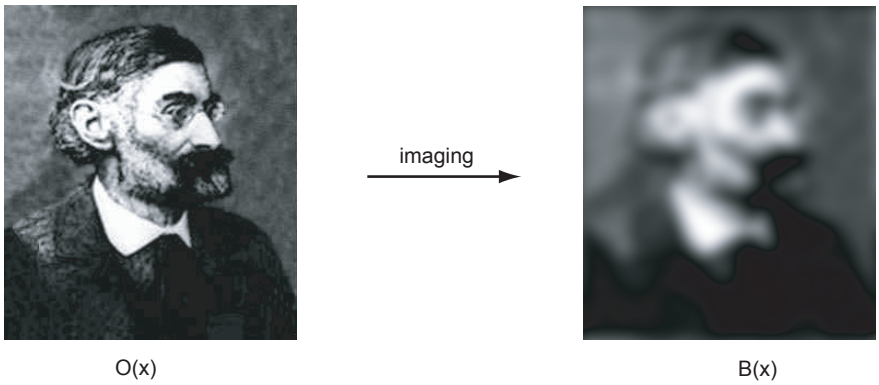

Figure 2.1: **Blurring due to Imaging** Image of Abbe (left) is blurred due to imaging (right) and therefore lacks detail in comparison to the original object. In mathmatical terms the object $O(x)$ is convolved with the point spread funtion $h(x)$ to yield the image $B(x)$.

The resolution describes the ability of an optical system - telescope, photographic camera or microscope - to image details of the original object. The higher the resolution the more details can be seen in the image. At the end of the 19th century Ernst Abbe found a relationship between the size Δx of the blurred spot emitted by a point source and the wavelength of the emitted light [1]. The full width at half maximum (FWHM) of that blurred spot was later quantified by Lord Rayleigh and is still known as the *Abbe diffraction limit* (see appendix A.2.1 for derivation):

$$\Delta x = 0.61 \frac{\lambda}{n \cdot sin\alpha} \tag{2.1}$$

λ is the wavelength of the emitted light, n the refractive index of the material between imaging lens and sample (immersion medium) and α half the angle under which the light emitted by the single spot is collected. The product $n \cdot sin\alpha$ is called the numerical apterure NA of the imaging optics. The spatial distribution of the light emitted by a point-like source and imaged by an optical system is called the **P**oint **S**pread **F**unction (PSF) and is characteristic to the optical system.

As described before, the object can be seen as a series of point-like emitters, each of which is imaged as a blurred spot (the PSF) and the final images results of an assembly of these blurred spots. In mathmatical terms this mechanism is described as a convolution between the spatial (x) distribution of the object $O(x)$ and the PSF $h(x)$. The final image $B(x)$ is:

$$B(x) = O(x) \otimes h(x) \tag{2.2}$$

In biology, far-field fluorescence microscopy is most commonly used for imaging. Structures or molecules to be imaged are specifically stained with a fluorescence marker, for example an organic dye or a fluorescent protein, whose fluorescence emission is excited (e.g. by a laser), and the fluorescence is detected by the optical system and a photon detector. Far-field fluorescence microscopy not only allows imaging of surfaces (as in electron microscopy or near-field optical microscopy) but within a three-dimensional object with three-dimensional image reconstruction.

The object that is imaged is the distribution of dye molecules within the sample, that is the density of dye molecules $\rho_{dye}(x)$ depending on the spatial position x. At moderate excitation intensities $I(x)$ the fluorescence $F(x)$ emitted from one dye molecule is proportional to $I(x)$ and the resulting fluorescence $S(x)$ from the sample is the product of the fluorescence signal $F(x)$, detected from one dye molecule, and the dye distribution $\rho_{dye}(x)$:

$$\begin{aligned} S(x) &= \rho_{dye}(x) \cdot F(x) \\ &\propto \rho_{dye}(x) \cdot I(x) \\ &\text{with} \quad F(x) \propto I(x) \end{aligned} \tag{2.3}$$

The wavelength determining the size of the PSF in equation 2.1 is the wavelength of the fluorescence light λ_{em}, which due to the Stokes shift is larger than the excitation wavelength λ_{ex}. To avoid phototoxicity the excitation wavelength λ_{ex} should not be $< 400\,nm$. The best objective lenses used in modern light microscopy allow a semi-aperture angle of $\alpha \approx 73°$. This leads to a highest resolution (the FWHM of the PSF) of ≈ 170 nm (and $NA = 1.5$).

The resolution in confocal microscopy is slightly higher than in standard widefield microscopy. In the latter the sample is illuminated homogeneously and the resolution is directly linked to the Abbe diffraction limit with λ_{em}. In confocal microscopy (see figure 2.2) the sample is scanned with a highly focused beam and the final image is reconstructed from the

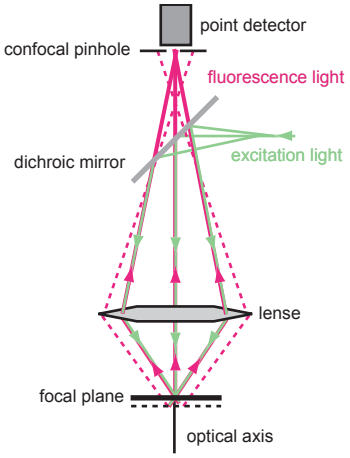

Figure 2.2: **Principle of a confocal microscope.** Focused light excites fluorescence in the sample. The fluorescence light is guided through a pinhole in the confocal plane onto a point detector. The pinhole hinders light that stems from out of the focal plane to fall onto the detector, thus increasing the resolution along the optical axis. By scanning the sample with the combination of focused beam and pinhole, a whole image can be reconstructed from the signals on the point detector.

signal detected for each scanning point. The fluorescence emitted by the sample is guided through a pinhole in the plane confocal to the sample plane onto a photon counting detector. From the signal on the detector the final image can be reconstructed on a computer. Light emitted from above or below the sample plane will be blocked by the pinhole (see figure 2.2). Therefore, only light emitted from the focal plane will be collected by the point detector, which leads to an enhanced resolution in the direction of z (along the optical axis). The resolution in the direction of x is determined by the illumination PSF and the detection PSF and is therefore slightly higher than the resolution of a widefield illuminated microscope.

The resolution given by the diffraction limit was achieved by the elimination of aberrations in lenses at the end of the 19th century. However, the need for higher resolution in biological imaging has only become more and more since, e.g. to resolve sub-cellular structures or protein distributions. In the early 1990s, Hell and coworkers presented a new concept for resolution beyond the diffraction limit ([11], [17] and [19]) now known as **R**eversible **S**aturable **O**ptical (**F**luorescence) **T**ransitions microscopy (**RESOLFT**, [8]). Within the RESOLFT approach high resolution is achieved by reducing the area of possible fluorescence emission below the diffraction limit by applying saturable optical transitions.

RESOLFT can use different mechanisms. In general it involves two states S_F and S_D in the dye molecules, one of which is fluorescent (S_F) and the other non-fluorescent (dark, S_D)[1]. The prerequisites for RESOLFT are:

1. A system of two (or more) states $S_F \leftrightarrow S_D$ with reversible transitions.

[1]The second state S_D can as well be fluorescent, but needs to be of a different color compared to the fluorescence color of S_F, i.e. its fluorescence is not detected by the optical system.

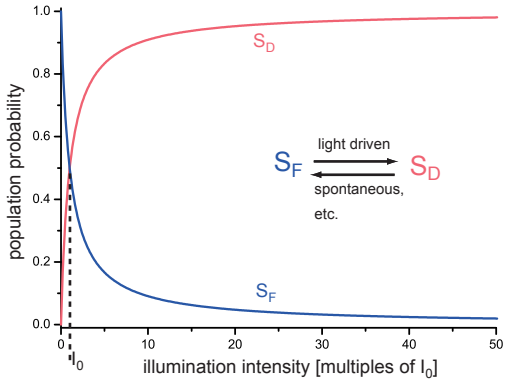

Figure 2.3: **Population curves of the fluorescent state S_F and the dark state S_D.** At zero illumination intensity $I_{FD} = 0$ all molecules are in state S_F, with increasing intensity state S_D is populated and state S_F is depopulated. The intensity at which both states are equally populated is defined as saturation intensity I_0.

2. One transition between S_F and S_D needs to be light driven.

3. The light driven transition needs to be saturable.

For example the transition $S_F \rightarrow S_D$ is light driven (with intensity I_{FD} and wavelength λ_{FD}) and reversible. $S_F \rightarrow S_D$ will be called the depletion transition, as the state S_D is non-fluorescent. The reverse transition $S_D \rightarrow S_F$ does not necessarily have to be light driven, but can be chemical, spontaneous or thermally driven. An example for the saturation behaviour of the transition from S_F to S_D is depicted in figure 2.3. Increasing the intensity of the illumination leads to a higher population of S_D and a depopulation of S_F (see appendix A.2.2 for derivation of the rate equations and population curves). The fluorescence emitted by the dye molecules due to additional illumination with excitation light I_{ex} directly follows the population of S_F as only that state is fluorescent.

To achieve resolution enhancement with this saturable process, the depletion light needs to have a spatial distribution featuring a local zero. One possible distribution is depicted in figure 2.4 with two maxima in a certain distance and a minimum with zero intensity in between. The zero intensity distribution is diffraction limited as well, thus the FWHM of the minimum is larger than $\geq \cdot \Delta x_{FD}$, with Δx_{FD} determined by equation 2.1 with the wavelength λ_{FD} of the depletion light. Illumination of the dye molecules with this distribution of depletion light (I_{FD} and λ_{FD}) will drive the molecules in the region of the maxima into the dark state S_D. Molecules located at the local zero reside in the fluorescent state S_F. Increasing the depletion intensity enhances this effect, broadening the area with the molecules in state S_D, reducing the area with molecules in state S_F and steepening the slopes between those two regions. Thus the area with fluorescent molecules in between the maxima (see figure 2.4 B) and therefore the area from which fluorescence can be emitted is effectively reduced. When this area of the sample is excited by a confocal diffraction limited scanning spot (see green gaussian-like peak in part (A) of this figure), with the confocal maximum overlaying the zero of the structured illumination light, fluorescence can only be emitted by the dye molecules in the small region around the zero. This fluorescence is guided through

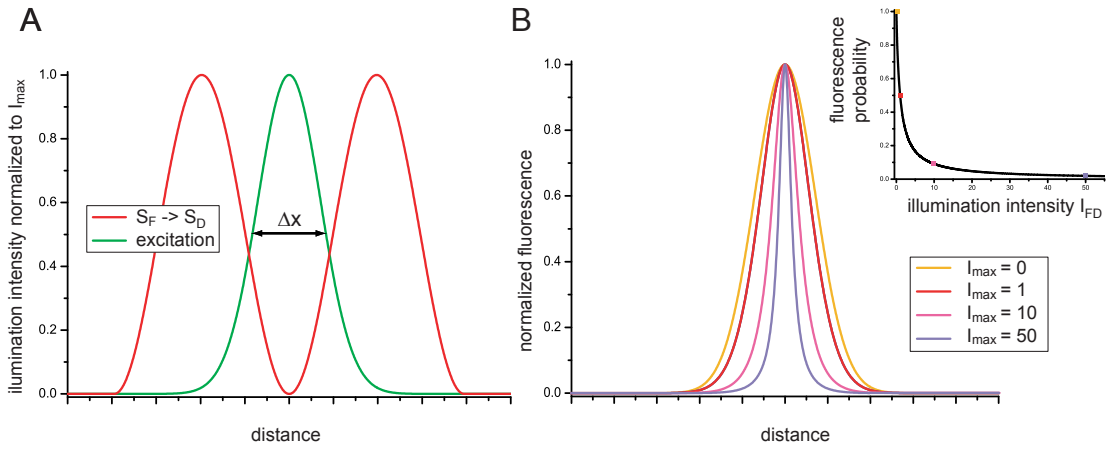

Figure 2.4: **Effect of structured depletion light on emitted fluorescence.** A: Overlay of confocal excitation spot in green and depletion light in red featuring a local zero in the center. B: resulting fluorescence after illumination with excitation spot and depletion light, inlay shows a saturated depletion curve, the area from which fluorescence is emitted gets smaller with increasing depletion intensity I_{max}.

a pinhole onto a detector exactly as in the confocal case, with the only difference, that the collected fluorescence stems from a smaller region in the sample, leading to an increased resolution for scanning imaging. Imaging this fluorescence onto a screen or a camera still results in a blurred spot which is due to the detection PSF $h(x)$. However, fluorescence emission is restricted to a sub-diffraction area, which for convenience is called the *effective PSF*.

The resolution of a RESOLFT-type microscope scales with the intensity of the depletion light I_{FD}. The higher the intensity, the smaller the region with molecules which are still in state S_F. The achievable resolution can as an extension to equation 2.1 be written as ([7], for the derivation see appendix A.2.3):

$$\Delta x \approx 0.61 \frac{\lambda}{n \cdot sin\alpha \cdot \sqrt{1 + I_{FD}/I_0}} \tag{2.4}$$

Δx is the FWHM of the effective PSF, n the index of refraction and α the half-aperture angle. In the case of RESOLFT, λ is the wavelength of the light driving the transition between the two states S_T and S_D. The newly added square root term stems from the saturation behaviour with the saturation intensity I_0 (see figure 2.3) and the applied maximum intensity I_{FD}.

The concept of RESOLFT was described for one dimension only, but it can be readily extended to two and three dimensions, using for example a doughnut shaped intensity distribution with a central zero ([20]).

The range of applicable optical transitions in RESOLFT is very broad and the actual implementations can be very different, altough they all are derived from the same concept. The first one implemented was **ST**imulated **E**mission **D**epletion ([11] and [12]). The fluorescent state S_F in this case is the first excited singlet state S_1 and the dark state S_D is the

ground state S_0, the depletion transition driving $S_1 \rightarrow S_0$ is stimulated emission. In the case of STED, the dye molecules in their ground state are excited into S_1 (e.g. by a confocal spot). Within a short timeframe after excitation the STED beam is applied with a doughnut intensity distribution, for example. The timeframe needs to be very short as STED has to compete against natural relaxation from $S_1 \rightarrow S_0$ (e.g. fluorescence).

Another mechanism for RESOLFT using switchable proteins is completely different. In the fluorescent protein asFP595, for example, the two states S_F and S_D are different conformations of the molecule, one of which is fluorescent. The transition $S_F \rightarrow S_D$ is achieved by light of one color, while the reverse transition is both spontaneous and driven by the excitation light itself ([21]). This complicates the saturation behaviour and the imaging process, but subdiffraction resolution was achieved with the use of asFP595 ([15], [16]).

It might also be possible, that the light-driven transition is from the dark state S_D to the fluorescent state S_F of the dye. This does not change the RESOLFT concept in principle, but leads to a reversed saturation curve (exchange S_F and S_D in figure 2.3) and a more complicated imaging and reconstruction process ([22]).[2]

Therefore the imaging protocol - the sequence of light pulses to prepare the sample, excite fluorescence and if necessary reset the dye molecules to their original state - can be very different depending on the dye molecules used as fluorescent markers and needs to be optimized before imaging.

Another possible mechanism for RESOLFT is **G**round **S**tate **D**epletion ([17], [23], [22], [24]), which is used in this project and will be discussed in the next section. The parameters and settings necessary to apply GSD within RESOLFT will be determined in chapter 3 and its application to enhance resolution will be shown in chapter 4.

2.2 Ground State Depletion

Ground **S**tate **D**epletion (GSD) is one of several RESOLFT mechanisms to achieve resolution enhancement. To understand the concept of GSD first the electronic energy levels and the transitions in a dye molecule have to be considered.

S_0 is the electronic singlet ground state of a molecule and, as it is – in most molecules – the energetically lowest state, an excited molecule relaxes into this state (see figure 2.5). Absorbtion of a photon excites a dye molecule from the ground state to a higher excited state S_n. In the case of fluorescence excitation the higher excited state is the first electronically excited state, S_1. The final state is not only electronically but vibrationally excited, too (S_1^{vib}), from which it relaxes very fast ($< \ ps$) to the lowest vibrationally excited state S_1. The transition from S_1 to S_0 can happen spontaneously either at the non-fluorescent rate $k_{nf} \approx 10^9 \frac{1}{s}$ (e.g. **i**nternal **c**onversion (IC) via vibration or other quenching mechanisms such as eletron transfer) or by emitting a photon of energy E_{em} at rate $k_{em} \approx 10^9 \frac{1}{s}$. k_{10} will be the combined deexcitation rate $k_{10} = k_{em} + k_{nf} \approx 10^9 \frac{1}{s}$. Fluorescence emission often

[2] This will not be discussed in detail, but partially adressed in chapter 3.1.1.

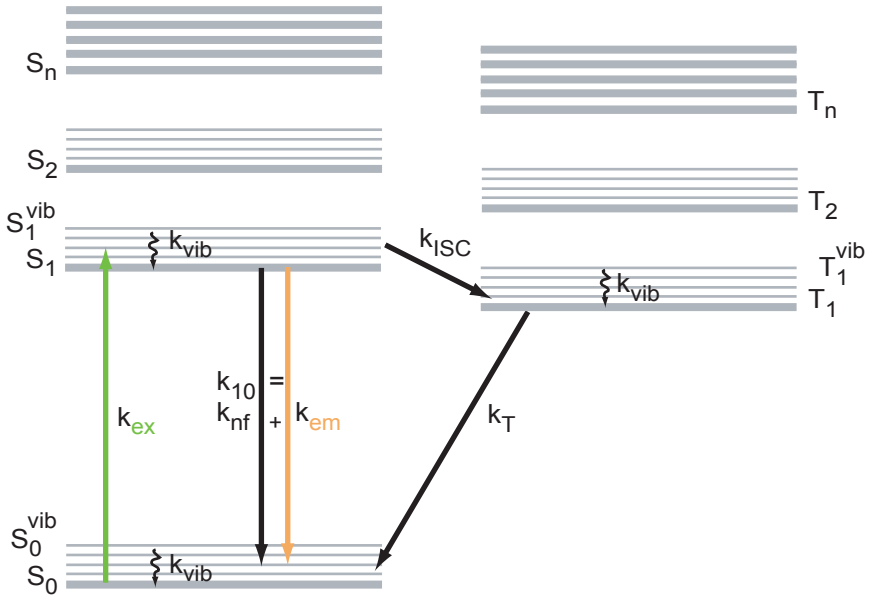

Figure 2.5: **Jablonski-diagram of a dye molecule** with S_0 the singlet ground state, S_1 the first eletronically excited singlet state, S_2 and S_n the higher excited singlet states, T_1 the lowest excited triplet state, T_2 and T_n the higher excited triplet states. S^{vib} and T^{vib} are the respective vibrationally excited states. The transition rates are: k_{ex} excitation rate, k_{em} fluorescence emission rate, k_{nf} nonfluorescent de-excitation rate, resulting in $k_{10} = k_{em} + k_{nf}$ the singlet de-excitation rate, k_{ISC} inter-system-crossing rate, k_T triplet relaxation rate and k_{vib} vibrational decay rate.

occurs most effectively into vibrationally higher excited states (S_0^{vib}) of S_0, from where fast relaxation to the lowest vibrational state of S_0 occurs.

The relaxation of the vibrationally excited states(S_0^{vib}, S_1^{vib}) is associated with a loss in energy so that:

$$E_{ex} = hc/\lambda_{ex} = E(S_1^{vib}) - E(S_0)$$
$$E_{em} = hc/\lambda_{em} = E(S_1) - E(S_0^{vib})$$

with E_{ex} the energy of the photon exciting the dye molecule from S_0 to S_1^{vib} with its wavelength being λ_{ex} and E_{em} and λ_{em} the energy and wavelength of the photon emitted during the tranistion from S_1 to S_0^{vib}. c is the velocity of light and h Planck´s constant. $E(S_0)$, $E(S_0^{vib})$, $E(S_1)$ and $E(S_1^{vib})$ are the energies of the respective states. Since $E(S_0^{vib}) > E(S_0)$ and $E(S_0^{vib}) > E(S_1)$ this results in

$$E_{ex} > E_{em} \quad \Leftrightarrow \quad \lambda_{ex} < \lambda_{em}$$

This difference in energy between the exciting and emitted photons is the so-called Stokes-Shift. The wavelength of the emitted light is red-shifted in comparison to the ex-

citation light [3]. The emitted fluorescence F is proportional to the population of the singlet state S_1. The excitation rate k_{ex} from S_0 to S_1 depends on the amount of illumination light I, the absorption cross section σ_{ex} and the inverse photon energy γ_{ex}:

$$k_{ex} = \sigma_{ex} \cdot \gamma_{ex} \cdot I$$

Apart from relaxing to the ground state about 1% of the excited molecules cross to the triplet state T_1 with a rate of $k_{ISC} \approx 10^6 \frac{1}{s}$ (**i**nter-**s**ystem-**c**rossing (ISC)[4]). In the singlet system all electrons in the dye molecule are spin-paired, which leads to a total spin angular momentum of zero. In the triplet system the spin of the excited eletron has flipped, resulting in two unpaired electron spins, giving a total spin angular momentum 1. Because of the quantum mechanical selecton rules the transition from T_1 to S_0 is electric-dipole forbidden and it occurs at a much lower rate than $S_1 \rightarrow S_0$ ($k_{10} \approx 10^9 \frac{1}{s} > k_T \approx 10^3 - 10^6 \frac{1}{s}$).

For GSD, the illumination light forces molecules from the ground state S_0 to another state, e.g. higher excited singlet states S_n or higher excited triplet states T_n, i.e. effectively depleting the ground state and therefore fluroescence. The two most probable states for that are the first excited singlet state S_1 and the first excited triplet state T_1 (see figure 2.5). How effectively this can be done depends on the dynamic properties of the dye molecule, that is the deexcitation rate k_{10}, the rate for inter-system-crossing k_{ISC} or the triplet relaxation rate k_T etc. The efficiency of ground state depletion can be derived by the rate equation system. The following equations (2.5) describe a three level system consisting of the singlet ground state S_0, the first excited singlet state S_1 and the lowest excited triplet state T_1 (ignoring higher excited triplet and singlet states).

$$\begin{aligned} \dot{S}_0 &= -k_{ex} \cdot S_0 + (k_{10}) \cdot S_1 + k_T \cdot T_1, \\ \dot{S}_1 &= k_{ex} \cdot S_0 - (k_{10}) \cdot S_1 - k_{ISC} \cdot S_1, \\ \dot{T}_1 &= k_{ISC} \cdot S_1 - k_T \cdot T_1, \\ S_0 + S_1 + T_1 &= 1 \end{aligned} \tag{2.5}$$

The vibrational levels of S_0, S_1 and T_1 are ignored because the relaxation to the lowest vibrationally excited level is so fast ($k_{vib} > 10^{12} \frac{1}{s}$) in comparison to other processes ($k_{10} \approx 10^9 \frac{1}{s}, k_{ISC} \approx 10^6 \frac{1}{s}, k_T \approx 10^3 - 10^6 \frac{1}{s}$) that it can be considered instantaneous. In the Appendix A.2.4 the complete equations and the derivation of the steady state levels are shown.

In the case of a dye with negligible inter-system-crossing ($k_{ISC} = 0$), the steady state leads to the following relationship between the emitted fluorescence F, which is porportional to the steady-state population S_1^{SS} of state S_1, and illumination intensity I:

[3] This is only the case in one-photon processes. In case of two-photon absorption or CARS (coherent anti-Stokes Raman scattering) the relationship for absorbed and emitted photons are different.

[4] The Rate for ISC varies strongly for different dyes and different ambient conditions.

$$F(I) \propto S_1^{SS}(I) = \frac{1}{1 + \frac{k_{10}}{\sigma_{ex} \cdot \gamma_{ph} \cdot I}} \overset{I \to \infty}{\to} 1 \tag{2.6}$$

In the case of dyes that show ISC $k_{ISC} \neq 0$, the steady state fluorescence is:

$$F(I) \propto S_1^{SS}(I) = \frac{1}{1 + \frac{k_{ISC}}{k_T} + \frac{k_{10} + k_{ISC}}{\sigma_{ex} \cdot \gamma_{ph} \cdot I}} \overset{I \to \infty}{\to} \frac{k_T}{k_T + k_{ISC}} < 1 \tag{2.7}$$

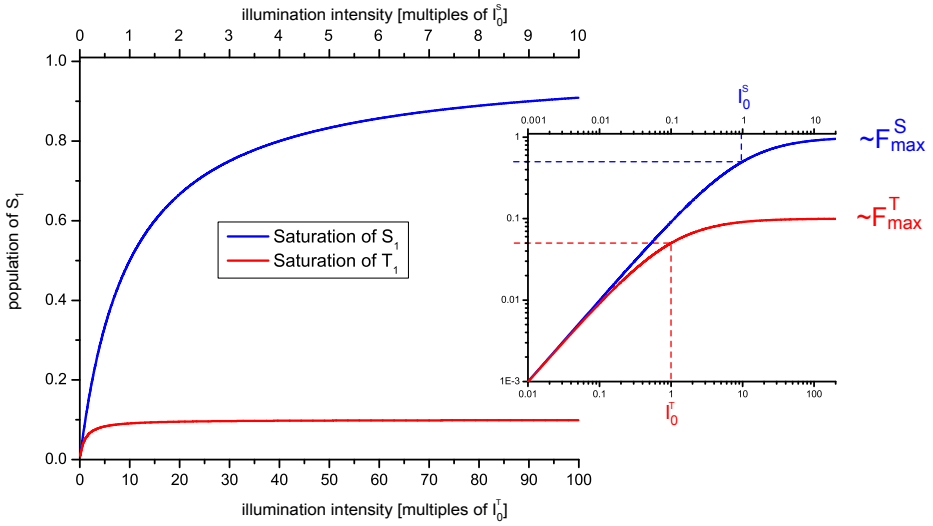

Figure 2.6: **Schematic population curves for GSD** without (blue) and with (red) triplet population with increasing illumination intensity, with linear and logarithmic illumination intensity scale (inlay). The saturation intensity I_0 is defined as the intensity at which half of the maximal possible population is reached: $I_0^T = \frac{k_T}{k_T + k_{ISC}} \cdot I_0^S$, with $\frac{k_T}{k_T + k_{ISC}} = 0.1$ for this simulation. The maximum fluoerscence level scales with the same quotient: $F_{max}^T = 0.1 \cdot F_{max}^S$. The fluorescence is proportional to the population of S_1.

In figure 2.6 the steady-state population S_1^{SS} is depicted over the illumination intensity I. After an initial linear rise, the fluorescence saturates at F_{max}. This fluorescence saturation level is reached when the same amount of molecules enters and leaves the saturated state (e.g. S_1 in the case of no triplet build or T_1 in the case with consideratable triplet build). Once saturation is achieved, increasing the illumination intensity further does not result in larger fluorescence emission. The value of F_{max} is lower in the case of triplet saturation $F_{max}^T \propto \frac{k_T}{k_T + k_{ISC}}$ than for singlet saturation $F_{max}^S \propto 1$, because the molecules trapped in T_1 do not contribute to the fluorescing cycle. The saturation intensity I_0 is defined as the intensity at which half of the saturation level F_{max} is achieved. It is used as a measure to compare the saturation properties of different dyes. I_0^S and I_0^T can be calculated from equations 2.6 and 2.7, respectively, as:

$$
\begin{aligned}
I_0^S &= \frac{k_{em} + k_{nf}}{\sigma_{ex} \cdot \gamma_{ph}} \\
I_0^T &= \frac{k_T}{k_T + k_{ISC}} \cdot \frac{k_{em} + k_{nf}}{\sigma_{ex} \cdot \gamma_{ph}}
\end{aligned} \tag{2.8}
$$

simplifying the equations for fluorescence to:

$$
\begin{aligned}
F^S(I) &\propto \frac{1}{1 + \frac{I_0^S}{I}} \\
F^T(I) &\propto \frac{k_T}{k_T + k_{ISC}} \cdot \frac{1}{1 + \frac{I_0^T}{I}}
\end{aligned} \tag{2.9}
$$

For ground state depletion it does not matter if the single state S_1 or the triplet state T_1 is populated. The principle of GSD, with or without triplet build-up can be applied to any dye, but both saturation mechanisms have their limitations. Saturation intensity I_0^S for the singlet state S_1 is higher than I_0^T for the triplet state T_1 (see equation 2.8): for example with the rate constants $k_{ISC} \approx 10^6 \frac{1}{s}$ and $k_T \approx 10^3 \frac{1}{s}$, $I_0^T \approx \frac{1}{10^3} \cdot I_0^S$ and $F_{max}^T \approx F_{max}^S \frac{1}{10^3}\cdot$. Higher illumination intensities I_{max} are necessary to achieve the same degree of saturation ($\xi_0 = I_{max}/I_0$) comparing the saturation with or withour population of the triplet state. On the other hand, the fluorescence saturation level is lower with triplet population, leading to longer exposure times for the same signal-to-noise ratio. Apart from that, the triplet lifetime $\tau_T = 1/k_T$ plays an important role in the saturation of the triplet. The larger τ_T the earlier the triplet will saturate leading to a lower I_0 and a better saturation factor. But on the other hand this leads to longer delay times until the triplet state has relaxed completely and sample-scanning can proceed.

As described above, the RESOLFT concept necessitates a fluorescent state S_F and a nonfluorescent dark state S_D. In case of GSD without triplet population the states are:

$$S_F = S_1 \qquad \text{and} \qquad S_D = S_0$$

The transition from S_0 to S_1 is driven by the excitation light, the reverse transition is spontaneous with the rate $k_{10} = k_{em} + k_{nf}$.

In the case of GSD with triplet build the states are:

$$S_F = S_1 \qquad \text{and} \qquad S_D = T_1$$

The dye molecules are driven from the singlet system to T_1 by the excitation light via ISC from the first excited triplet state S_1. The reverse transition is spontaneous with the triplet relaxation rate k_T.

Both saturation mechanisms lead to an increase and saturation of fluorescence with larger illumination intensities (see figure 2.6). This must be taken into account when designing the spatial distribution during the actual imaging. Before GSD can be put into practice for RESOLFT resolution enhancement, though, there are some problems that have will be adressed in the following section and possible solutions will be presented in chapter 3.

2.3 Problems inherent to RESOLFT microscopy

Time

A general problem of single point scanning RESOLFT microscopy is the long image acquisition time. As for confocal microscopy, the sample has to be scanned by a specially designed intensity distribution featuring a local zero. An increase in resolution by a factor of two in one dimension requires twice as many scannings steps, leading to a factor of four in two dimensions, which increases the time for a whole image by a factor of four. Additionally, the region from where fluorescence is sampled during one scanning step is smaller. Thus the sampling time for one scanning step should be elongated to achieve the same signal-to-noise ratio. These two effects, scanning step size and signal-to-noise ratio, lead to longer acquistion times for single images as the resolution increases.

To counteract the increase in image acquistion time due to high-resolution imaging, it is a possibility to parallelize image acquisition. Therefore the illumination has to be structured with not only one point of zero-intensity but several, while fluorescence has to be detected from several areas simultaneously but , preferably by widefield detection. A structured illumination pattern and the possible resolution enhancement achievable will be discussed in section 3.1.

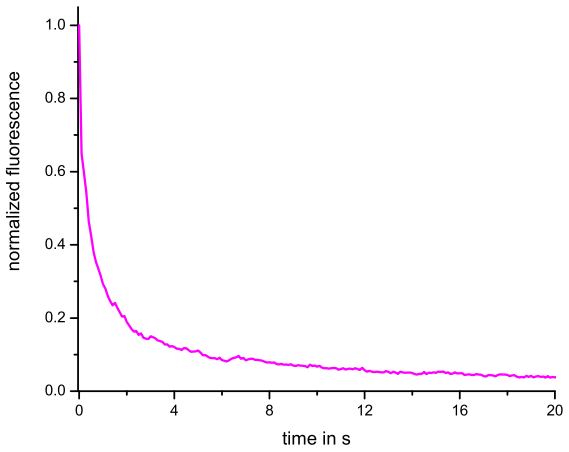

Figure 2.7: **Irreversible bleaching** of fluorescence emitted by beads labeled with Atto-532 excited by green laser light ($532\ nm$) for $\approx 20s$, illumination intensity $I = 750W/cm^2$

Bleaching

Due to the high intensitites required for large saturation factors and thus improved resolution there is a considerable amount of photobleaching. Photobleaching leads to an irreversible loss of fluorescence, caused by enhanced reactivity from higher excited states and increases with illumination intensity. Thus, following illumination of an ensemble of dye molecules the fluorescence signal decays exponentially (or multi-exponentially) over time (see figure 2.7).

In RESOLFT-microscopy the illuminated area, for example the area that is illuminated by the depletion light which drives S_F to S_D, is larger than the region from where the fluorescence signal is probed. Thus bleaching does not only affect the region of fluorescence probing, but the whole illuminated area, which may cause unpredictable artifacts.

For high resolution RESOLFT imaging high intensities have to be used (see equation 2.4). To avoid photobleaching low intensities would have to be applied, leading to less resolution enhancement. Another possibility to decrease photobleaching without decreasing the illumination intensity and thus impair resolution is by evacuating and cooling the sample to 80 , which will de addressed in detail in section 3.2.

Photophysics

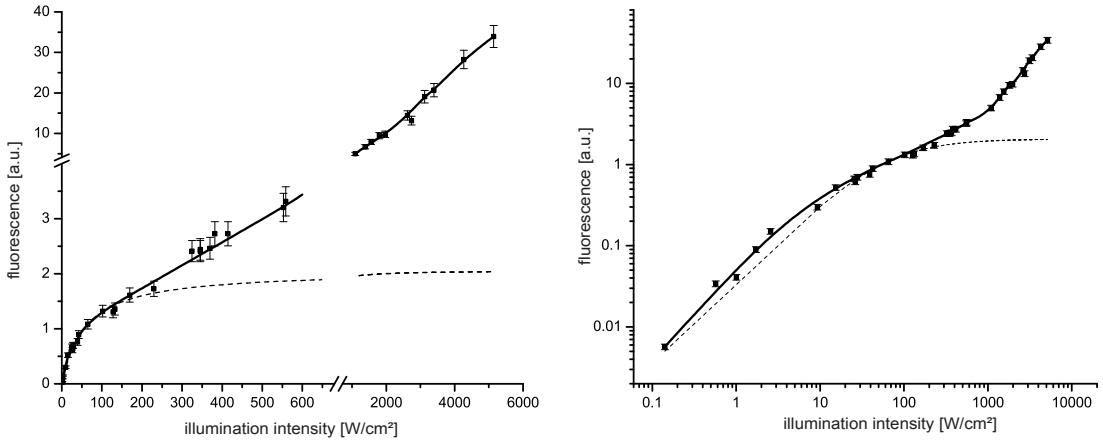

Figure 2.8: **Fluorescence signal due to excitation with different intensities** of propidium iodide with green light ($532\ nm$ CW), left linear, right logarithmical scale; dots: measured values, straight line: eyeguide only, dashed line: fluorescence saturation behaviour as expected from equation 2.9 fit to overlay in the low intensity region

As described in chapter 2.2 the saturation depends on the photophysical properties of the applied dye. For all dyes tested the fluorescence signal was recorded for increasing intensities. From equation 2.9 a fluorescence saturation curve as in figure 2.6 is expected, but none of the tested dyes showed a satisfactory saturation behaviour. Figure 2.8 depicts the saturation curve of propidium iodide.

Propidium iodide is heavy-atom doted and known to have large ISC and thus a large triplet yield ([25]). The saturation intensity I_0 is expected to be moderate. As can be seen in figure 2.8 fluorescence rises linearly up to an illumination intensity of $\approx 50W/cm^2$, where fluorescence seems to level to a saturation value due to enhanced triplet population. But instead of approximating an expected saturation value such as the dashed lines in figure 2.8, fluorescence increases further with increasing illumination intensity, yet this unexpected increase is less than in the linear increase for low intensities.

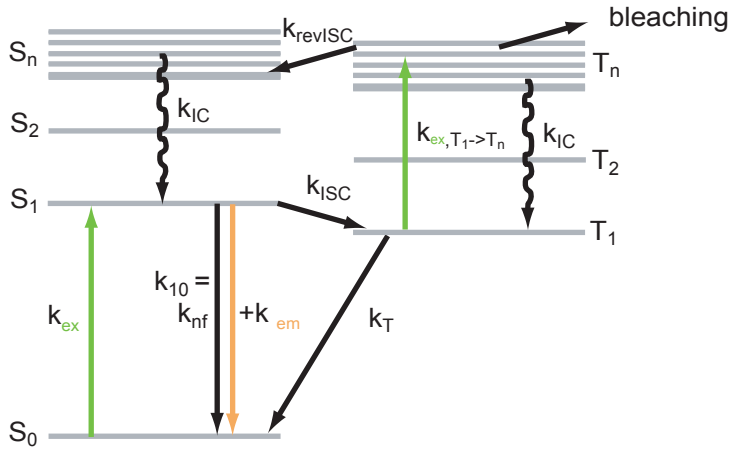

Figure 2.9: **Jablonski diagram including bleaching and reverse ISC**, additional excitation from T_1 to T_n by the green excitation light with an excitation rate $K_{ex,T1->Tn}$ and bleaching from T_n.

The unexpected increase in signal at intensities $> 100\ W/cm^2$ can be explained by the excitation of molecules in the triple state T_1 to higher excited triplet states T_n by the same illumination light. From T_n they can either decay back to T_1, bleach or return to the singlet system (**rev**erse **i**nter-**s**ystem-**c**rossing, k_{revISC})(see the Jablonski diagram in figure 2.9). From higher exited singlet states S_n they decay nonradiatively to S_1 via internal conversion (k_{IC}) and are again available for the fluorescent cycle between S_0 and S_1. Reverse ISC depletes the triplet population and increases fluorescence with higher illumination intensities. Simulation of this behaviour using an extended rate equation system similar to equations 2.5 is given in the appendix A.2.7.

Same or similar results were found for Rhodamin 6G and Atto532 in PVA or Glycerol and for Quantum Dots (CdSe/ZnSe Evidots) in air. All tested dyes did show a nonlinear relationship between applied intensity and measured fluorescence but no real saturation level. At even higher intensities I the transition from $T_1 \rightarrow T_n$ ($k_{ex,T1->Tn} \propto I$) can compete against internal conversion from $T_n \rightarrow T_1$, so that $k_{ex,T1->Tn} \geq k_{IC} \approx 10^{15}\frac{1}{s}$. The saturation of

the transition $T_1 \rightarrow T_n$ results in a saturation behaviour of fluorescence emission as theoretically depicted in figure 2.8 but at much higher intensities. Such intensities, especially when the triplet system is involved, lead to very strong bleaching, proving that the saturation of $T_1 \rightarrow T_n$ is not useful for high-resolution microscopy.

Another possible mechanism is the saturation of the transition from $S_0 \rightarrow S_1$, but for this the population of the triplet state has to be avoided. By the use of a pulsed laser of a repetition frequency in the range of kHz instead of a cw laser to illuminate the sample, the dye molecules which have crossed to the triplet state are given time to relax to the singlet state (in dyes with triplet lifetime of $\approx ms$, [22]) before being illuminated by the next pulse. Saturation of the transition from $S_0 \rightarrow S_1$ needs much higher illumination intensities I for high saturation factors $\xi_{sat} = I/I_0$, as the saturation intensity I_0^S for $S_0 \rightarrow S_1$ is higher by a factor of $\frac{k_T + k_{ISC}}{k_T}$ than the saturation intensity, when the triplet is involed (see equation 2.8).

The approach taken in the current work is preparing the steady-state populations (inculding the triplet state) and probing the residual population of the singlet. This will be discribed in more detail in section 3.3.

3 Experimental Realisation

In the previous chapter the use of ground state depletion for RESOLFT-microscopy and the inherent problems have been adressed. In order to accelerate the image acquisition parallelization with structured illumination and widefield detection will be discussed in the first section. Bleaching can be reduced by evacuating and cooling the sample which will be addressed in the second section. In the third section the effects of the absence of oxygen and low temperature on the photokinetic parameters of the dyes in use and the saturation of depletion will be presented.

3.1 Time: Parallelisation

As described in chapter 2.3, one major problem of image formation using single-spot scanning is the long acquisition time. It takes between five and 30 minutes for one high-resolution STED image, depending on image acquisition area, pixel spacing and desired signal-to-noise ratio. In order to make the imaging process faster, it is possibile to use widefield illumination, i.e. illumination of a larger area with a diameter in the range of several μm in comparison to $300\ nm$ in confocal microsopy, and camera-based widefield-detection. To still reach subdiffraction resolution, the illumination has to be structured with several zero intensity regions to exploit the advantages of the RESOLFT concept. The easiest way to achieve such a pattern is to let two beams interfere in the focal plane under an angle α, as will be described in chapter 4.1. The interference results in a sine squared illumination pattern along one lateral direction, leading to a resolution enhancement along that direction, as described below. The distance D between two neighbouring interference stripes is $D = \lambda/(2n\ sin(\alpha/2))$ with λ denoting the wavelength of the illumination light and n the index of refraction at the sample, which for the moment will be set $n = 1$ for air.

3.1.1 Theoretical explanation

The increase in resolution resulting from such a sinesquare illumination pattern is based on the saturation of fluorescence excitation or fluorescence depletion. An explanation of the resolution enhancement in real space and in the frequency domain will be given in the following sections.

Real space

Figures 3.1 and 3.2 depict a sinequare illumination pattern along the lateral x-direction (green) and the fluorescence signal that would be emitted from a single dye molecule at a certain position x (yellow, red, pink and purple). Figure 3.1 exemplifies the case of saturating fluorescence depletion, with a patterned intensity distribution (green) and a homogeneously distributed intensity of fluorescence excitation or probing (blue). There is a simultaneous exposure to homogeneous light, which is exciting fluoresence and depicted in blue, and patterened depletion light in green. Figure 3.2 describes the case of patterned fluorescence excitation, like ground state depletion (as described in chapter 2.2).

First, the case of fluorescence depletion is discussed, which will be called *positive stripes*. In the top part of figure 3.1 (A) the homogeneous light exciting or probing fluorescence is shown in light blue and the sine squared pattern of the depletion light is shown in green. The points with the largest depletion intensity I_{max} are at the maxima of the sine squared pattern. The distance between the maxima is $D = \lambda/(2sin(\alpha/2))$, with α the angle between the incident beams and λ the wavelength of the depletion light. Part (B) of this figure shows a typical depletion curve, for example a STED saturation curve. The curve is normalized to the fluorescence signal without any depletion. As before, the saturation intensity I_0 is defined as the intensity at which half of the fluoresence is depleted. For simplification the depletion intensity is given in multiples of the saturation intensity I_0. This saturation behaviour is applied to the sine squared illumination pattern for the depletion light.

At a low depletion intensity $I_{max} = 0.1 \cdot I_0$ the relationship between depletion intensity $I(\mathbf{x}) \propto sin^2(\pi\ \mathbf{x}/D)$ and fluorescence resulting from homogeneous excitation light can be considered linear. The resulting fluorescence $F_{prob}(I_{max}, \mathbf{x})$ can be understood as the fluorescence emission probability of a single dye molecule at a position **x** following depletion with the interference pattern $I(\mathbf{x})$ and the maximal intensity I_{max}. For low $I_{max} = 0.1 \cdot I_0$ the fluorescence emission probability can be described as $F_{prob}(I_{max}, \mathbf{x}) \propto 1 - I(\mathbf{x}) \propto 1 - sin^2(pi\ \mathbf{x}/D)$. For the applied intensity it is a reversed sine squared pattern (see yellow trace in (A)), with the lowest fluorescence emission probability at the maxima of the depletion light.

When the depletion intensity is increased to $I_{max} = 1 \cdot I_0$ (red trace) the maximal depletion is 50%. The valleys of the sine squared fluorescence probability pattern get deeper. Further increase of the maximal depletion intensity (pink and purple trace) enhances this effect, leading to minima of approximately 90% and 98%. Apart from lowering the minima, the minima are broadened in comparison to the maxima. In part (C) of 3.1 all fluorescence emission probabilities with different I_{max} have been normalized for better comparison. The FWHM decreases with increasing depletion intensity. The fluorescence emission is confined to smaller and smaller regions. By saturation of fluorescence depletion the FWHM of these regions can be driven beyond the diffraction limit. The high resolution information of the resulting image lies within the small maxima and the steep slopes of these maxima, which will be addressed later.

The second approach is based on saturation of fluorescence excitation (**negative stripes**). Figure 3.2 (B) shows a saturated excitation curve as in figure 2.6, which was derived in

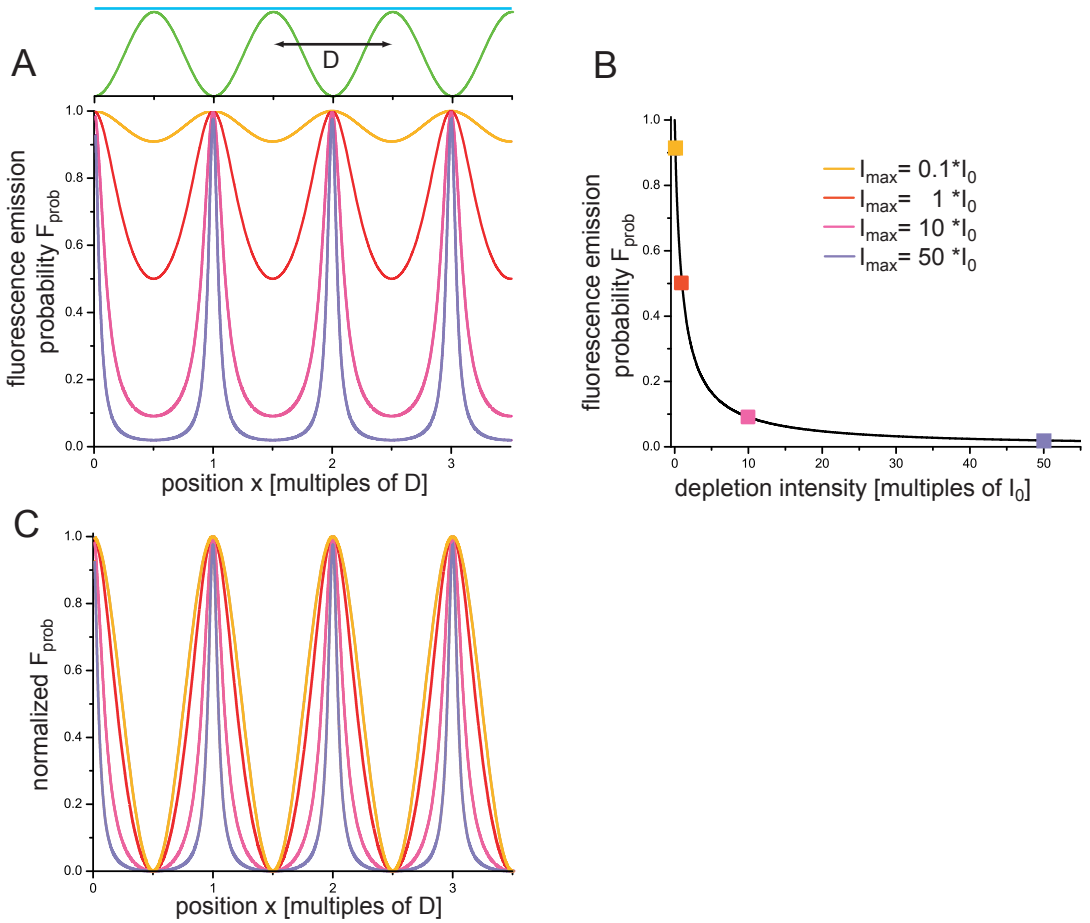

Figure 3.1: **Structured illumination with *positive stripes* (fluorescence depletion)**
A: The upper part shows the sine squared illumination pattern of the depletion light in green and the homogeneous illumination with excitation or probing light in blue. The lower part shows the effect of increased depletion light on the fluorescence emission probability. The minima of the fluorescence - at the maxima of the depletion light - get lower and broader with increasing depletion intensity and the remaining fluorescence regions get sharper and smaller. **B:** Schematic depletion curve which was used to determine the fluorescence pattern of part (A). The saturation intensity I_0 is defined as the intensity at which half of the fluorescence is depleted. **C:** The fluorescence emission probability curves from part (A) are normalized to show the decrease in FWHM of the remaining area of fluorescence emission with increasing depletion intensity.

the previous chapter for ground state depletion with and without the triplet state. The curve is normalized to the maximal possible fluorescence, which is reached asymptotically with increasing intensity. The saturation intensity I_0 is defined accordingly as the excitation intensity at which half of the maximal fluorescence is emitted. Once again at a low excitation intensity, i.e. $I_{max} = 0.1 \cdot I_0$, the relationship between illumination intensity $I(\mathbf{x})$ and resulting fluorescence probability $F_{prob}(I_{max}, \mathbf{x})$ can be considered linear $F_{prob}(I_{max}, \mathbf{x}) \propto I(\mathbf{x}) \propto sin^2(\pi\, \mathbf{x}/D)$. This leads to a sine squared pattern (yellow trace) for $F_{prob}(I_{max}, \mathbf{x})$ with the minima at the position of the minima of $I(\mathbf{x})$. The fluorescence

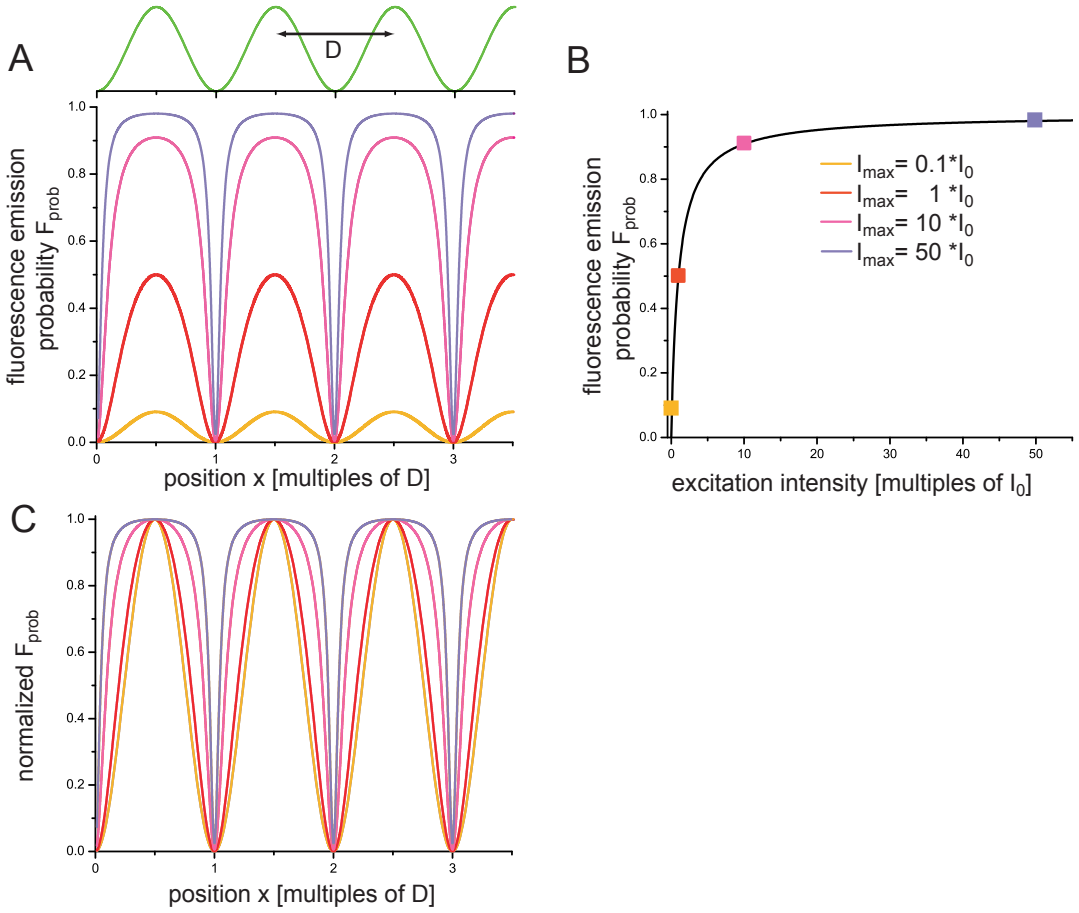

Figure 3.2: **Structured illumination with *negative stripes* (fluorescence saturation)**
A: The upper part shows the sine squared illumination pattern of the excitation light in green. The lower part shows the effect of increased excitation light on the fluorescence emission probability. The maxima of the fluorescence - at the maxima of the excitation pattern - increase and broaden with increasing excitation intensity. **B:** Schematic excitation curve (i.e. saturation of S_1) which was used to determine the fluorescence pattern of part (A) . The saturation intensity I_0 is defined as the intensity at which half of the maximal possible fluorescence is emitted. **C:** The fluorescence emission probability curves from part (A) are normalized to show the decrease in FWHM of the minima with increasing excitation intensity.

probability does not exceed 10% all over the sample and the resulting signal would be very low.

An increase in excitation intensity to $I_{max} = 1 \cdot I_0$ results in a higher maximum fluorescence probability of 50% and a slight deviation from the sine squared fluorescence profil. Further increasing the excitation intensity leads to a broadening of the maxima contrary to the case of fluorescence depletion, where the minima were broadened. At large excitation intensities the probability for fluorescence emission is almost uniformly 1, apart from dips to zero at the minima of the illuminating sine squared pattern. As can be seen in part (C) of 3.2, where normalized emission probabilities are shown, the FWHM of these dips in fluorescence

decrease with increasing illumination intensity.

Saturation of fluorescence excitation such as GSD turns the sine squared illumination pattern into an altered fluorescence emission probability pattern, with broadened maxima, constricted minima (see 3.2 (C)) and steepened slopes. This will transport the high resolution information to the final image.

To summarize, a sine squared illumination pattern in combination with fluorescence depletion leads to high probability peaks for fluorescence emission in the position of the illumination minima. In contrast, the sine squared pattern with fluorescence saturation results in a uniformly high fluorescence emission probability with spatially constricted and steep dips to zero at the illumination minima. The following section will explain such spatially structured fluorescence emission probability results in an actual resolution enhancement.

The object that is imaged consists of a distribution of dye molecules $\rho_{dye}(\mathbf{x})$, which leads to the following fluorescence signal $S(\mathbf{x})$ from the sample after illumination with excitation and depletion light

$$S(\mathbf{x}) = F_{prob}(I_{max}, \mathbf{x}) \cdot \rho_{dye}(\mathbf{x}). \tag{3.1}$$

with $F_{prob}(I_{max}, \mathbf{x})$ the fluorescence emission probability, depicted in figures 3.1 and 3.2.

In the case of fluorescence depletion at high illumination intensities (and therefore high saturation factors $\xi_{Sat} = I_{max}/I_0$), fluorescence emission is confined to the zero-intensity regions, that is, the maxima of the sine squared depletion pattern as outlined in figure 3.1.

During the imaging process the signal $S(\mathbf{x})$ is blurred (see figure 3.3) due to the diffraction limit of the detection optics (with a certain numerical aperture NA), i.e. the detection process cannot discriminate objects closer than $\Delta x = 0.61\ \lambda/NA \approx \lambda/2$ (see chapter 2.1). This blurring can mathmatically be described by the convolution of the signal $S(\mathbf{x})$ with the point spread function (PSF) $h(\mathbf{x})$ of the detection optics:

$$B(\mathbf{x}) = S(\mathbf{x}) \otimes h(\mathbf{x}) = [F_{prob}(I_{max}, \mathbf{x}) \cdot \rho(\mathbf{x})] \otimes h(\mathbf{x}) \tag{3.2}$$

As long as the distance D of the pattern is at least two times the width Δx of the point spread function $h(\mathbf{x})$ even after the blurring the fluorescence can easily be associated with the confined fluorescence regions of the zero depletion intensity. Using this a priori knowledge the emitted fluorescence from the sample can be re-associated to its region of origin. This is the same principle as in RESOLFT-confocal microscopy, with the only difference being a spatial detector such as a camera instead of a point detector. In comparison to single-point scanning the structured illumination in combination with camera-based detection allows much faster image acquisition, since fluorescence signals from every pattern maximum can be detected simultaneouslyand in parallel. Scanning of the pattern is necessary though, but only in one direction (the direction of the modulation x) and only the distance between two maxima (D), which leads to a considerable reduction in acquistition time in comparison to confocal microscopy.

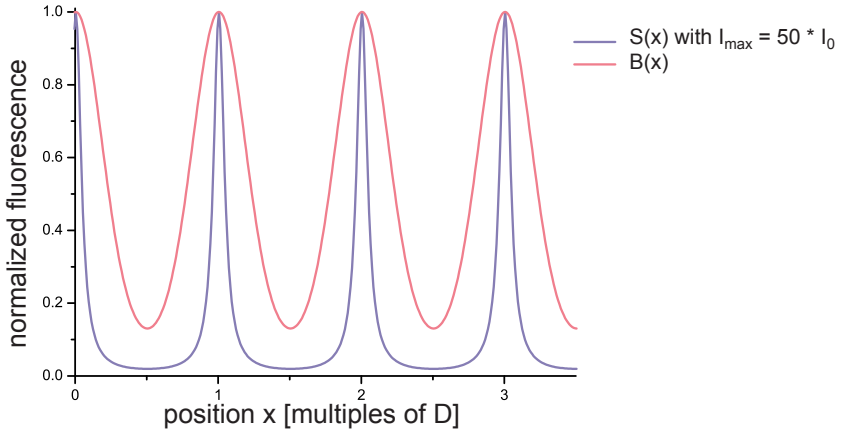

Figure 3.3: **Blurring of constricted stripes due to diffraction limit of detection optics**, the emission probability pattern F_{max} for fluorescence depletion with $I_{max} = 50 \cdot I_0$ is depicted in blue, the blurring by the detection optics shown in red. The distance of the maxima was chosen $D = 2.5\,\Delta x$, with Δx the FWHM of the detection PSF $h(\mathbf{x})$.

In the case of fluorescence saturation, equation 3.1 leads to a sample fluorescence that is opposite to the first case. Fluorescence is emitted from all dye molecules of the sample but the ones in the minima of the illuminating interference pattern. These dips in fluorescence will be disguised by the imaging process (see equation 3.2) but are nonetheless there. Taking a structured illumination image and substract if from a nonstructured widefield image will for example lead to images as described above.

The only difference between the two imaging methods is the amount of photon noise. Photon noise is proportional to the square root of the number of photons $\propto \sqrt{N_{Ph}}$. In the case of fluorescence depletion the signal consists of fluorescence from spatially confined regions, leading to a certain signal to noise ratio. In the case of fluorescence saturation, the signal is composed of the fluorescence photons missing in comparison to uniform illumination. Thus it is determined as the difference of two high-fluorescence images, one with homogeneous widefield illumination and one with patterned illumination. The signal due to *negative stripes* consists of a similar amount of photons as that from *positive stripes*, but carries the noise of the high-fluorescence images from which it was derived. Thus the signal-to-noise ration is worse in the case of fluorescence saturation. In conclusion, it is preferable to use fluorescence depletion (*positive stripes*) instead of fluorescence saturation (*negative stripes*), but this decision depends on the properties of the dye in question.

Fourier space

To be able to determine the factor of resolution enhancement due to saturated structured illumination the imaging process has to be considered in Fourier space. Every image can be transformed from the space domain, in which we see images, into the frequency domain, the so-called Fourier space. In real space, images are represented as intensities at a specific

point in space. In Fourier space, the basis (mathmatically speaking) are frequencies and their associated phases. It is hard for us, who are very used to the concept of space and space coordinates, to understand images represented in Fourier space, but for imaging it proves useful to change the coordinate system.

The Fourier transform[1] of a function $f(\mathbf{x})$

$$\hat{f}(\mathbf{k}) = \frac{1}{\sqrt{2\pi}} \int_{-\infty}^{\infty} f(\mathbf{x}) \cdot e^{-\mathrm{i}\,\mathbf{k}\cdot\mathbf{x}} d\mathbf{x} \tag{3.3}$$

and the reverse Fourier transform

$$f(\mathbf{x}) = \frac{1}{\sqrt{2\pi}} \int_{-\infty}^{\infty} \hat{f}(\mathbf{k}) \cdot e^{+\mathrm{i}\,\mathbf{x}\cdot\mathbf{k}} d\mathbf{k} \tag{3.4}$$

allow the transformation from one domain into the other. $\mathbf{x}$ is the variable in space and $\mathbf{k}$ the variable in frequency domain. A certain distance X corresponds to the frequency $K = 2\pi/X$, thus small details in the image in real space result in high frequencies in Fourier space. Convolution $f(\mathbf{x}) \otimes g(\mathbf{x})$ in real space turns into a simple multiplication $\hat{f}(\mathbf{x}) \cdot \hat{g}(\mathbf{k})$ in Fourier space and vice versa. Although an image in real space is real, its Fourier transform is a complex function. The chosen basis functions of the Fourier transform are the frequency amplitude $abs(\hat{f}(\mathbf{k})) = \sqrt{Re^2(\hat{f}(\mathbf{k})) + Im^2(\hat{f}(\mathbf{k}))}$ and the associated phase component $\varphi(\hat{f}(\mathbf{k})) = atan(Im(\hat{f}(\mathbf{k}))/Re(\hat{f}(\mathbf{k})))$. The Fourier transform can be expressed in its polar form:

$$\hat{f}(\mathbf{k}) = abs(\hat{f}(\mathbf{k})) \cdot e^{\mathrm{i}\varphi(\mathbf{k})} \tag{3.5}$$

For simplicity, only the frequency component $abs(\hat{f}(\mathbf{k}))$ will be shown in the figures.

As described in the previous chapter, during the imaging process the fluorescence signal from the sample is blurred, which can be describend by a convolution of the signal $S(\mathbf{x})$ with the PSF of the detection optics $h(\mathbf{x})$ (see equation 3.2). The Fourier transformation to

$$\begin{aligned} \text{real space} : B(\mathbf{x}) &= S(\mathbf{x}) \otimes h(\mathbf{x}) \\ &\Downarrow FT \\ \text{Fourier space} : \hat{B}(\mathbf{k}) &= \hat{S}(\mathbf{k}) \cdot \hat{h}(\mathbf{k}) \end{aligned} \tag{3.6}$$

with $B(\mathbf{x})$ the final image, and the respective Fourier transforms $\hat{B}(\mathbf{k})$, $\hat{S}(\mathbf{k})$ and $\hat{h}(\mathbf{k})$. $S(\mathbf{x})$ is the signal from the illuminated sample and defined as the product of the fluorescence emission probabilty $F_{prob}(I_{max}, \mathbf{x})$ and the dye distribution $\rho_{dye}(\mathbf{x})$ (see 3.1). It transforms to :

[1] The convention is that functions and their Fourier transform have the same letter as a name, but are discriminated by the hat and the following function parameter $\mathbf{x}$ in real space and $\mathbf{k}$ in Fourier space.

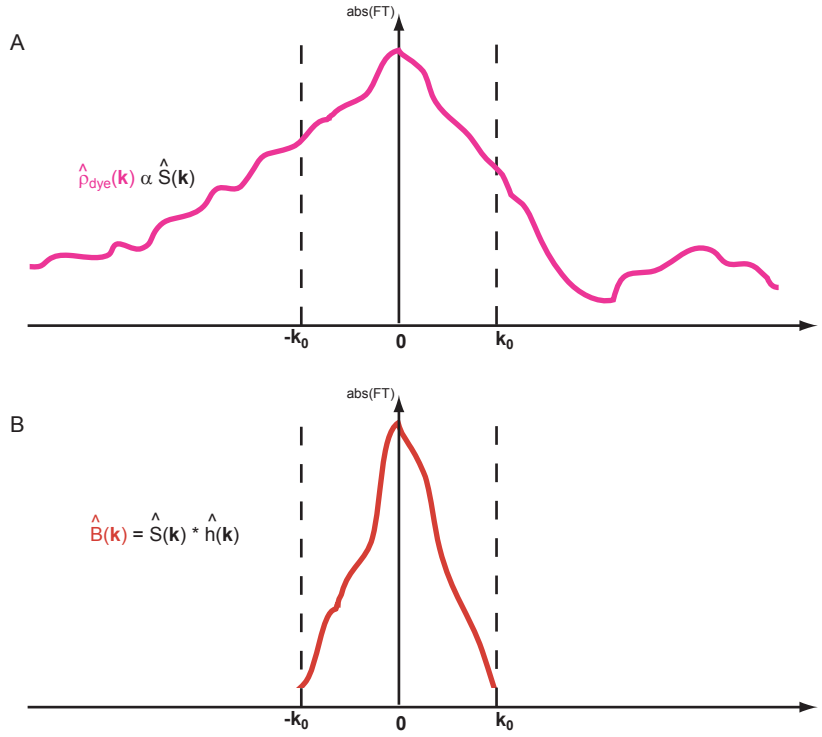

Figure 3.4: **Imaging process in Fourier Space**; (A): Fourier transfrom of a possible dye distribution ρ_{dye}, (B) : Result of the mulitplication of the dye distribution $\hat{\rho}_{dye}$ with the OTF $\hat{h}(\mathbf{k})$, image frequencies that are higher than $\mathbf{k}_0$ are cut off, because $\hat{h}(\mathbf{k})$ is nonzero only within the dashed lines (region of support)

$$\begin{aligned} \text{real space} : S(\mathbf{x}) &= F_{prob}(I_{max}, \mathbf{x}) \cdot \rho_{dye}(\mathbf{x}) \\ &\Downarrow FT \\ \text{Fourier space} : \hat{S}(\mathbf{k}) &= \hat{F}_{prob}(I_{max}, \mathbf{k}) \otimes \hat{\rho}_{dye}(\mathbf{k}) \end{aligned} \tag{3.7}$$

In figure 3.4 (A) the absolute value of a schematic Fourier transform of an arbitrary dye distribution $\hat{\rho}_{dye}(\mathbf{k})$ is shown. In case of uniform illumination, like in widefield microscopy, the signal from the sample is proportional to the dye distribution $S(\mathbf{x}) \propto \rho_{dye}(\mathbf{x})$, as are their Fourier transforms, $\hat{S}(\mathbf{k}) \propto \hat{\rho}_{dye}(\mathbf{k})$.

The **O**ptical **T**ransfer **F**unction $\hat{h}(\mathbf{k})$ (the Fourier transform of the PSF $h(\mathbf{x})$) of the optical system is nonzero only within $|\mathbf{k}| \leq |\mathbf{k}_0|$ which is the so-called region of support. $\mathbf{k}_0$ is the highest transmittable frequency and can be determined with the fluorescence wavelength $|\mathbf{k}_0| = 2\pi \cdot \mathrm{NA}/(0.5 \cdot \lambda) \approx 2\pi/\Delta x$. Frequencies higher than $\mathbf{k}_0$ correspond to image details smaller than the diffraction limit.

For the final image, $\hat{B}(\mathbf{k})$, the signal from the sample has to mulitplied with the OTF. As the OTF is zero for frequencies larger than $\mathbf{k}_0$, only the part of the dye distribution $\hat{\rho}_{dye}(\mathbf{k})$ within the borders of $\mathbf{k}_0$ (dotted lines in figure 3.4) will be transmitted. The larger frequency

components $|\mathbf{k}_{sample}| \geq |\mathbf{k}_0|$ are not transmitted. Therefore the resulting image lacks these larger frequencies and the small image components associated with these frequencies, thus missing details in the real image that are smaller than Δx.

Figure 3.5 describes the case of nonsaturated structured illumination. Part (A) shows the Fourier transfom of the dye distribution $\hat{\rho}_{dye}(\mathbf{k})$, Part (B) the Fourier transform of the fluorescence emission probability $\hat{F}_{prob}(I_{max}, \mathbf{k})$ following non-saturated and structured illumination of depleting or exciting light (inset). Nonsaturated illumination means that the relationship between illumination intensity $I(\mathbf{x})$ and fluorescence emission probability is still linear (see 3.1 and 3.2 at lowest displayed illumination intensity $I_{max} = 0.1 \cdot I_0$). Therefore, fluorescence emission probability follows a sine squared pattern. The Fourier transform of a sine squared function is the sum of three delta peaks at 0 and $\pm\mathbf{k}_I$, where $|\mathbf{k}_I| = 2\pi/D$ is the pattern frequency:

$$\hat{F}_{prob}(\mathbf{k}) = c_{-1} \cdot \delta(\mathbf{k} + \mathbf{k}_I) + c_0 \cdot \delta(\mathbf{k}) + c_{+1} \cdot \delta(\mathbf{k} - \mathbf{k}_I) \tag{3.8}$$

The Fourier coefficients of the delta peaks are determined by the Fourier transform and are $|c_{-1}| = |c_1| = 1/2 \cdot c_0$ (see appendix A.2.5 for the derivation of these components). For simplicity only the amplitudes of the complex Fourier coefficients c_{-1}, c_0 and c_{+1} are shown and the phase φ will be ignored for the moment. To determine the fluorescence emitted by the sample in Fourier space $\hat{S}(\mathbf{k})$, the fluorescence emission probability $\hat{F}_{prob}(\mathbf{k})$ and the dye distribution $\hat{\rho}_{dye}(\mathbf{k})$ have to be convolved, according to equation 3.7:

$$\begin{aligned}
\hat{S}(\mathbf{k}) &= c_{-1} \cdot \hat{\rho}_{dye}(\mathbf{k} + \mathbf{k}_I) + c_0 \cdot \hat{\rho}_{dye}(\mathbf{k}) + c_{+1} \cdot \hat{\rho}_{dye}(\mathbf{k} - \mathbf{k}_I) \\
&= c_{-1} \cdot \hat{\rho}_{-1}(\mathbf{k}) + c_0 \cdot \hat{\rho}_0(\mathbf{k}) + c_{+1} \cdot \hat{\rho}_{+1}(\mathbf{k}) \\
&\text{with} \\
&\hat{\rho}_{-1}(\mathbf{k}) := \hat{\rho}_{dye}(\mathbf{k} + \mathbf{k}_I) \\
&\hat{\rho}_0(\mathbf{k}) := \hat{\rho}_{dye}(\mathbf{k}) \\
&\hat{\rho}_{+1}(\mathbf{k}) := \hat{\rho}_{dye}(\mathbf{k} - \mathbf{k}_I)
\end{aligned} \tag{3.9}$$

That means that the dye distribution function $\hat{\rho}_{dye}(\mathbf{k})$ is once shifted to the left ($+\mathbf{k}_I$) and multiplied by $c_{-1}(\varphi)$ and shifted to the right ($-\mathbf{k}_I$) and multiplied by $c_{+1}(\varphi)$ (see two red curves in figure 3.5 (C)). The two shifted functions are renamed $\hat{\rho}_{-1}(\mathbf{k})$ and $\hat{\rho}_{+1}(\mathbf{k})$, respectively. Multiplication with the OTF $\hat{h}(\mathbf{k})$ (see equation 3.6) results in the image $\hat{B}(\mathbf{k})$:

$$\hat{B}(\mathbf{k}) = c_{-1} \cdot \hat{\rho}_{-1}(\mathbf{k}) \cdot \hat{h}(\mathbf{k}) + c_0 \cdot \hat{\rho}_0(\mathbf{k}) \cdot \hat{h}(\mathbf{k}) + c_{+1} \cdot \hat{\rho}_{+1}(\mathbf{k}) \cdot \hat{h}(\mathbf{k}) \tag{3.10}$$

As $\hat{h}(\mathbf{k})$ is nonzero only for frequencies within the region of support $|\mathbf{k}| \leq \mathbf{k}_0$ the three dye density functions will only partially be transmitted within $-\mathbf{k}_0 \leq \mathbf{k} \leq \mathbf{k}_0$. This implies that the original dye distribution function $\hat{\rho}_{dye}(\mathbf{k})$ is known over different domains:

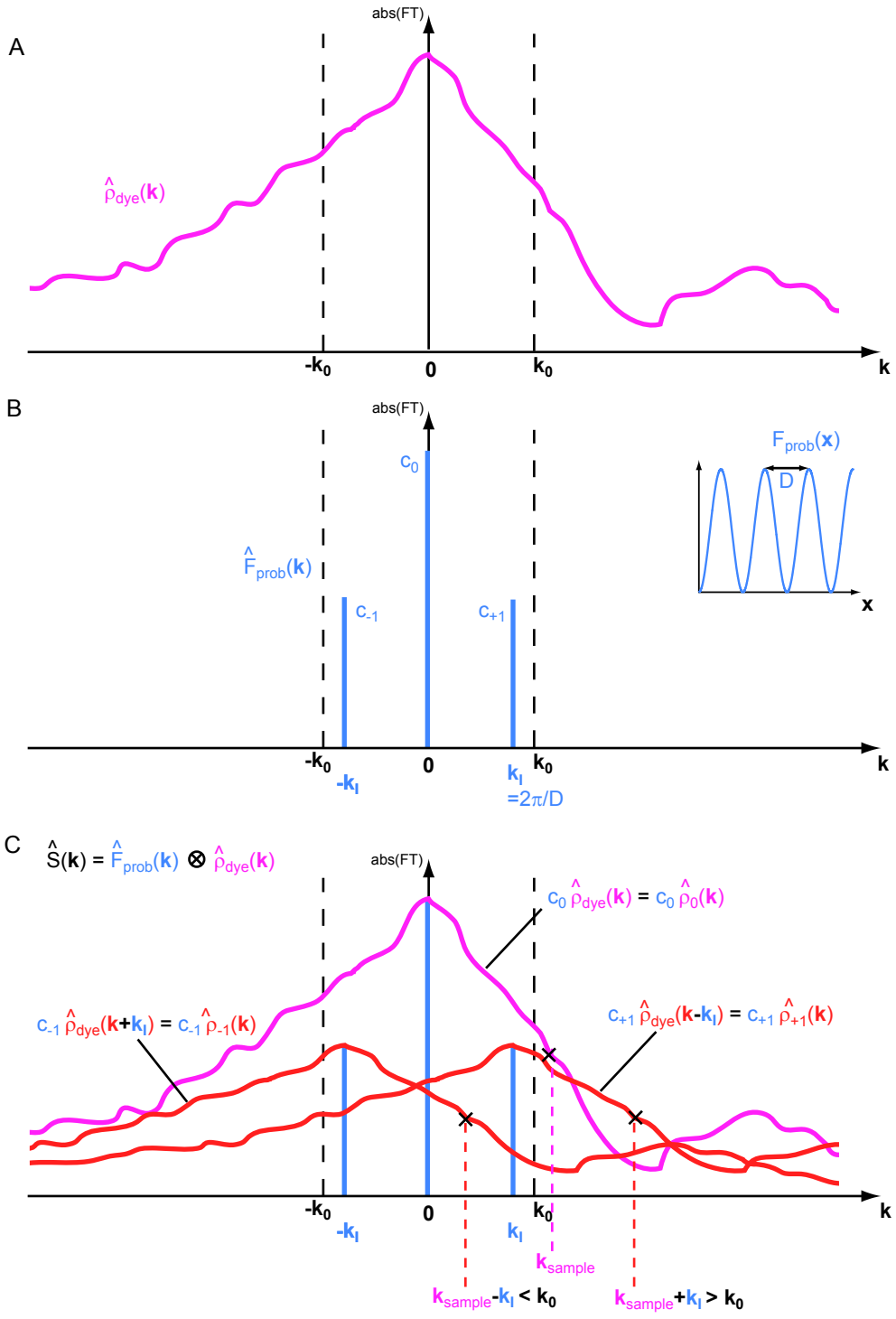

Figure 3.5: **Imaging process in Fourier Space with non-saturated structured depletion illumination**; (A): Fourier transfrom of a possible dye distribution ρ_{dye}, (B) : Fourier transform of the sine squared fluorescence emission probability pattern F_{prob} (inlay) with three deltapeaks, (C): Convolution of $\hat{\rho}_{dye}(\mathbf{k})$ and $\hat{F}_{prob}(\mathbf{k})$, the three components due to the three deltapeaks are shown, not the total sum. The amplitude at a certain sample frequency $\mathbf{k}_{sample}$ is shifted into the region of support by $\mathbf{k}_{sample} \pm \mathbf{k}_I$.)

$$\begin{aligned}
\hat{\rho}_{dye}(\mathbf{k}) &= \hat{\rho}_{-1}(\mathbf{k}-\mathbf{k}_I) && for -\mathbf{k}_0-\mathbf{k}_I \leq \mathbf{k} \leq \mathbf{k}_0-\mathbf{k}_I \\
\hat{\rho}_{dye}(\mathbf{k}) &= \hat{\rho}_{0}(\mathbf{k}) && for -\mathbf{k}_0 \leq \mathbf{k} \leq \mathbf{k}_0 \\
\hat{\rho}_{dye}(\mathbf{k}) &= \hat{\rho}_{+1}(\mathbf{k}+\mathbf{k}_I) && for -\mathbf{k}_0+\mathbf{k}_I \leq \mathbf{k} \leq \mathbf{k}_0+\mathbf{k}_I
\end{aligned} \tag{3.11}$$

From these partial functions the original dye distribution $\hat{\rho}_{dye}(\mathbf{k})$ can be reconstructed over a larger area $-\mathbf{k}_0-\mathbf{k}_I \leq \mathbf{k}_{sample} \leq \mathbf{k}_0+\mathbf{k}_I$, in comparison to $-\mathbf{k}_0 \leq \mathbf{k}_{sample} \leq \mathbf{k}_0$ in the diffraction limited case. This implies that more frequencies are accessible and the image of the dye distribution exhibits more details. For example the frequency $\mathbf{k}_{sample}$ (see figure 3.5 (C)) is larger than $\mathbf{k}_0$ and is therefore lost during the conventional imaging process. But by illuminating the sample with the sine squared pattern, the frequency $\mathbf{k}_{sample}$ gets shifted by $\pm\mathbf{k}_I$, so that $|\mathbf{k}_{sample}-\mathbf{k}_I| \leq \mathbf{k}_0$. The amplitude associated with $\mathbf{k}_{sample}$ can now be determined, taking into account that it has been multiplied by c_{-1}.

To be able to reconstruct the original dye distribution $\hat{\rho}_{dye}(\mathbf{k})$, the three partial dye distribution functions $\hat{\rho}_0(\mathbf{k})$, $\hat{\rho}_{+1}(\mathbf{k})$ and $\hat{\rho}_{-1}(\mathbf{k})$ must be determined. It is not possible to determine these from one single image $\hat{B}(\mathbf{k})$. For three unknowns at least three different images $\hat{B}(\mathbf{k})$ with different phases, φ_1, φ_2 and φ_3, have to be taken. Different phases mean different postitions of the minima of the sine squared pattern. The phase of the sine squared pattern is reflected in the Fourier coefficients $c_0(\varphi)$, $c_{+1}(\varphi)$ and $c_{-1}(\varphi)$. The result is a set of linear equations from which the three unknowns $\hat{\rho}_0(\mathbf{k})$, $\hat{\rho}_{+1}(\mathbf{k})$ and $\hat{\rho}_{-1}(\mathbf{k})$ can be deduced:

$$\begin{aligned}
\hat{B}(\mathbf{k},\varphi_1) &= |c_{-1}| \cdot e^{-\mathrm{i}\,\varphi_1} \cdot \hat{\rho}_{-1}(\mathbf{k}) \cdot \hat{h}(\mathbf{k}) + |c_0| \cdot \hat{\rho}_0(\mathbf{k}) \cdot \hat{h}(\mathbf{k}) + |c_{+1}| \cdot e^{-\mathrm{i}\,\varphi_1} \cdot \hat{\rho}_{+1}(\mathbf{k}) \cdot \hat{h}(\mathbf{k}) \\
\hat{B}(\mathbf{k},\varphi_2) &= |c_{-1}| \cdot e^{-\mathrm{i}\,\varphi_2} \cdot \hat{\rho}_{-1}(\mathbf{k}) \cdot \hat{h}(\mathbf{k}) + |c_0| \cdot \hat{\rho}_0(\mathbf{k}) \cdot \hat{h}(\mathbf{k}) + |c_{+1}| \cdot e^{-\mathrm{i}\,\varphi_2} \cdot \hat{\rho}_{+1}(\mathbf{k}) \cdot \hat{h}(\mathbf{k}) \\
\hat{B}(\mathbf{k},\varphi_3) &= |c_{-1}| \cdot e^{-\mathrm{i}\,\varphi_3} \cdot \hat{\rho}_{-1}(\mathbf{k}) \cdot \hat{h}(\mathbf{k}) + |c_0| \cdot \hat{\rho}_0(\mathbf{k}) \cdot \hat{h}(\mathbf{k}) + |c_{+1}| \cdot e^{-\mathrm{i}\,\varphi_3} \cdot \hat{\rho}_{+1}(\mathbf{k}) \cdot \hat{h}(\mathbf{k})
\end{aligned} \tag{3.12}$$

Solving this system of linear equations allows the reconstruction of the dye distribution $\hat{\rho}_{dye}(\mathbf{k})$ for frequencies $-\mathbf{k}_0-\mathbf{k}_I \leq \mathbf{k}_{sample} \leq \mathbf{k}_0+\mathbf{k}_I$. The highest transmittable frequency would be $\pm(\mathbf{k}_0+\mathbf{k}_I)$. As the illuminating light is diffraction limited as is the emitted light, the highest possible frequency for the illuminating sine squared pattern is $\mathbf{k}_I = \mathbf{k}_0$. This leads to a possible resolution enhancement of a factor of two[2] using nonsaturated sine squared structured illumination, as previously described by Heintzmann et al. and Gustaffson et al. ([26], [27], [28], [22]).

Equation 3.11 presents the domains for which each partial dye distribution function is known. These domains overlap partially and therefore fewer boundary conditions are necessary. It is sufficient to image at two phase positions rather than three to reconstruct the better resolved image.

[2]The possible frequency of the sine squared pattern k_I is determined by the wavelength of the structured light, but due to the blurring during the detection process, the restriction on k_I stems from the wavelength of the fluorescence λ_{em}.

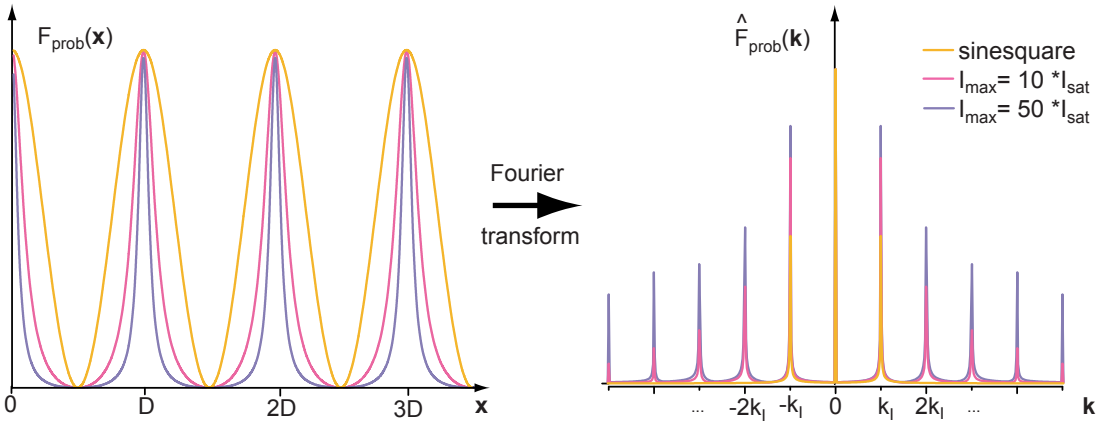

Figure 3.6: **Saturated sine squared funtions and their Fourier transforms**: Fluorescence emission probability pattern $F_{prob}(\mathbf{x})$ at three different depletion intensities (left) and their Fourier transforms (right). The higher the depletion intensity the higher the amplitude of the contributing side-deltapeaks. The distance of the interference maxima D and the frequency k_I are coupled by $\mathbf{k}_I = 2\pi/D$.

In the case of saturated structured illumination and fluorescence depletion the applied principle is the same. Again the sample fluorescence $S(\mathbf{x})$ and its Fourier transform have to be determined. According to equation 3.7, $\hat{S}(\mathbf{k})$ is the convolution of the fluorescence emission probability $\hat{F}_{prob}(I_{max}, \mathbf{k})$ and the dye distribution $\hat{\rho}_{dye}(\mathbf{k})$. In figure 3.6 three sine squared illumination patterns and their Fourier transforms are shown as an example. In the case of low saturation there are only three delta peaks, as described before. When the depletion intensity and thus the saturation degree is increased, more peaks appear in the Fourier transforms at multiples of the pattern frequency $\mathbf{k}_I = 2\pi/D$. The Fourier coefficients c_n of the peaks at $n \cdot \mathbf{k}_I$ get more prominent with increasing intensity. Therefore the Fourier transform of a saturated sine squared pattern can be described as a sum of delta peaks with the coefficients c_n (see appendix A.2.5):

$$\hat{F}_{prob}(\mathbf{k}) = \sum_n c_n \cdot \delta(n \cdot \mathbf{k}_I) \qquad n \in Z \tag{3.13}$$

According to equation 3.7 the fluorescence emission probability $\hat{F}_{prob}(I_{max}, \mathbf{k})$ and the dye distribution $\hat{\rho}_{dye}(\mathbf{k})$ have to be convolved to determine the fluoresence signal from the sample $\hat{S}(\mathbf{k})$:

$$\begin{aligned} \hat{S}(\mathbf{k}) &= \sum_n c_n \cdot \hat{\rho}_{dye}(\mathbf{k} - n \cdot \mathbf{k}_I) \qquad n \in Z \\ &= \sum_n c_n \cdot \hat{\rho}_n(\mathbf{k}) \\ &\text{with} \\ &\hat{\rho}_n(\mathbf{k}) := \hat{\rho}_{dye}(\mathbf{k} - n \cdot \mathbf{k}_I) \end{aligned} \tag{3.14}$$

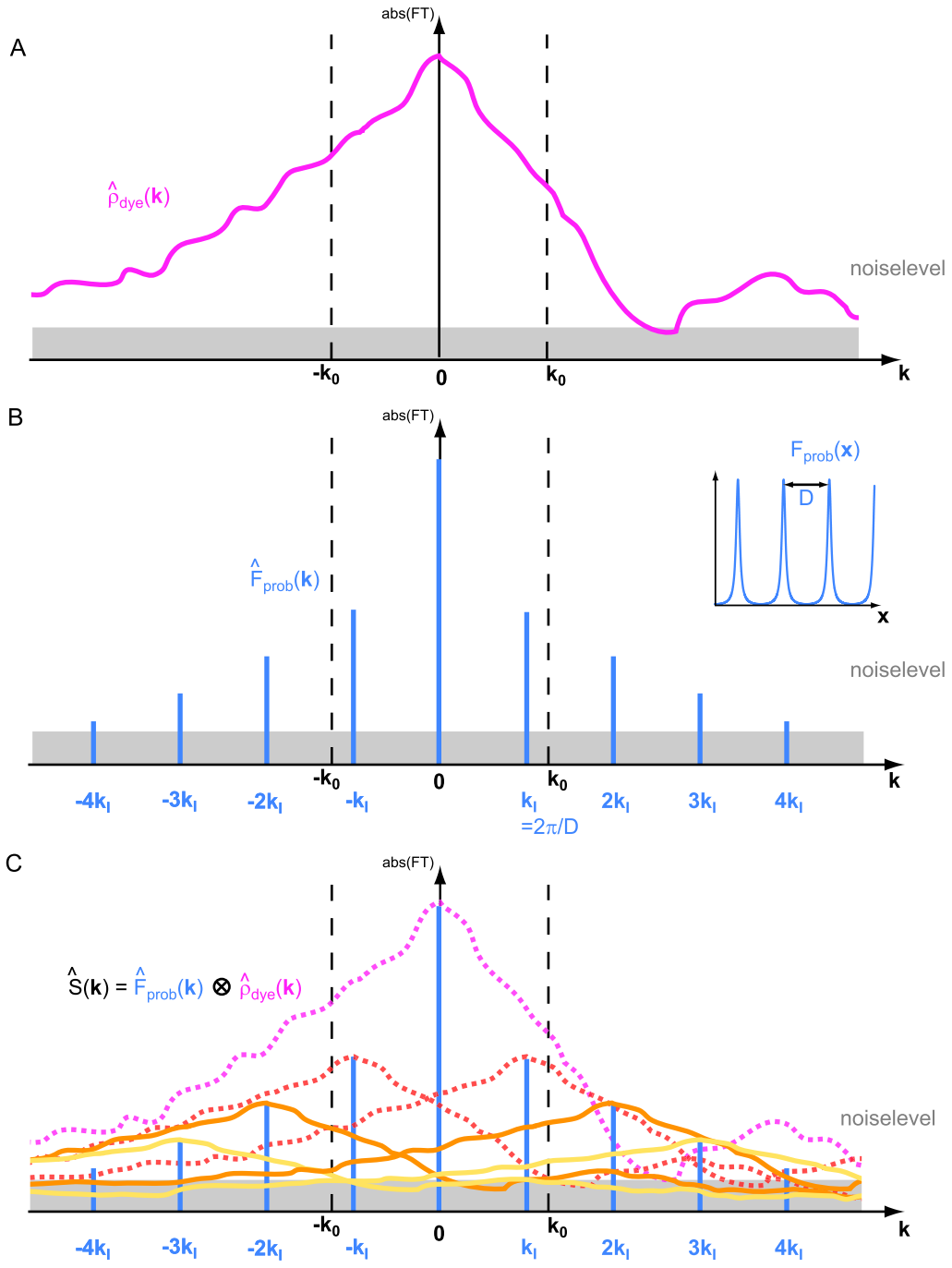

Figure 3.7: **Imaging process in Fourier Space with saturated structured depletion illumination**; (A): Fourier transfrom of a possible dye distribution ρ_{dye}, (B) : Fourier transform of the saturated sine squared fluorescence emission probability pattern F_{prob} with more deltapeaks (inlay), (C): Convolution of $\hat{\rho}_{dye}(\mathbf{k})$ and $\hat{F}_{prob}(\mathbf{k})$, for simplicity only the components due to the deltapeaks are shown, not the total sum.

As in the linear case, the dye distribution function $\hat{\rho}_{dye}(\mathbf{k})$ is shifted by multiples of $\mathbf{k}_I$, multiplied with the Fourier coefficients c_n of the saturated pattern (see figure 3.7) and added up. For simplicity, only the contributing parts of $\hat{S}(\mathbf{k})$ are shown, not the sum. During the imaging process the signal from the sample has to be multiplied with the OTF $\hat{h}(\mathbf{k})$ (see equation 3.6):

$$\begin{aligned} \hat{B}(\mathbf{k}) &= \hat{S}(\mathbf{k}) \cdot \hat{h}(\mathbf{k}) \\ &= \sum_n c_n \cdot \hat{\rho}_n(\mathbf{k}) \cdot \hat{h}(\mathbf{k}) \qquad\qquad n \in Z \end{aligned} \tag{3.15}$$

Only the parts of the partial functions $\hat{\rho}_n(\mathbf{k})$ that are within the borders of the region of support $-\mathbf{k}_0 \leq \mathbf{k} \leq \mathbf{k}_0$ can be transmitted. This means that other frequency domains than $|\mathbf{k}| \leq \mathbf{k}_0$ of the original dye distribution function $\hat{\rho}_{dye}(\mathbf{k})$ are transmitted from the sample $\hat{S}(\mathbf{k})$:

$$\hat{\rho}_{dye}(\mathbf{k}) = \hat{\rho}_n(\mathbf{k} + n \cdot \mathbf{k}_I) \qquad for - \mathbf{k}_0 + n \cdot \mathbf{k}_I \leq \mathbf{k} \leq \mathbf{k}_0 + n \cdot \mathbf{k}_I \tag{3.16}$$

From these partials dye distribution functions the original dye distribution function can be reconstructed over a larger range of spatial frequencies than in the diffraction limited case. The higher transmitted frequency components lead to higher resolution and thus to a more detailed image.

In order to determine the unknown functions $\hat{\rho}_n(\mathbf{k})$ and thus $\hat{\rho}_{dye}(\mathbf{k})$, several images $\hat{B}(\mathbf{k})$ have to be taken at different phase positions φ_j (analog to the linear case). The resulting system of linear equations will be:

$$\begin{aligned} \hat{B}(\mathbf{k}, \varphi_j) = \sum_{n=-N}^{N} |c_n| \cdot e^{-\mathrm{i}\varphi_j} \cdot \hat{\rho}_n(\mathbf{k}) \cdot \hat{h}(\mathbf{k}) \\ \text{with } n \leq N \in Z, j = 0, \cdots + m \end{aligned} \tag{3.17}$$

The frequency $N \cdot \mathbf{k}_I$ is the highest frequency of the saturated sine squared pattern for which $c_N \cdot \hat{\rho}_N(\mathbf{k})$ is above the noise level, depicted in figure 3.7 as the grey area in case of white noise. In the figure this would be $N = 3$. The delta peaks for $n = 4$ and $n = -4$ are shown as well, but are already hidden within the noise and can therefore not contribute to resolution enhancement. By further increasing the depletion intensity and thus a better saturated sine squared pattern, the Fourier coefficients c_n increase (see figure 3.6), leading to a rise of c_n above the noise level up to larger N, accessing larger $\mathbf{k}$ and thus higher resolution. The domain over which the original dye distribution function $\hat{\rho}_{dye}(\mathbf{k})$ can be reconstructed is: $-\mathbf{k}_0 - N \cdot \mathbf{k}_I \leq \mathbf{k} \leq \mathbf{k}_0 + N \cdot \mathbf{k}_I$. This leads to a N-fold resolution enhancement.

To solve the system of linear equations 3.17 with $2N + 1$ unknowns it is in principle necessary to have $2N + 1$ equations, and therefore measure at $2N + 1$ phase positions ($m =$

$2N + 1$). However, analog to the linear case there is an overlap of the $2m + 1$ partial dye distribution functions $\hat{\rho}_n(\mathbf{k})$. This reduces the amount of necessary boundary conditions and thus the necessary amount of phase positions.

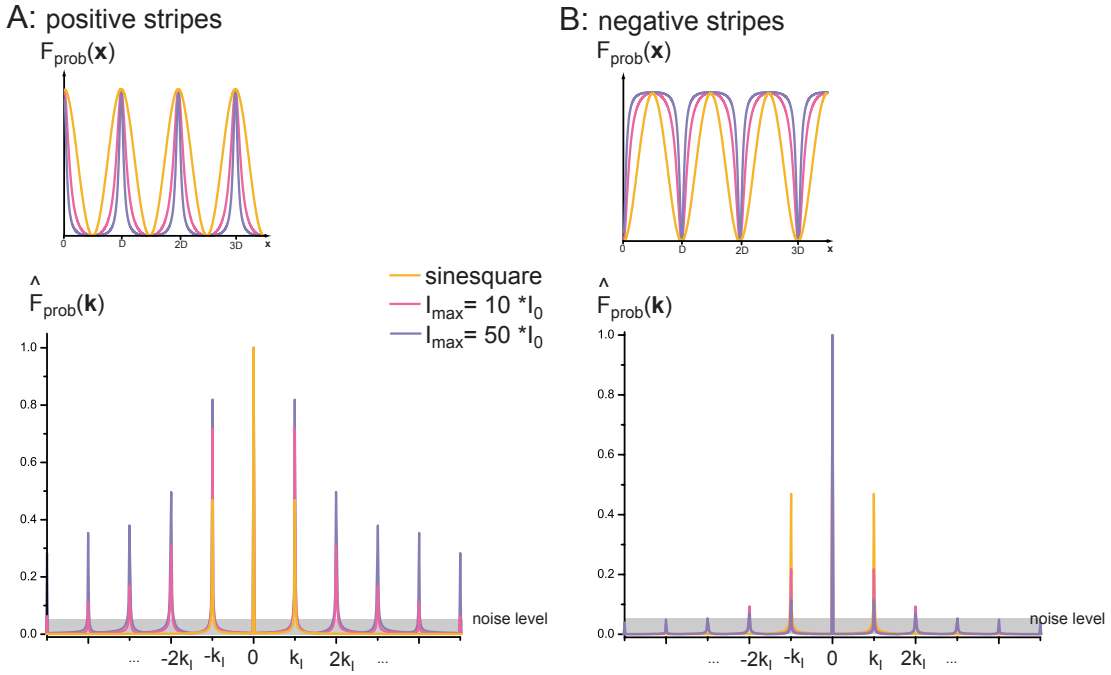

Figure 3.8: **Comparison of Fourier coefficients for *positive* (A:) and *negative* (B:) stripes** in real space (upper part) and in Fourier Space (lower part) at different saturation factors with a certain level of noise.

The considerations about saturated structured illumination are the same for the case of positive stripes (fluorescence depletion) and for the case of negative stripes (fluorescence saturation). In both cases, it is necessary to know the coefficients c_n of the Fourier transform of the fluorescence emission probability $\hat{F}_{prob}(\mathbf{k})$ (compare equation 3.13 and figure 3.8). The deltapeak at frequency 0 stands for a constant, position-independent signal in real space. In the case of negative stripes, the fluorescence emission probability $F_{prob}(\mathbf{x})$ is generally high apart from dips to zero at the minima of the illumination pattern (see inlay in (B)). Therefore the constant term c_0^{neg} is very large in comparison to the other coefficients c_n^{neg} ($n \neq 0$). In the lower part of (B) the coefficients c_n^{neg} can be seen. They have been normalized to c_0^{neg}. In (A) positive stripes and their Fourier transform can be seen (again normalized to the constant term c_0^{pos}). Comparing (A) and (B) shows that the coefficients c_n^{pos} are larger than the coefficients c_n^{neg}. The higher the Fourier coefficients c_n the better can high frequencies be transmitted after having been multiplied with the respective c_n. Therefore noise is a bigger issue for imaging with negative stripes than with positive stripes, as was already stated.

The theory of imaging with a structured illumination pattern in combination with fluorescence saturation and fluorescence depletion (positive stripes) has been addressed using real space and Fourier space calculations. Because of noise the use of fluorescence depletion is preferable. However, the saturation behaviour depends on dye properties - some dyes

do not show saturation of depletion, others cannot be saturated with the powers available. Therefore the optimal saturation behaviour must be found for the dye in question. In theory, unliminted resolution is possible by driving the saturation to higher and higher values, thus bringing higher frequency components of c_n above the noise level. Experimentally, resolution is limited by the available power, bleaching and noise. While exposing the sample to high levels of light, bleaching becomes increasingly probable. This leads both to possible artifacts and to a reduction in signal, having the negative effect of hiding the high frequency components of c_n within the noise.

3.1.2 Experimental Implementation

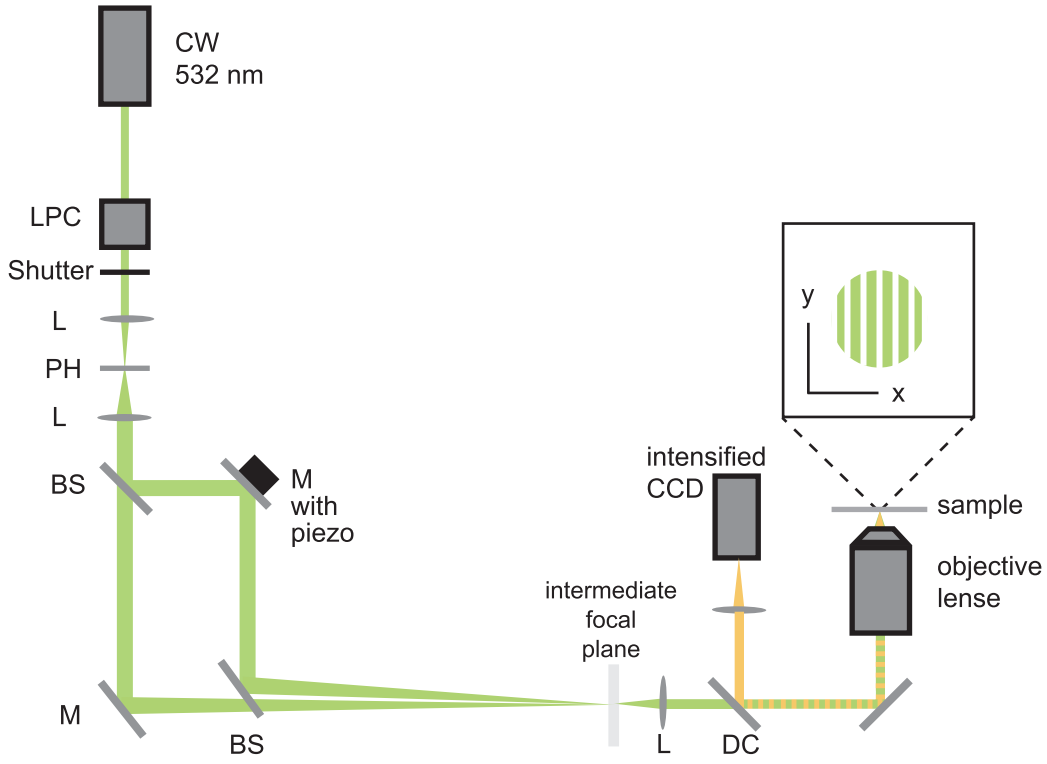

Figure 3.9: **Experimental Setup for the implementation of parallelized RESOLFT.** For exact description of the components see chapter 4.1.

Experimentally the sine squared illumination pattern is achieved by having two beams of the same intensity interfere at the sample plane: a laserbeam is separated into two beams

of the same intensity that are recombined at the sample under a certain angle α.

To make sure that the beam profile is homogeneous the light from a frequency-doubled Nd:YAG laser ($523nm$) is directed through a clean-up system consisting of two lenses and a small pinhole. A laser power controller and a fast shutter have been added before the clean-up to control the intensity of the beam and the exposure time. The beam is split by a 50:50 beam splitter and combined again using another 50:50 beam splitter and two mirrors (lower left corner of figure 3.9). The width D of the interference stripes is determined by the angle α between the two beams as $D = \lambda/(2sin(\alpha/2))$. It can easily be adjusted using the two mirrors and beam splitters in the so-called interference cavity. One of the mirrors in the cavity is mounted onto a piezo-actuator, which allows control of the retardation in one beam in respect to the other and therefore the phase. The two beams interfere in the intermediate focal plane, where they can directly be imaged using an imaging chip (from a standard webcam) to check if the two single spots overlap exactly. To achieve optimal minima – zeros of the interfernce pattern – it is also important to take care of the polarisation of the two single beams, which should be perpendicular to the optical plane spanned by the incoming beams. With other orientations of the polarization (either not perpendicular to the optical plane or not parallel to each other) there will be polarisation components that cannot interfer and therfore lead to non-zero interference minima. Behind the intermediate focal plane the two single beams enter a standard fluorescence microsope via a tubular lens of focal length $f = 200$ and a dichroic mirror which is mounted directly underneath the objective lens. The interference stripes of the intermediate focal plane are demagnified into the focal plane by a factor of 100 or 63 (depending on the combination of tubular and objective lens). The emitted fluorescence light from the sample is collected by the standard fluorescence microscope and imaged by a tubular lens onto a microchip camera.

Using the interference of two beams to create a structured illumination pattern for RESOLFT will increase resolution perpendicular to the stripes but not alter it along the direction of the stripes. There are several possibilites to apply paralleliziation to two dimenstions, which will be discussed later.

3.2 Bleaching: Working at low temperatures

To counteract the problem of bleaching at high illumination intensities the sample was evacuated and cooled down using liquid nitrogen and a standard cryostat for optical microscopy (ST-500-LN, Janis Research Corporation Inc., Wilmington, USA). Photoinduced bleaching is a chemical reaction of the dye molecule in a higher excited state (triplet or singlet) with another molcules in the environment – preferably oxygen, which is a highly reactive molecule. Evacuation reduces the amount of ambient oxygen and cooling decreases chemical reaction constants ([18]), therefore both effects leading to a reduction in bleaching.

The following traces were all taken with a homogeneous illumination spot and an avalanche photo diode for detecting fluorescence emission over time. The reaction leading to the loss in fluorescence is irreversible, waiting before another exposere did not recover fluorescence.

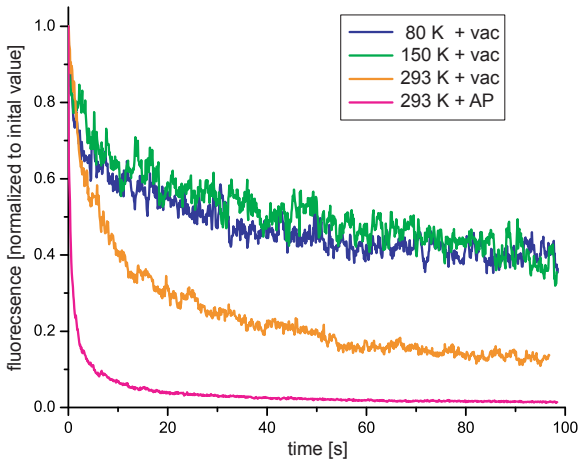

Figure 3.10: **Irreversible Photobleaching at different temperatures.** Bleaching of beads labeled with Atto532 at different temperatures due to exposure to green light with an illumination intensity $I \approx 750 W/cm^2$.

The effect of evacuation ($< 10^{-5}\ mbar$) and cooling ($\geq 80\ K$) on the bleaching behaviour of Atto532 labeled beads during continuous laser exposure is shown in figure 3.10. At atmospheric conditions (temperature $293\,K$ and atmospheric pressure) $\approx 90\,\%$ of the dye molecules are bleached within the first five seconds (pink trace). Evacuation of the sample already leads to a significant decrease of bleaching (orange trace, $\approx 40\ \%$ residual fluorescence after $10\ s$ of exposure), which is due to the absence of oxygen. One major bleaching mechanism is the reaction of the dye molecule in its triplet state with ambient oxygen ([29], [18]). The ground state of oxygen is the triplet state, which makes it very reactive, especially with other molecules in triplet states, thus leading to photodestruction of the dye. The absence of ambient oxygen reduces such bleaching reactions. Decrease of the sample temperature leads to further reduced bleaching, with a residual level of $\approx 60\,\%$ after $10\,s$ both for $150\,K$ and $80\,K$ (green and blue traces, respectively). This is due the fact, that the bleaching probability decreases with temperature ([18]). The normalized traces in figure 3.10 display a higher noise level for the fluorescence signal detected at evacuation and low temperatures compared to measurements taken at $293\ K$ and atmospheric pressure. The reason is that fluorescence emitted by the sample is lower at vacuum conditions and low temperatures due to higher triplet build-up (see chapter 3.3), since lower oxygen content does not only result in less bleaching but also in less quenching of the triplet state.

To simulate measurement conditions used during imaging (see chapter 4.1) the sample was repeatedly exposed to the laser light for $100\ ms$ at a repetition frequency of $1\ Hz$ (see 3.11). For room temperature and atmospheric pressure (pink trace) there is almost no difference to figure 3.10: after five seconds of exposure, that is 50 exposures of $100\ ms$ each, $\approx 90\ \%$ of the dye molecules are bleached. In the cases of the evacuated samples repeated

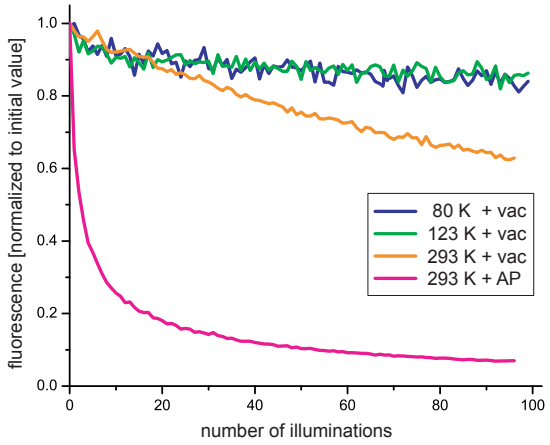

Figure 3.11: **Irreversible Photobleaching at different temperatures.** Bleaching of beads stained with Atto532 at different temperatures and pressure conditions, due to repetitive exposure to green light of an illumination intensity $I = \approx 750\, W/cm^2$; single exposure time was $100\, ms$, the repetition rate $1\, Hz$

exposure with a repetition frequency of $1\, Hz$ leads to reduced bleaching. After $10\, s$ of total exposure (100 exposures of $100\, ms$ each) the residual fluorescence was $\approx 60\, \%$ at vacuum and room temperature (orange trace) and $\approx 85\, \%$ for vacuum and $123\, K$ (green trace) and $80\, K$ (blue trace), which is the same amount of bleaching as with continous illumination from figure 3.10. The time between single exposures allowed the dye molecules in the triplet state to relax to the ground state before the next laser exposure, leading to less bleaching than continous illumination ([30]).

In conclusion, bleaching is reduced by evacuation and cooling of the sample, but at the same time there is more triplet build-up due to a higher triplet lifetime τ_T. Details of these photophysical and chemical behaviours will be adressed in the following section.

3.3 Photophysics

As a result of different ambient conditions like evacuation and cooling, the photokinetics of the dye are altered, especially the triplet relaxation rate k_T is decreased. This leads to a higher population of the triplet state, the possibility of draining the triplet state with laser light and the possibility of saturaing fluorescence depletion.

Population of the Triplet State

At vacuum conditions ($<10^{-5}\, mbar$) a sudden decrease in fluorescence upon illumination can be detected for all dyes tested. Figure 3.12 shows this fluorescence decrease over time for beads labeled with Atto532. It very much resembles the bleaching behaviour discussed in the previous section. In contrast to figure 3.10) the illumination time is much shorter $s \leftrightarrow ms$ in the above figure. In contrast to bleaching, the sudden drop in fluorescence is reversible when the sample is illuminated again after a delay of e.g. $2\, s$, which means that a

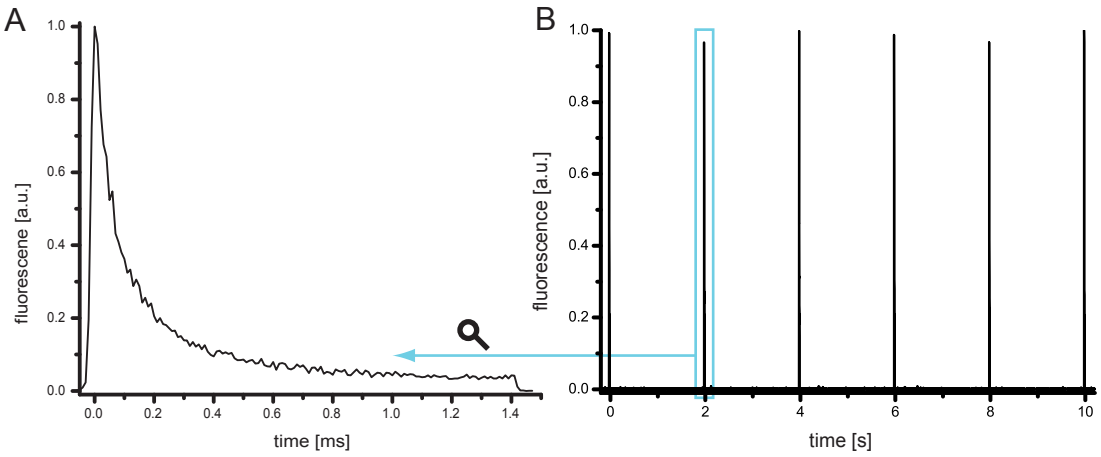

Figure 3.12: **Reversible fluorescence loss at vacuum and low temperature.** (A): fluorescence decrease over time due to triplet population in beads labeled with Atto532 at 80 K and vacuum conditions (<$10^{-5} mbar$), illumination intensity $I \approx 627\ W/cm^2$; (B) : complete recovery of the fluorescence after a drak period of 2 s measured with an illumination intensity $I \approx 505\ W/cm^2$.

reversible non-fluorescent state is involved. At room temperature and atmospheric pressure the initial decrease is almost not discernible within the noise (see figure 3.13). The different behaviours shown in figures 3.12 and 3.13 are mainly due to evacuation and less due to the decrease in temperature.

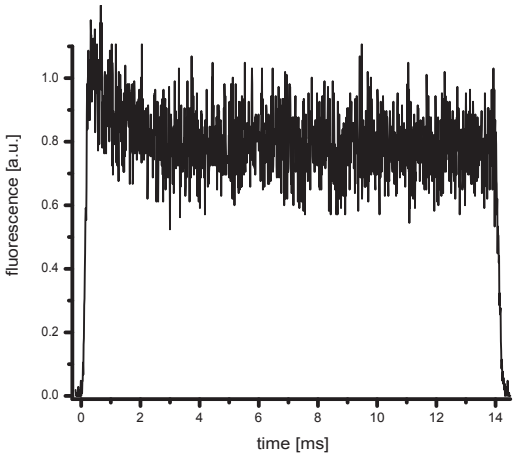

Figure 3.13: **Little fluorescence loss at room temperature and atmospheric pressure.** Almost no loss of fluorescence due to triplet population of beads labeles with Atto532 at 300 K and atmospheric pressure, illumination intensity $I \approx 627\ W/cm^2$

As fluorescence recovered fully after a certain dark period which strongly depends on

the ambient conditions, the drop in fluorescence is not irreversible photodestruction, but a population of the non-fluorescent triplet or another dark state. A constant factor of the molecules in the first excited state S_1 spontaneously cross over to the lowest triplet state T_1 (inter-system-crossing **ISC**), so they cannot take part in the fluorescing cycle between $S_0 \Leftrightarrow S_1$ for the time they are trapped in T_1. The transition from T_1 back to S_0 is spin-forbidden, therefore exhibiting a rather long triplet lifetime τ_T (in the range of μs to s compared to the ns lifetime of S_1), and therfore a small triplet relaxation rate k_T (see chapter 2 and figure 2.9). The *triplet relaxation* rate constant k_T strongly depends on the environment of the dye. Evacuation of the sample, the lack of oxygen, which is a strong triplet quencher, leads to a decrease of the triplet relaxation rate k_T. The level to which the fluorescence drops is the steady state fluorescence due to a certain illumination intensity I and is given by equation 2.7. It depends on the rate of ISC k_{ISC} and the triplet relaxation rate k_T. With no ISC there would be no build-up of the triplet population and therefore no drop in fluorescence. With no triplet relaxation ($k_T = 0$), the fluorescence would drop to zero, because in the steady state all dye molecules would reside in the triplet. In an environment with triplet quenchers, for example oxygen in the non-evacuated sample of 3.13, the triplet relaxation is much faster than in an evacuated sample ($\mu s \approx \tau_T(\mathrm{w\ O_2}) \prec \tau_T(\mathrm{w/o\ O_2}) \approx s$), that the resulting reduction in fluorescence of $20\ \%$.

Relaxation of the Triplet State

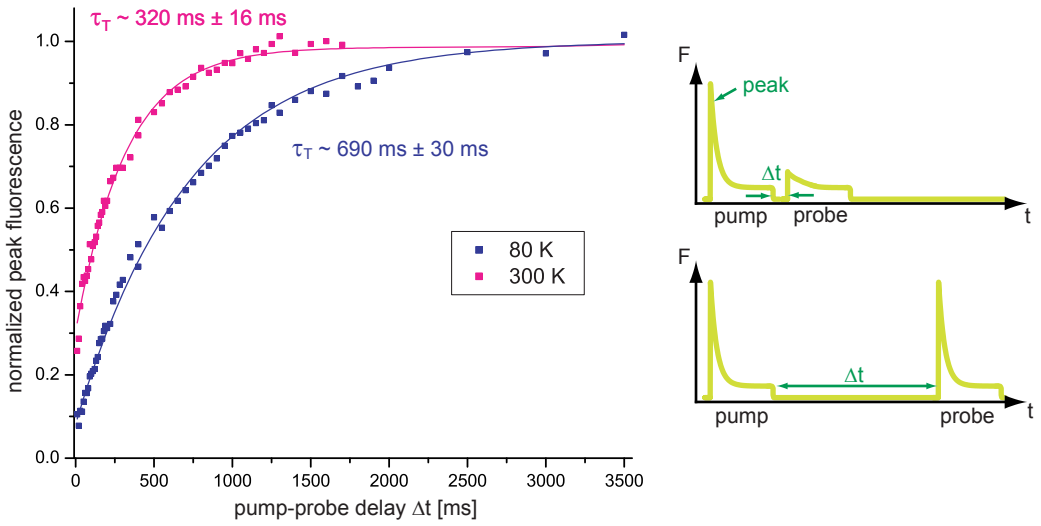

Figure 3.14: **Fluorescence recovery at different temperatures.** Fluorescence (and therefore triplet) recovery of beads labeled with Atto532 at $80\ K$ and $300\ K$ and vacuum conditions (<10^{-5}); the recovery was meaured at an illumination intensity $I \approx 420\ W/cm^2$ with a first pulse (pump) populating the triplet and a second pulse (probe) after a delay time Δt (depicted on the right).

As seen in figure 3.12 the decrease in intensity is reversible. Figure 3.14 shows the triplet relaxation at vacuum conditions at $80\ K$ and $300\ K$ respectively. For noise reduction each

displayed value is an average over 100 single measurements. First the sample was exposed to illuminating light of $\approx 420\ W/cm^2$ for $50\ ms$ to make sure the steady state was reached. This first pulse will be called the *pump pulse*. After a certain delay period the sample was exposed to a second pulse (the *probe pulse*) of the same power density for another $50\ ms$. The peak fluorescence of the probe pulse is normalized to the peak fluorescence during the pump pulse and plotted against the pump-probe delay time Δt. Only the peak value of the probe pulse could be taken, as the probe pulse itself populates the triplet. Fitting the data points with a single exponential decay leads to an estimated triplet lifetimes of $\tau_T(80K) \approx 716\ ms$ and $\tau_T(300K) \approx 320\ ms$. The associated triplet relaxation rates are $k_T(80K) = 1/\tau_T(80K) \approx 1.4\ Hz$ and $k_T(300K) = 1/\tau_T(300K) \approx 3.13\ Hz$. The triplet relaxation rate at low temperature, $k_T(80K)$, is lower because energy transfer via collisions is less likely (at room temperature and water $k_T \approx 10^5\ \frac{1}{s}$, [31]).

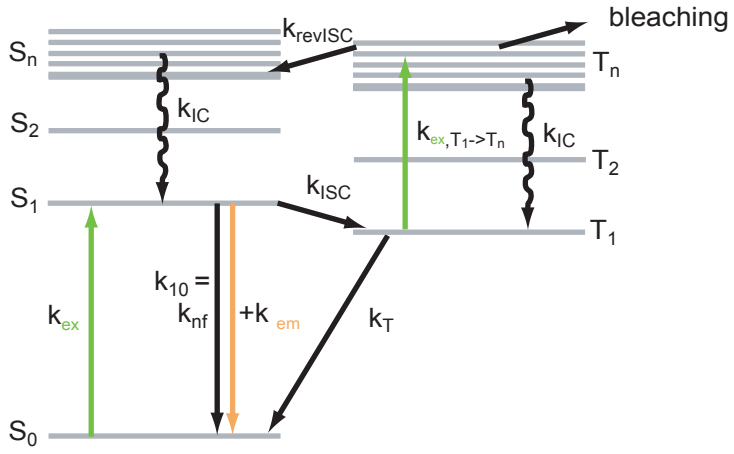

Figure 3.15: **Jablonski diagram** with the additional triplet depletion mechanism via higher excited triplet states T_n and reverse ISC.

Both graphs do not meet the abscissa at zero but at the residual fluorescence level of $8\,\%$ at $80\ K$ and $15\,\%$ at $300\ K$. This residual fluorescence level is a measure for the equilibrium between triplet population and triplet depletion at a constant illumination intensity. This equilibirium is reached when the same amount of dye molecules enter and leave the triplet state (see for example figure 3.15), and was described in chapter 2.2 by equation 2.7 as

$$F(I) \propto \frac{1}{1 + \frac{k_{ISC}}{k_T} + \frac{k_{10}+k_{ISC}}{\sigma_{ex}\cdot\gamma_{ph}\cdot I}} \tag{3.18}$$

The steady-state fluorescence depends on the excitation rate $k_{ex} = \sigma_{ex} \cdot \gamma_{ph} \cdot I$, with σ_{ex} the absroption cross-section, γ_{ph} the inverse photon energy and I the illumination intensity. The non-fluorescent rate k_{nf} and fluorescent rates k_{nf} are merged to one rate $k_{10} = k_{nf}+k_{em}$. k_{ISC} is the inter-system-crossing rate and k_T the triplet relaxation rate. The rates k_{10} and k_{ISC} are hardly affected by the environtment, unlike the triplet relaxation rate k_T. As described before, k_T is increased in the presence of triplet quenchers, and a decrease of temperature decreases k_T due to fewer collisions. Thus, the equilibrium fluorescence level mainly

depends on the illumination intensity and the ambient conditions. The inital value in figure 3.14 is the equilibrium fluorescence value for the applied pump intensity. It is lower at the lower temperature of $80\ K$ because the triplet relaxation rate k_T is lower than in the case of $300\ K$, which leads to a lower fluorescence $F(I)$ at the same applied pump intensity I.

Fluorescence Saturation with Triplet Population

As described in section 3.1.1 for RESOLFT-imaging a saturable, light driven transition between two states is necessary. **G**round **S**tate **D**epletion either saturates the tranistion from $S_0 \rightarrow S_1$ or the transition from the singlet system to the triplet system $S_0 + S_1 \rightarrow T_1$, leading in both ways to a saturated depletion of the singlet ground state S_0, and thus to a saturated depletion of possible fluorescence excitation. As stated before, the saturating mechanism depends on the photophysical properties of the dye. With the high triplet build-up at vacuum conditions and low temperatures it is expected to saturate the triplet state and thus to deplete S_0 of the fluorescence markers. Figure 3.16 plots the fluorescence signal detected from Atto532-labeled beads for different illumination intensities and for different ambient conditions, resulting in so-called *fluorescence saturation curves*.

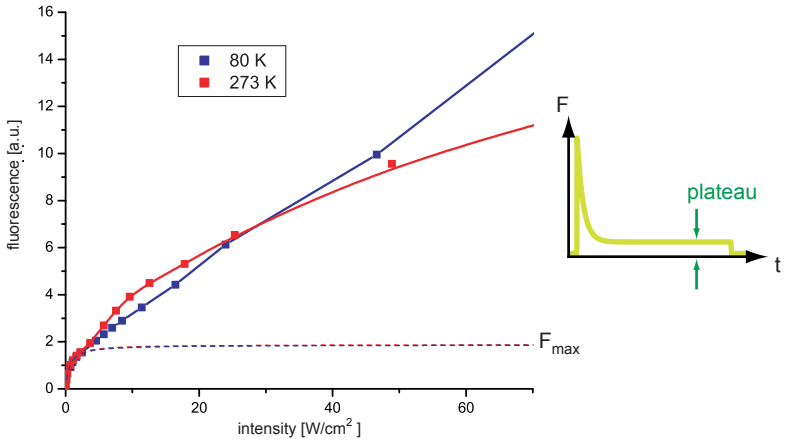

Figure 3.16: **Saturation behaviour of fluorescence emission with increasing excitation intensity.** Fluorescence at different excitation intensites detected for beads labeled with Atto532 at $80\,K$ (blue) and $273\,K$ (red) at vacuum conditions (<10^{-5}), fluorescence was determined after the initial decrease in fluorescence (plateau, see inset); the dashed lines depict the expected saturation behaviour following equation 3.19 with $I_0 \approx 0.6 W/cm^2$.

As described before, the emitted fluorescence detected after the start of illumination strongly decreases for the first ms due to population of the triplet state T_1 and reaches a plateau, that is the fluorescene at equilibrium (see inset of figure 3.16). Figure 3.16 plots

this plateau (fluorescence signal sampled during $50\ ms$ after plateau is reached) over the intensity of the illumination beam for two different temperatures ($273\ K$ red and $80\ K$ blue) at vacuum conditions. For better comparison, the fluorescence has been rescaled so that both curves are overlaid at their initial parts. As expected for a saturation behaviour (chapter 2.2) there is a linear increase in fluorescence signal for low intensities and a saturation at higher power density ($>\ 5\ W/cm^2$). The dashed lines indicate fits with the function of equation 3.18 describing this behaviour simplified to

$$\begin{aligned} &F(I) \propto F_{max} \cdot \frac{1}{1+\frac{I_0}{I}} \\ &\text{with} \\ &I_0 = \frac{k_T}{k_T + k_{ISC}} \cdot \frac{k_{10}}{\sigma_{ex} \cdot \gamma_{ph}} \\ &F_{max} \propto \frac{k_T}{k_T + k_{ISC}} \end{aligned} \tag{3.19}$$

with I_0 the saturation intensity (see chapter 2.2) and $F_{max} = \lim_{I\to\infty} F(I)$ the maximum fluorescence value. From the fit to the initial values in figure 3.16 the saturation intensity in both cases is determined as $I_0 \approx 0.6\ W/cm^2$, whereas the calculated value for $I_0 = 0.23\ W/cm^2$ using equation 2.8 from chapter 2.2 ($\sigma_{ex} \cdot \gamma_{ph} = 1030\ cm^2$, $k_{10} = 5 \cdot 10^8\ \frac{1}{s}$, $k_{ISC} = 3 \cdot 10^6\ \frac{1}{s}$ and $k_T = 1.4\ \frac{1}{s}$; see appendix for determination of those values):

$$I_0 = \frac{k_T}{k_T + k_{ISC}} \cdot \frac{k_{em} + k_{nf}}{\sigma_{ex} \cdot \gamma_{ph}}$$

Both values for I_0 agree very well taking into account, that the sampling at low intensities was poor for the displayed data.

Instead of asymptotically approaching a maximum fluorescence value F_{max}, the measured fluorescence further rises with increasing illumination intensity. The slope is smaller than in the initial region, but within the applied intensities a real plateau is not reached. This behaviour can be explained by depletion of the triplet due to the green illumination light via higher excited triplet states and reverse ISC, reverting the depletion of the singlet system and thus increasing fluorescence emission (see 3.15).

Molecules in the triplet state T_1 have a certain probability to be excited to higher excited triplet states T_n by the green illumination light via additional absorption of photons. From T_n they can either relax within the triplet system to the T_1, bleach or cross over to the singlet system, S_n, from where they relax to S_0, emitting fluorescence. The higher the excited state T_n the higher the possibility for reverse ISC, because of the higher density of states. The molecules relaxing from T_n to T_1 are still trapped in the dark triplet state and do no emit fluorescence, while molecules bleached from T_n are completely lost for fluroescence cycling. The described processes can be described by a set of rate equations (see appendix A.2.7) with the rate constants $k_{ex,T1\to Tn} = \sigma_{ex,T1\to Tn} \cdot \gamma_{ph} \cdot I \approx 0.035 \cdot I$ for $T_1 \to T_n$ excitation, which depends on the absorption cross section of the triplet state T_1 $\sigma_{ex,T1\to Tn}$,

the inverse photon energy γ_{ph} and the illumination intensity I; k_{IC} the rate for radiationless **i**nternal **c**onversion (IC) from $S_n \rightarrow S_1$, or $T_n \rightarrow T_1$ and k_{revISC} the rate for reverse ISC. The transition $T_1 \rightarrow T_n \rightarrow S_n \rightarrow S_1$ is light induced and leads to an increase in singlet population and therefore an increase in fluorescence with increasing illumination intensities.

Photon-induced reverse ISC via higher excited triplet states T_n causes the deviation of the dependence of the fluorescence signal detected for imcreasing illumination intensities (figure 3.16) from the expected saturation behaviour (dashed lines). At low intensities reverse ISC does not affect the saturation behaviour, because 1. the population of the triplet state is still small, therefore not presenting many targets for reverse ISC and 2. the excitation probability from T_1 to T_n is small because of its dependence on I ($k_{ex,T1\rightarrow Tn} = \sigma_{ex,T1\rightarrow Tn} \cdot \gamma_{ph} \cdot I$). At larger intensities, the population of the triplet state saturates to a maximum possible (compare chapter 2.2), while reverse ISC leads to a depopulation of the triplet state. For a detailed simulation of the processes involved see appendix A.2.7.

Due to the low triplet relaxation rate $k_T \approx 1/s$ the relaxation of the dye molecules in the triplet state takes long. For the possible imaging protocols, regeneration of the sample to an initial state without any residual triplet population is essential and would cost long ($\approx s$) delay times. Therefore the light induced reverse ISC mechanism as a potential process to accelerate regeneration will be studied in the following section.

Light Induced Triplet Recovery via reverse ISC

As described in the previous section it is possible to deplete the triplet state T_1 with the green illumination light. The dye molecules in the triplet state are excited to higher triplet states T_n, from where reverse ISC to the singlet states S_n and relaxation to the ground state S_0 is possible. These dye molecules are again available for the fluorescence cycle, and the triplet has been depleted. In this section recovering the dye molecules from the triplet state via reverse ISC induced with light of different wavelenght will be studied, to potentially accelerate the triplet depopulation in between phase scanning.

In figure 3.17 two triplet relaxation curves recorded at the same sample at $80K$ and vacuum conditions are displayed. The black trace displays the simple pump-probe experiment of figure 3.14, with a pump pulse to populate the triplet state T_1. After a certain delay time Δt the sample is illuminated by a probe pulse of the same intensity (see schematics in figure 3.17). The peak fluorescence signal during the probe pulse is normalized to the peak signal during the pump pulse and depicted over the delay time Δt. The red trace depicts the probe fluorescence, when the sample was additionally exposed to red laser light at $655\ nm$ with a power density of $\approx 14,3\ kW/cm^2$ during the delay period Δt. It can be clearly seen that fluorescence recovery and therefore triplet relaxation is two to three times faster than in the case without additional red light ($\tau_T^{w/o\,red} \approx 750\ ms$ and $\tau_D^{with\,red} \approx 260\ ms$).

The triplet depletion - seen as fluorescence recovery - is more effective at a wavelength, that does not cause significant triplet build-up, i.e., hardly any excitation $S_0 \rightarrow S_1$. The wavelength of $655\ nm$ is chosen that is red-shifted to the excitation spectrum (see figure A.5). On the other hand the wavelength chosen for the following experiments is well above

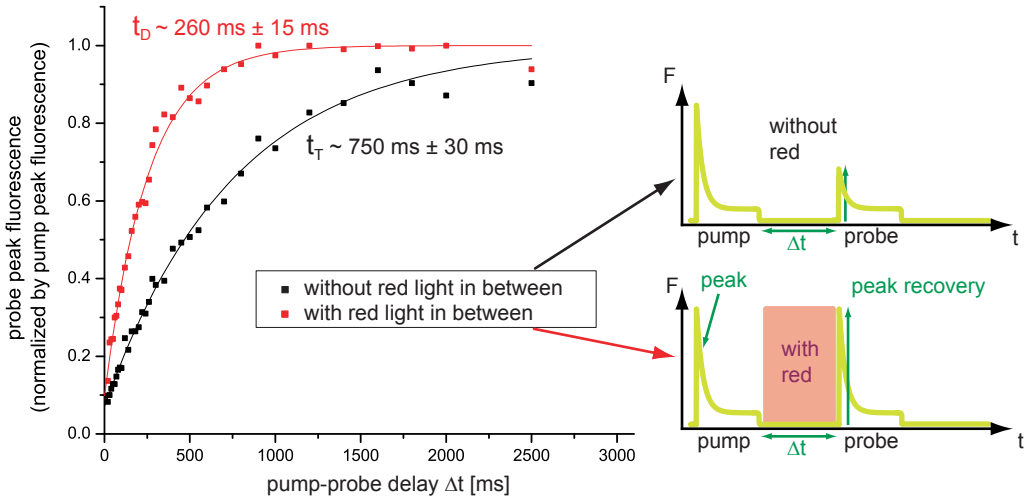

Figure 3.17: **Fluorescence recovery and triplet depopulation via induced reverse ISC.** Fluorescence recovery of beads labeled with Atto532 at $80\,K$ and vacuum conditions (<10^{-5}) at a pump-probe excitation intensity $I \approx 114,3 W/cm^2$, with (red trace) and without (black trace) exposure to a red laser (illumination intensity $I_{red} \approx 14,3 kW/cm^2$) during the delay time Δt (see schematics on the right side).

the absorption spectrum at $655\ nm$, which leaves a large detection window for fluorescence from $532\ nm$ (excitation) up to $655\ nm$ (triplet recovery).

Effect of Triplet Recovery Light on Bleaching

With the introduction of the additional red recovery laser light, the question of its influence on photobleaching arises, because the involvement of higher triplet and singlet states T_n and S_n leads to higher bleaching probabilities. Figure 3.18 shows the results of a bleaching study comparable to the one in figure 3.11. As a control, the sample is exposed 100 times to a short laser pulse of $100\,ms$ duration at a frequency of $0.1\,Hz$. Fluorescence during that so-called probe pulse is sampled and plotted over the repetitions in figure 3.18 (A). As expected bleaching is strongest at room conditions (atmospheric pressure and room temperature, pink trace). Evacuation of the sample already leads to a considerable reduction in bleaching (orange trace). Cooling further reduces bleaching slightly (compare orange, green and blue traces).

For part (B) the sample is exposed to the red laser ($655 nm$) at full power ($18.6\,kW/cm^2$) for $8\ s$ in between the probe pulses. With atmospheric conditions (atmospheric pressure and room temperature) there is no difference between the curves without and with the red laser (compare red traces in (A) and (B)), at vacuum and room temperature bleaching is slightly stronger (yellow in (A) and (B)). However the red laser reduces photobleaching in a cooled sample (green and blue traces in (A) and (B)). The red light depletes the triplet state, thus redcing the number of dye molecules in the triplet state T_1 that could be bleached via T_n by the next probe pulse. In the case of atmospheric pressure, there is less triplet build and

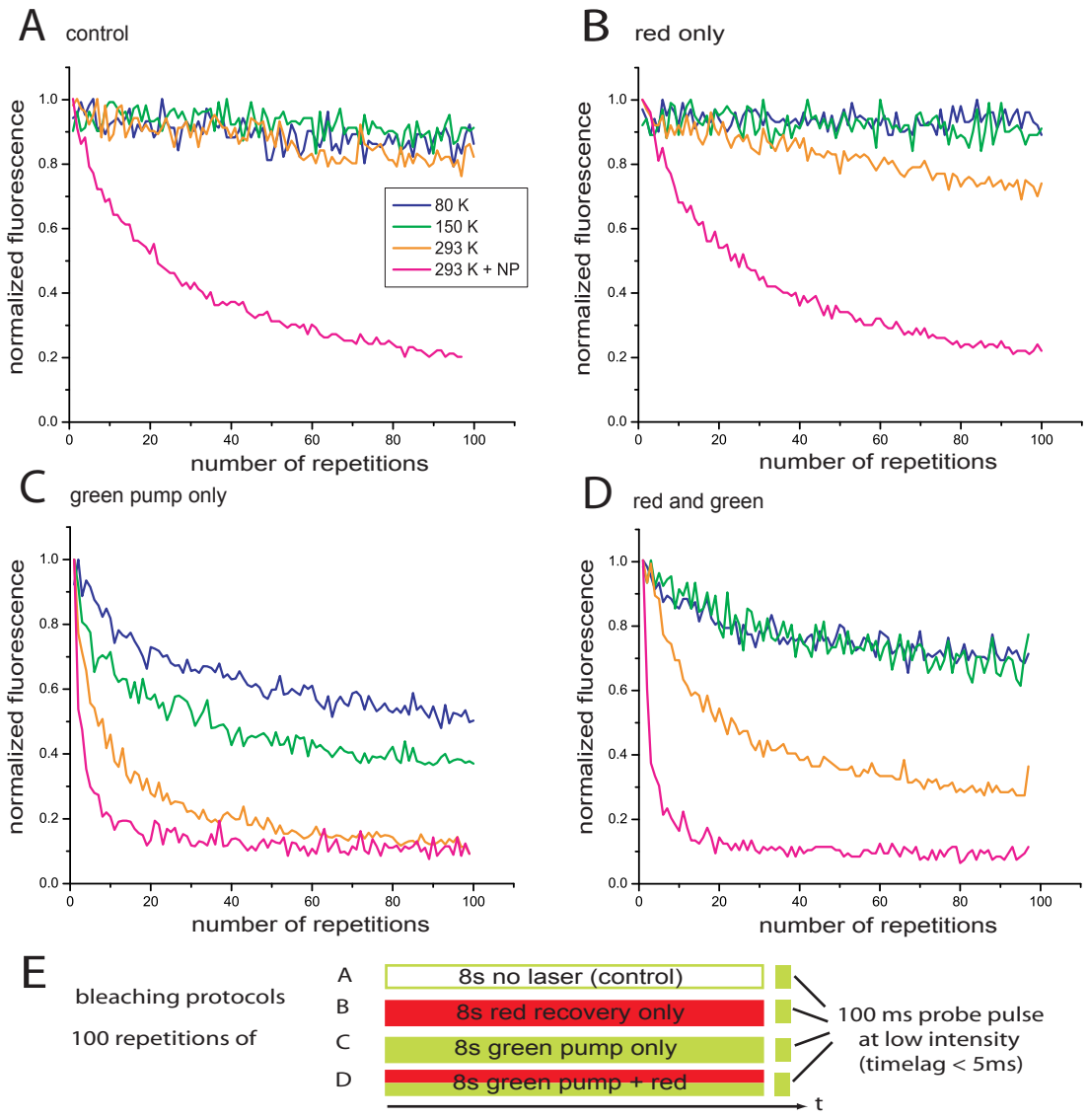

Figure 3.18: **Bleaching of beads with different light exposures and at different temperatures.** Bleaching of beads labeled with Atto532 at different temperatures and different bleaching settings
100 repetitions with a repetition frequency $0.1\ Hz$, after each $8\ s$ bleaching pulse one $100\ ms$ probe pulse: fluorescence during probe pulse averaged and normalized to first exposure, (A): no bleach laser (control for bleaching by probe laser), (B) : red laser only, (C): green pump laser only, (D): red and green pump laser simultaneously
power densities: $I_{Probe} = 136\ W/cm^2, I_{red} = 18.6\ kW/cm^2, I_{Pump} = 765\ W/cm^2$

the triplet relaxes completely within the delay time even without red laser (at atmospheric pressure and room temperature the triplet relaxation rate k_T is considerably higher than in vacuum and lower temperatures, as outlined previously). Therefore exposure to red light does not influence the bleaching behaviour at atmospheric pressure and room temperature.

In figure 3.18 (C) the green laser (pump pulse) is switched on for $8\ s$ at high power

($785\ W/cm^2$) in between probe pulses. Bleaching is considerably stronger than in case (A) at all temperatures and conditions, because the triplet is constantly populated and aids bleaching. It is reduced though by lowering the temperature.

For part (D) the sample is simultaneously exposed to the green pump pulse ($785 W/cm^2$) and the red depletion pulse ($18.6\ kW/cm^2$) for $8\ s$ in between the probe pulses. At room conditions (pink trace) bleaching is merely altered in comparison to the other settings, if at all it is slightly stronger. For the evacuated samples bleaching is reduced substantially compared to figure 3.18 (C) (orange, green and blue traces), which is due to depletion of the triplet by the red light.

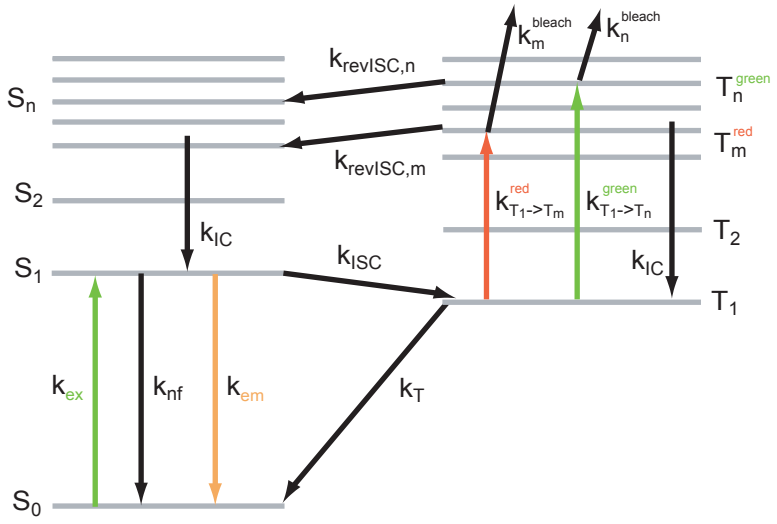

Figure 3.19: **Jablonski diagram** including excitation from T_1 to T_n by green excitation light oder red triplet recovery light, reverse inter-system-crossing with a rate k_{revISC} and bleaching with a rate k_n.

To illuminate the processes involved, figure 3.19 shows a Jablonski diagram with exciation from $T_1 \rightarrow T_n, T_m$ by absorption of a green or red photon respectively, bleaching and reverse ISC from T_n, T_m and internal conversion $T_n, T_m \rightarrow T_1$ and $S_n \rightarrow S_1, S_0$. The excitation rates ($k^{red}_{T1->Tm}$ and $k^{red}_{T1->Tm}$) depend on the absorption cross section for the particular transition at the wavelength in question ($\lambda_{\text{green}} = 532\ nm$, $\lambda_{\text{red}} = 655\ nm$) and the illumination intensity of the red or green laser respectively. The final state T_n^{green} after absorption of a green photon is energetically higher than the final state T_m^{red} after absorption of a red photon: $E(T_n^{green}) > E(T_m^{red})$, which is due to the energy of the absorbed photon. Bleaching is more probable from energetically higher excited electronic states. Therefore the bleaching rate from T_n^{green} is higher than from T_m^{red} , which can be described by bleaching rates $k_n^{bleach} > k_m^{bleach}$.

The sample can be bleached by the red laser alone, which can be seen when comparing the orange traces of part (A) and (B) , but this effect is slightly reduced when the sample is cooled (green and blue traces), which is to due smaller bleaching rates k_m^{bleach} – reactivity

– at lower temperatures. When the sample is evacuated, exposure to green or red light in between probe pulses leads to bleaching. At vacuum and even more so at low temperatures, the triplet lifetime is larger, resulting in a larger steady-state population of the triplet state and therfore more bleaching.

When comparing the orange, green and blue traces of parts (C) and (D) it is very clear, that the combined exposure to red and green light reduces the bleaching effect of the green pump laser. This is due to triplet depletion by the red light over higher excited triplet states. Actually the probability and therefore the rate for reverse ISC is larger fir higher levels n of T_n ($k_{revISC,n} > k_{revISC,m}$), because of the higher density of states. However the rate for reverse ISC with red light k^{red}_{revISC} seems to be larger than the bleaching rate with the green pump laser $k^{green}_{n,bleach}$, thus resulting in a diminished bleaching at combined exposure to red and green light.

Red light in competition to green light at given powers leads to reduced bleaching, but does not directly render an increase in fluorescence. This can only be achieved by a better and thus faster depletion of the triplet state, by more pronounced $T_1 \rightarrow T^{red}_m$ excitation. The excitation rate $k^{red}_{T1->Tm}$ depends on the absorption cross section and the illumination intensity of the red light. Due to limited power output of the applied laser, higher illumination intensities are not available at the moment, especially for a widefield setup where the illuminated area is larger than in a confocal setup.

In conclusion the triplet state can be depleted by red light, which does not provide enough energy for excitation and therfore does not populate the triplet state. The triplet relaxation rate k_T is thus increased by a factor of ≈ 3 to $\approx 260\,ms$. Introduction of a second laser line in combination with the green pump laser reduces bleaching thus adding a useful sideeffect.

Pump-Probe Fluorescence Saturation

To be able to use GSD as a RESOLFT-method for high resolution imaging a saturable transition between a bright and a dark state is essential. As described previously, the steady-state fluorescence with population of the triplet state does not saturate, because of depopulation of said triplet state via reverse ISC (see figure 3.16). Therefore a *pump-probe* approach is taken, where a *pump pulse* of $50ms$ is directly followed by a second exposure to the so-called *probe pulse* of constant intensity. Figure 3.20 displays the peak fluorescence signal sampled during the first $3\,ms$ of the probe pulse (constant probe intensity I_{probe}) with different illumination intensities of the pump pulse I_{pump}. The fluorescence signal is normalized to the fluorescence during the probe pulse without previous exposure to the pump pulse ($I_{pump} = 0$). At low pump intensities the fluorescence signal is large, but decreases rapidly with increasing pump intensities towards a constant saturation level F_{sat}, which is the same for all temperatures at vacuum conditions.

During the exposure to the pump pulse the dye molecules are driven to the steady-state populations of the ground state S^{SS}_0, the first excited singlet S^{SS}_1 and the first excited triplet state T^{SS}_1 described in the appendix A.2.4:

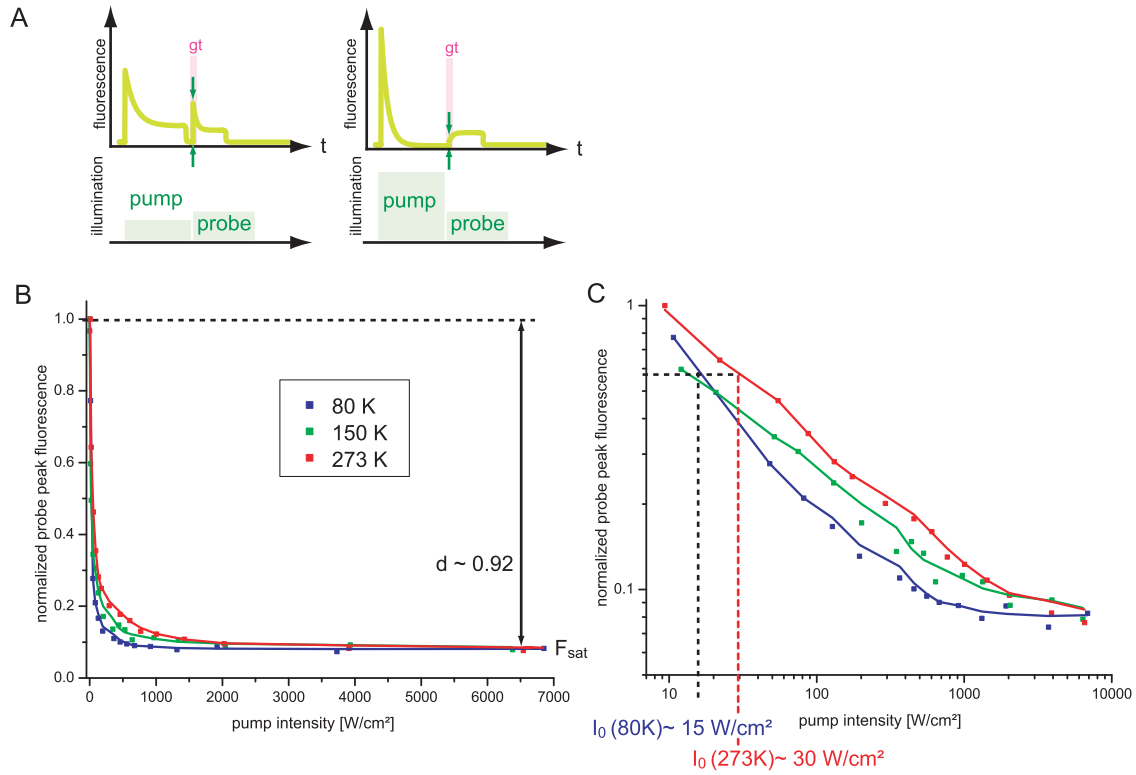

Figure 3.20: **Fluorescence depletion by GSD of Beads at different temperatures** (A): schematic fluorescence signal due to pump-probe exposure (B) & (C): peak fluorescence signal during probe pulse with linear and logarithmic scaling (respectively); F_{sat} is the saturation fluorescence, I_0 is the saturation intensity and $d := F_{sat}/F_{max}$ the depletion efficiency ; parmeters: silica beads labeled with Atto532, vacuum conditions (<10^{-5}), pump pulse 50 ms, probe pulse 50 ms, pump-probe delay $\Delta t < 2\ ms$, recovery pulse (red laser) 800 ms, integration sampled during 3 ms over 50 repetitions with a rate of 1 Hz

$$
\begin{aligned}
S_0^{SS} &= \frac{(k_{10} + k_{ISC}) \cdot k_T}{(k_{10} + k_{ISC}) \cdot k_T + k_{ex,pump} \cdot (k_T + k_{ISC})} \\
S_1^{SS} &= \frac{k_{ex,pump} \cdot k_T}{(k_{10} + k_{ISC}) \cdot k_T + k_{ex,pump} \cdot (k_T + k_{ISC})} \\
T_1^{SS} &= \frac{k_{ISC} \cdot k_{ex,pump}}{(k_{10} + k_{ISC}) \cdot k_T + k_{ex,pump} \cdot (k_T + k_{ISC})}
\end{aligned}
\tag{3.20}
$$

with the singlet deexcitation rate k_{10}, ISC rate k_{ISC}, triplet relaxation rate k_T and the excitation rate $k_{ex,pump} = \sigma_{ex} \cdot \gamma_{ph} \cdot I_{pump}$ (σ_{ex} and γ_{ph} are the cross section for fluorescence excitation and the inverse photon energy, respectively). After the pump pulse the molecules in the first excited singlet state S_1 decay rapidly to the ground state S_0 within ns ($k_{10} \approx 10^9\ \frac{1}{s}$), whereas the molecules in the triplet state T_1 hardly relax to the ground state ($k_T \approx \frac{1}{s} \prec k_{10}$)

within the time window $\Delta t < 2\ ms$ to the probe pulse, leading to the following populations at the beginning of the probe pulse:

$$\begin{aligned} S_0^{\text{after pump}} &= \frac{(k_{10} + k_{ISC} + k_{ex}) \cdot k_T}{(k_{10} + k_{ISC}) \cdot k_T + \sigma_{ex} \cdot \gamma_{ph} \cdot I_{pump} \cdot (k_T + k_{ISC})} \\ S_1^{\text{after pump}} &= 0 \\ T_1^{\text{after pump}} &= T_1^{SS} = 1 - S_0^{SS} \\ &= \frac{k_{ISC} \cdot \sigma_{ex} \cdot \gamma_{ph} \cdot I_{pump}}{(k_{10} + k_{ISC}) \cdot k_T + \sigma_{ex} \cdot \gamma_{ph} \cdot I_{pump} \cdot (k_T + k_{ISC})} \end{aligned} \tag{3.21}$$

The peak fluorescence F resulting from illumination with the probe pulse (I_{probe}) can only stem from the molecules in the singlet system:

$$\begin{aligned} F &\propto k_{ex,probe} \cdot S_0^{\text{after pump}} \\ &\propto I_{probe} \cdot S_0^{\text{after pump}} \end{aligned} \tag{3.22}$$

The linear relationship between singlet population and the peak fluorescence during the probe pulse is only true as long as the probe intensity I_{probe} is well below the saturation intensity for the transition from $S_0 \rightarrow S_1$, which is the case in moste experiments. Only the peak fluorescence of the probe pulse can be taken, as the probe pulse itself influences the population of the three states to a new steady-state population.

Figure 3.20 shows the dependence of the peak fluorescence $F(I_{pump})$ during the probe pulse (with constant intensity I_{probe}) in dependence of the intensity of the pump pulse: I_{pump}. Low I_{pump} elicits negligible triplet build-up, leaving a high singlet population, which results in high probe peak fluorescence. By increasing I_{pump} the population of the triplet state increases, leading to less molecules left in the singlet and a reduced fluorescence signal.

The fluorescence saturation level F_{sat} is determined by the relative population of the singlet and triplet states after the pump pulse:

$$\begin{aligned} F_{sat} &= \lim_{I_{pump} \to \infty} F(I_{pump}) \\ &\propto \lim_{I_{pump} \to \infty} \left(1 - T_1^{SS}\right) \\ &\propto \lim_{I_{pump} \to \infty} \left(1 - \frac{k_{ISC} \cdot \sigma_{ex} \cdot \gamma_{ph} \cdot I_{pump}}{(k_{10} + k_{ISC}) \cdot k_T + \sigma_{ex} \cdot \gamma_{ph} \cdot I_{pump} \cdot (k_T + k_{ISC})}\right) \\ &\propto \left(1 - \frac{k_{ISC}}{k_{ISC} + k_T}\right) = \frac{k_T}{k_{ISC} + k_T} \end{aligned} \tag{3.23}$$

As $k_{ISC} \approx 10^6\ \frac{1}{s} \succ k_T \approx 1\ \frac{1}{s}$, the fluorescence saturation is expected to be $F_{sat} \approx 5 \cdot 10^{-7} \cdot F_{max}(I_{pump} = 0)$ (using the rate constants $k_{ISC} = 3 \cdot 10^6\ \frac{1}{s}$ (see appendix A.2.7 for detailed references for rate constants) and $k_T = 1.4\ \frac{1}{s}$ determined previously). However,

the depletion level in figure 3.20 (A) i.e. the *depletion of fluorescence* is incomplete down to only $d \approx 92\%$, leading to a saturation fluorescence $F_{sat} = (1-d) \cdot F_{max} \approx 8\%\ F_{max}$. If the light driven reverse ISC were responsible for this incomplete depletion, the saturation fluorescence level would be:

$$\begin{aligned} F_{sat} &= \lim_{I_{pump}\to\infty} F(I_{pump}) \\ &\propto \lim_{I_{pump}\to\infty} \left(1 - T_1^{SS}\right) \\ &\propto \left(1 - \frac{k_{ISC}}{k_{ISC} + k_T}\right) = \frac{k_T + k_{T1->Tn} \cdot \Phi_{revISC}}{k_{ISC} + k_T + k_{T1->Tn} \cdot \Phi_{revISC}} \end{aligned} \tag{3.24}$$

which leads to $F_{sat}/F(I_{pump} = 0) \approx 1 \cdot 10^{-5}$ (with $k_{T1->Tn}(I_{pump} = 1000\ W/cm^2) \cdot \Phi_{revISC} \approx 35$ determined in appendix A.2.7), which is still much lower than $d \approx 8\%$ determined from figure 3.20. Reverse ISC depends on the illumination intensity I_{pump}, therefore an increase of F_{sat} with I_{pump} is expected, but since this relationship is very weak ($k_{ex} \approx 1030\, cm^2/J \cdot I$ in comparison to $k_{T1->Tn} \cdot \Phi_{revISC} = 0.035\, cm^2/J \cdot I$ see appendix A.2.7) it was not observed at the intensities used in the experiment. The incomplete depletion is therefore mainly due to the chosen fluorescence integration time (so-called *gate time* gt) for peak fluorescence sampling and will be discussed in detail below.

The saturation intensity I_0 (of the pump pulse) at which half of the fluorescence is depleted can be read from figure 3.20 (B) as $I_0(80\ K) \approx 15\ W/cm^2$ and $I_0(273\ K) \approx 30\ W/cm^2$. I_0 can be calculated from the rate equations 3.20 as:

$$\begin{aligned} I_0 &= \frac{k_T}{k_T + k_{ISC}} \cdot \frac{k_{10} + k_{ISC}}{\sigma_{ex} \cdot \gamma_{ph}} \\ &\text{leading to :} \\ F(I_{pump}) &\propto \frac{k_T}{k_T + k_{ISC}} \cdot \frac{1}{1 + \frac{I_0}{I_{pump}}} \end{aligned} \tag{3.25}$$

The triplet relaxation rate is lower at lower temperatures (see figure 3.14, $\tau_T(80\ K) \approx 716\, ms$, $\tau_T(300\ K) \approx 320\, ms \leftrightarrow 1/k_T(80\ K) \approx 2 \cdot 1/k_T(300\ K)$). The saturation intensity is proportional to the triplet relaxation rate $I_0 \propto k_T \cdot \frac{k_{ISC}+k_{10}}{k_{ISC}}$ (with the approximation $k_t << k_{ISC}$), and thus I_0 decreases with temperature ($I_0(273\ K) \approx 2 \cdot I_0(80\ K)$).

The pump-probe approach clearly shows a saturated relationship between the pump intensity I_{pump} and the peak fluorescence during the probe pulse. The low saturation intensity allows very large saturation factors $\xi_{sat} = I_{pump}/I_0$, which is necessary for high-resolution imaging.

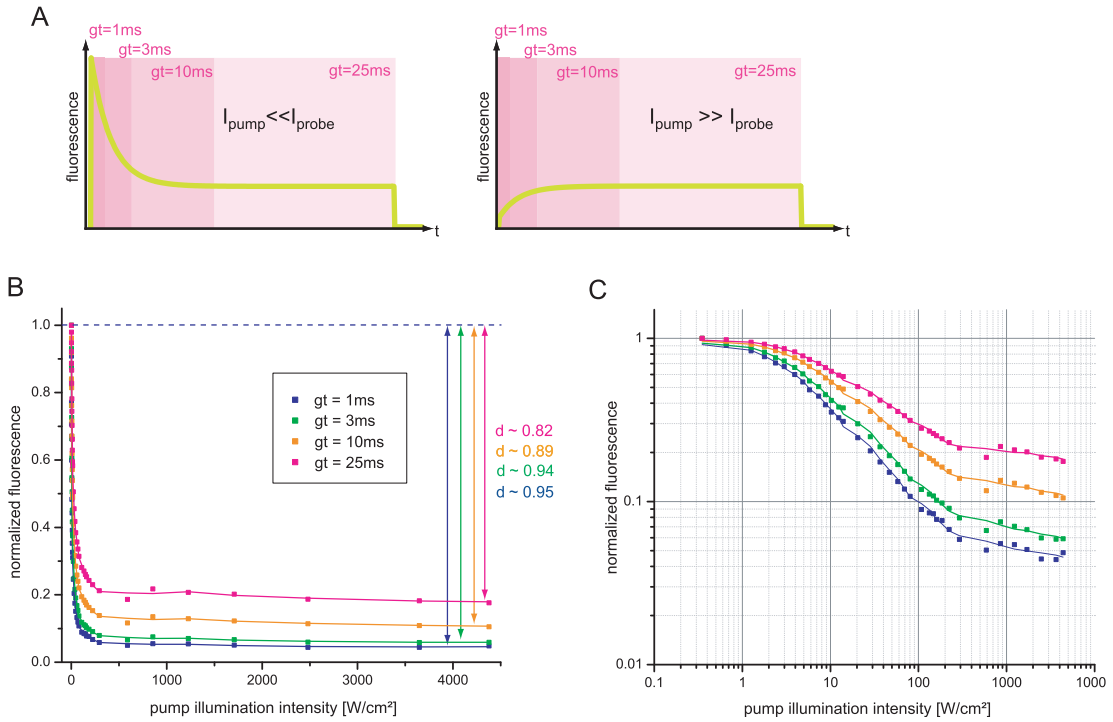

Figure 3.21: **Influence of different fluorescence integration times on the level of fluorescence depletion by GSD** of Atto532-Beads at $80\,K$ and vacuum conditions (<10^{-5}), different integration windows of fluorescence sampling during the probe pulse (blue: $gt = 1\,ms$, green $gt = 3\,ms$, yellow $gt = 10\,ms$, red $gt = 25\,ms$). Saturation level F_{sat} (blue: 0.05, green: 0.06, yellow: 0.11, red: 0.18) and decreases as the gate time (fluorescence integration time) is increased. Saturation intensity I_0 (blue: $5\,W/cm^2$, green: $6\,W/cm^2$, yellow: $10\,W/cm^2$, red: $13\,W/cm^2$) increases as well with gate time. $I_{Probe} = 94.9\,W/cm^2$, lines are eyeguides

Incomplete Fluorescence Depletion

In the previous chapter it has been shown, that the depletion efficiency expected from photophysical theory is much lower than the measured one. A possible reason was assumed to be the lenght of the gate time (fluorescence integration time) gt of fluorescence signal detection during the probe pulse. Figure 3.21 shows the measured initial fluorescence sampled for four different imtegration times ($gt = 1\,ms$ (blue), $gt = 3\,ms$ (green), $gt = 10\,ms$ (orange) and $gt = 25\,ms$ (pink), dwell time $1\,ms$) of the probe pulse in dependence of the pump intensity I_{pump}. As in the previous figure 3.20 the fluorescence depletion is clearly saturated, but at different residual levels of F_{sat} or depletion efficiencies $d = (F_{max} - F_{sat})/F_{max}$ given in percent. The depletion efficiency d decreases with increasing integration times gt for peak fluorescence sampling, which is due to the influence of the probe pulse on the population of the singlet and triplet system. Not only the pump pulse, but also the probe pulse influences the population of the singlet and triplet states, leading to new steady state populations depending on the probe intensity I_{probe}. Only the initial fluorescence during the probe pulse is proportional to the population of the singlet after the pump pulse, described by equation 3.25.

If the intensity of the pump pulse is much lower than the intensity of the probe pulse $I_{pump} << I_{probe}$, the steady-state population after the pump pulse is higher than the steady-state population due to the probe intensity. This leads to a decrease from the initial intensity ($\propto S_0^{\text{after pump}}$) to the equilibrium fluorescence due to I_{probe} and appears as a peak in the fluorescence trace (see left part of (A) of figure 3.21). If $I_{pump} >> I_{probe}$ the steady-state after the pump pulse is much lower than the steady-state due to the probe pulse. This leads to an increase in fluorescence with illumination by the probe pulse (see right part of (A) of figure 3.21).

By sampling the fluorescence for a certain integration time gt, not only the initial fluorescence signal will be detected, but also contributions from the changing fluorescence as well. In the case of $I_{pump} << I_{probe}$, the additionally integrated signal will be smaller, than the initial signal, leading to an underestimation of the fluorescence response. In the case of $I_{pump} >> I_{probe}$, the additionally integrated signal is larger than the initial signal. Thus the integrated fluorescence signal is over-estimated. Altogether, the influence of the fluorescence integration time gt on the depletion efficiency is twofold: firstly the maximum fluorescence $F_{max}(I_{probe} = 0)$ is estimated too low, and secondly the fluorescence saturation level F_{max} is estimated too large. In total, this leads to lower levels of depletion efficiency as theoretically expected. The apparent depletion efficiency increases with choosing a smaller fluorescence integration time windows gt. On the other hand, gt needs to be of a certain size, to be able to detect the fluorescence signal over the present noise. Therefore a certain level of *incomplete depletion* cannot be avoided.

The incomplete saturation of fluorescence can be described by adding the depletion efficiency d to equation 3.25:

$$\begin{aligned} F(I_{pump}) &\propto \frac{k_T}{k_T + k_{ISC}} \cdot \frac{d}{1 + \frac{I_0}{I_{pump}}} \\ &\text{with :} \\ I_0 &= \frac{k_T}{k_T + k_{ISC}} \cdot \frac{k_{10} + k_{ISC}}{\sigma_{ex} \cdot \gamma_{ph}} \end{aligned} \tag{3.26}$$

The actual saturation intensity I_0 is hardly influenced by the choice of a fluorescence integration time windwows gt, since it is merely determined by the photophysical properties. The value of I_0 determined from fluorescence saturation curves such as figure 3.20 and 3.21 varies slightly with the fluorescence integration time windwows gt as it is an unavoidable measurement artifact.

The choice of the probe intensity I_{probe} has a similar effect on the depletion efficiency as the choice of detection timeframe as the length of the gate time gt (3.22). With larger I_{probe} the population of the triplet occurs faster and the peak fluorescence decays faster. Thus a small gate time is chosen to detect the initial fluorescence, but not too much of the residual fluorescence level.

The saturation of fluorescence depletion by pump-probe sequences yields a very low

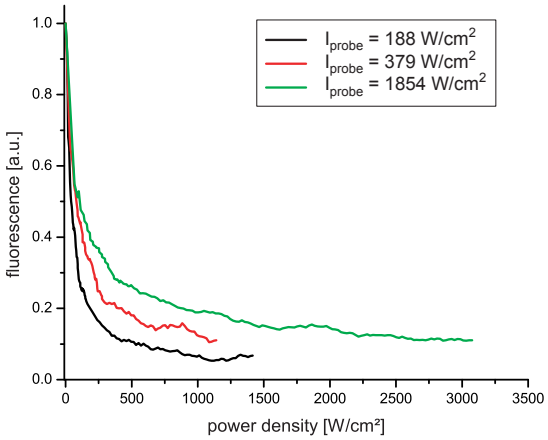

Figure 3.22: **GSD for Atto532 in glycerol** on cover slip @$80\,K$, vacuum conditions (<10^{-5}). Different probe powers show slightly different saturation curves, as the triplet build up is faster in the case of higher laser power.

saturation intensity of $I_0 \approx 15\,W/cm^2$ and thus very high saturation possible factors $\xi_{sat} = I_{pump}/I_0$, with a low value of $I_{probe} << I_{pump}$. Probing the singlet population leads to fluroescence depletion as the saturable process and allows the implementation of positive signal stripes for RESOLFT. Positive stripes were discussed to be the favorable option for imaging with saturated structured illumination (chapter 3.1).

4 Parallelized Ground State Depletion

This chapter describes the experimental realization of parallelized ground state depletion. Saturable depletion of fluorescence is utilized by populating the dye´s triplet state, thus depleting the singlet ground state with green excitation light and probing the residual singlet population (the residual fluorescence) with a second pulse of green excitation light (see section 3.3). Besides spontaneous relaxation, the original population of the ground state only is reset by the use of red depletion light. Parallelization is achieved by structuring the depleting pump light by interference of two beams in the optical plane (see section 3.1.2). Probe light and red recovery light are homogeneous (not modulated). Fluorescence is detected in a spatially resolved manner by a camera.

4.1 Experimental Setup

Taking an image with parallelized ground state depletion requires three consecutive exposures of the sample, repeated at a frequency of $1\ Hz$ (see figure 4.1). First the sample is exposed to a pump pulse (depleting the singlet population) of $50\ ms$ duration, directly ($< 2\ ms$) followed by a probe pulse of $50\ ms$ duration. To reset the ground state population, the sample is exposed for $\approx 800\ ms$ to red light. The pulses were temporally aligned by a function generator (9514 digital delay and function generator, Scientific Instrumens, Gilching, Germany). Temporal alignment was optimized with the use of a photodiode in the intermediate focal plane and an oscilloscope.

Figure 4.1: **Pulse sequence used for imaging**

The depletion light (pump pulse), which applies the RESOLFT principle, i.e. which causes the subdiffraction confinement of fluorescence, is modulated in space. The probe

pulse has a homogeneous beam profile ensuring the same probe power at every point of the illuminated sample (see influence of probing power on saturation behaviour in figure 3.22). The same is true for the red recovery beam, to ensure an equal reset all over the sample. Fluorescence was detected during the first $3 - 5\ ms$ of the probe pulse.

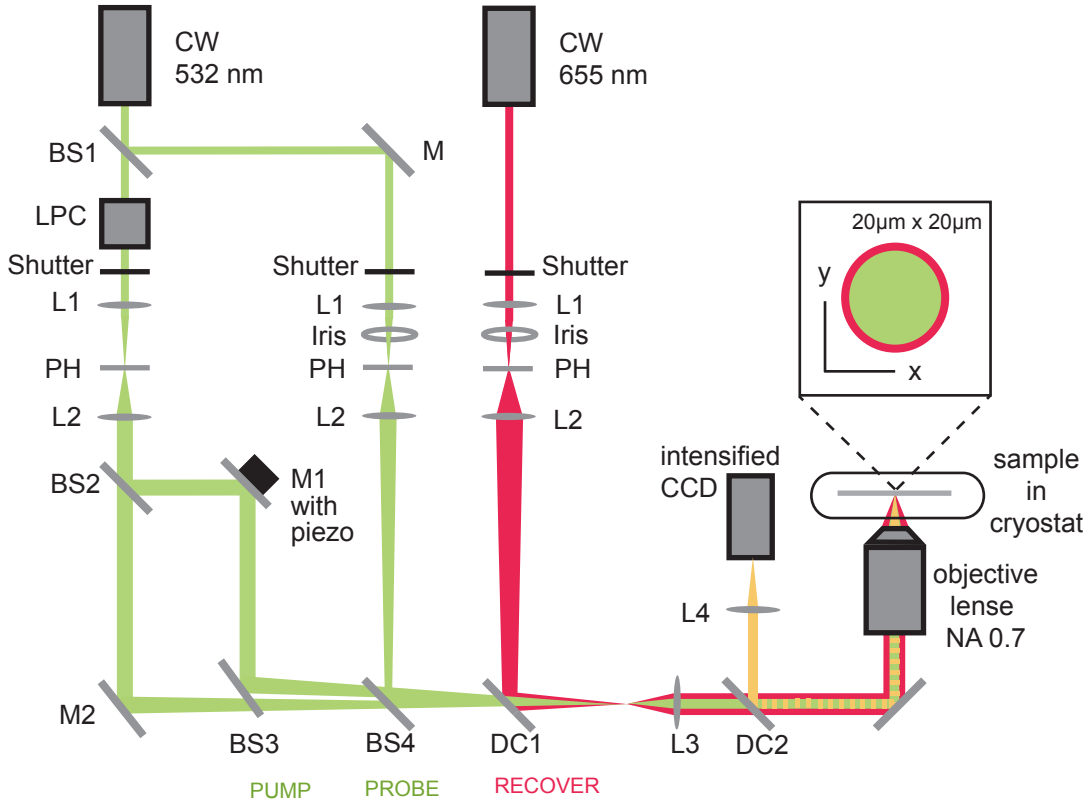

Figure 4.2: **Experimental Setup**

The experiment was implemented as depicted in figure 4.2 with a continuous wave (cw) laser of $532\ nm$ (Verdi V5, Nd:YAG 1064nm, SHG 532nm, Coherent GmbH, Dieburg, Germany). Using a beam splitter (BS1, 80:20) the laser light was divided into pump and probe beams respectively. Duration and power of the pump pulse were controlled by a laser power controller (LPC; Brockton Electro-Optics, Brockton, MA, USA) and a fast shutter (Shutter; Uniblitz, BFI Optilas GmbH, Puchheim, Germany). Duration and power of the probe pulse was controlled by another shutter (Shutter; Uniblitz, BFI Optilas GmbH, Puchheim, Germany) and the use of an iris diaphragm (iris) in combination with a pinhole (PH). Both beams were focused by lenses (L1) onto pinholes (PH) and subsequently recombined by a beam splitter (BS 4, 50:50). The source for the depletion light was a continous wave (cw)

laser of $655\,nm$ (Alphalas, Göttingen, Germany), for which illumination time and power was controlled with a third shutter (Shutter; Uniblitz, BFI Optilas GmbH, Puchheim, Germany) and by another set of iris diaphragm (iris) in combination with a pinhole (PH), respectively. The red light was combined with the green light via a dichroic mirror. For all three beamlines the pinhole was imaged using a single lens (L2) into the intermediate focal plane, where their alignment could be tested using a CCD chip (webcam, Phillips, Hamburg, Germany).

The three overlaid spots from the intermediate focal plane were mapped by another lens (L3) and the objective lense (0.7 NA, 63x air, LEICA Microsystems GmbH, Bensheim, Germany) into the focal plane of an inverse epi-illuminated microscope (DM-IRBE, LEICA Microsystems GmbH, Bensheim, Germany). Fluorescence emitted by the sample was collected through the same objective lense and focused (L4) onto an intensified CCD camera (intensified CCD; PI-MAX2: 1003 UNIGEN, Roper Scientific GmbH, Ottobrunn, Germany) and processed with a framegrabber card and a PC. For recording the fluorescence signal over time the CCD camera was replaced with an avalanche photo diode (APD; Perkin & Elmer, Laser Components GmbH, Olching, Germany) in combination with a multichannel data collector (P7782, Fast ComTec, Oberhaching, Germany).

The interference pattern of the pump beam was generated by an interferometer consisting of two 50:50 beam splitter (BS2 and BS3) and two mirrors (M1 and M2) as already shown in figure 3.9. The resulting intensity profile $\approx\ sin^2\left[2\pi\ n/\lambda\ x\ sin(\alpha/2)\right]$ along the x-direction of the objective focal plane was given by interference of the two beams in the sample with $\lambda = 532\,nm$ denoting the laser wavelength, n the index of refraction at the sample, and α the angle under which the two partial pump beams interfere in the sample plane. The polarization of the green pump beam was perpendicular to the plane spanned by the interfering partial beams. The polarization of the green probe laser was chosen to be the same to avoid polarization effects. By varying α, the distance $D = \lambda/(2n\ sin(\alpha/2))$ between two neighbouring interference stripes could be controlled. Additionally, a piezo actuator (Piezo; P-841, PI, Karlsruhe, Germany) in one of the interferometric arms allowed one to scan the phase of the green pump pattern, i.e. to scan the illumination pattern across the sample.

For evacuation and cooling, the sample was put into a microscopy cryostat (ST-500-LN, Janis Research Corporation Inc., Wilmington, USA) which was mounted on top the microsope, so that the sample was in the focal plane of the microsope. The sample was evacuated by a two stage pump (TSH 071/DUO TurboCube, Pfeiffer Vacuum GmbH, Asslar, Germany). For cooling, liquid nitrogen was piped from a dewar vessel (Apollo, Messner, Griesheim, Germany) into the cryostat. The cryostat was equipped with a heating system, whereby sample temperatures between $80\ K$ and $373\ K$ could easily be achieved.

4.2 Image reconstruction

Images taken with structured illumination at one pattern position can be seen directly on the CCD camera. To extract the high resolution information from these single frames and build one high-resolution image, a reconstruction process is necessary. Image reconstruction from the series of frames with different pattern positions can either be done in real or in

Fourier space. The use of real space is very straightforward and comparable with image reconstruction in confocal imaging and was used in this thesis.

The illumination pattern used for image recording was structured along one dimension, **x**, only: $I(\mathbf{x})\sin^2(\pi\ \mathbf{x}/D)$ (with D the distance between maxima). Along the second dimension, **y**, the illumination was homogeneous. Thus the direction of y did not give any resolution enhancement or require special attention during reconstruction. In principle structured illumination can be extended to the second dimension **y** by successive or simultaneous exposure to a second pattern $I(\mathbf{y})\sin^2(\pi\ \mathbf{y}/D)$. The following description of the reconstruction protocol deals with structuring along the direction of **x** only.

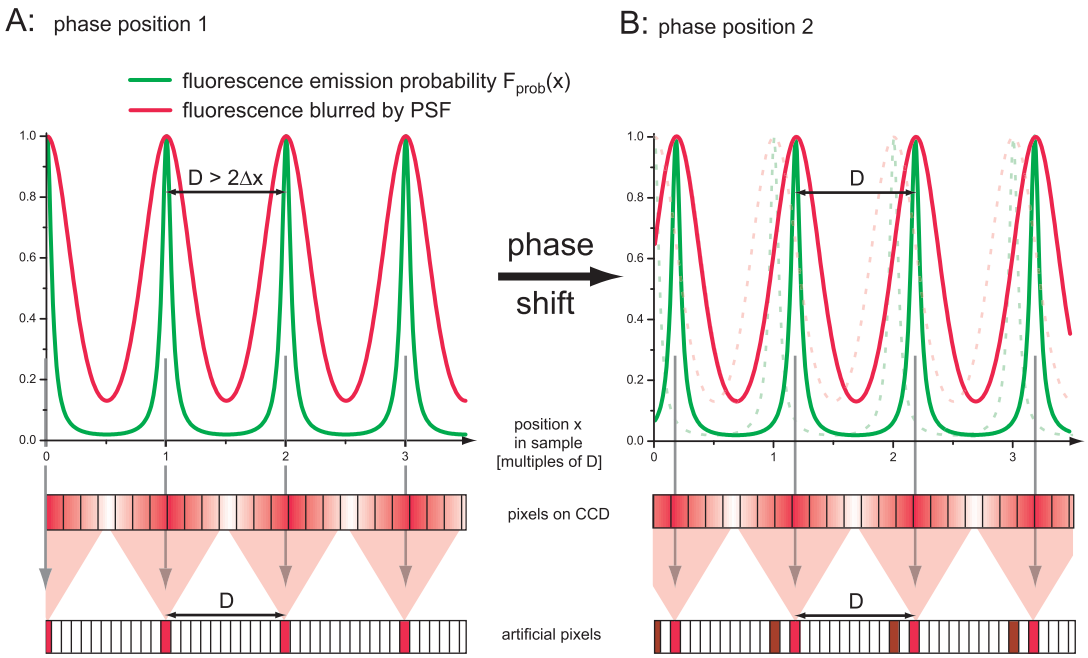

Figure 4.3: **Image reconstruction process** Image reconstruction procedure by addition and resampling fluorescence according to the areas of possible fluroescence emission with the help of artificial confinement pixels; no complex procedures such as deconvolution were used. (A): first phase position (B): another phase position, dashed lines indicate phase position of part (A)

As was described previously in chapter 3.1.1 and figures 3.1 and 3.2, due to saturated fluorescence depletion via saturation of the triplet population the fluorescence emission probability $F_{prob}(x)$ is restricted to spatially small regions at the minima of the depletion pattern of the pump pulse (see green trace in figure 4.3 (A)) . Fluorescence emitted by dye molecules

in these areas is blurred by the objective and tubular lens when it is detected on the CCD camera pixels (red trace in figure 4.3). Since fluorescence can only be emitted from the maxima of $F_{prob}(x)$, the fluorescence signal can be reassigned to these regions. Therefore, the fluorescence counts from CCD pixels in between the minima of the depletion light are added to create a new artificial confinement pixel of the high-resolution image. This is done at every minimum, i.e. every maximum of the fluorescence emission probability F_{prob} as is shown in the lower part of figure 4.3 (A), leading to a series of artificial pixels in the distance D of the depletion pattern . To be able to clearly reassign the fluorescence to the maximum of F_{prob} where it was emitted, the distance has to be $D \geq 2 \cdot \Delta x$, with the diffraction limit Δx (from equation 2.1). If D is smaller than that, there will be crosstalk due to reassignment of fluorescence to the wrong maximum of F_{prob}.

The reassignment process is repeated for every phase shifted image that has been taken during the experiment (see figure 4.3 B), assuming an equidistant scanning of one period in m phase steps. The resulting artificial pixels have to be rearranged alternately according to their original maxmimum position to create the final image. It is only necessary to scan every point in space once, that is, until one maximum of the fluorescence emission probability $F_{prob}(x)$ has reached the position of the previous maximum in the very first frame.

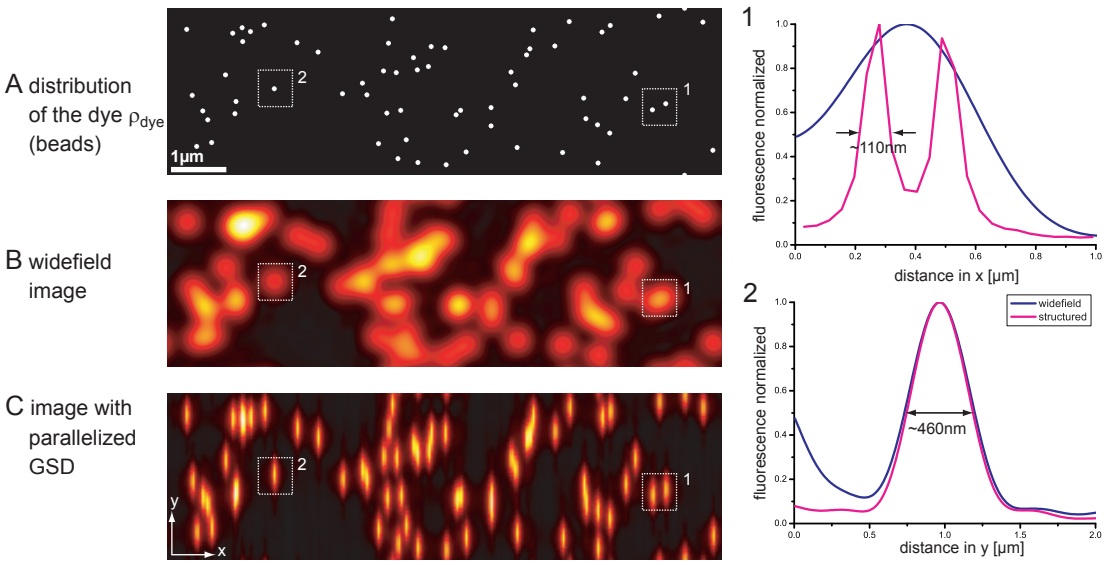

Figure 4.4: **Reconstruction process exemplified on a simulated image of beads of** $45\ nm$ (A): original dye distribution ρ_{dye}: 20 beads with a diameter of $45\ nm$ (B): widefield image of the beads with a detection PFS with a FWHM $\approx$ $440\ nm$ (C): reconstructed image from structured illumination (distance of maxima $D = 1.25\ \mu m$, saturation factor $\xi_{sat} = I_{max}/I_0 = 100$); 1: and 2: profiles in the direction of x and y of the regions marked as a white box, respectively; total image size $10\ \mu m \times 3\ \mu m$

When the distance D between two maxima is scanned in m equidistant phase steps and the number of fluorescence emission probability maxima used is l, the resulting number of pixel in the final image in the direction of x will become $m \cdot l$ and the image size X along that direction $X = D \cdot l + D \cdot (m-1)/m$. The size s of the artificial pixels is determined

by $s = D/m$.

Figure 4.4 outlines the image reconstruction on a simulated image of randomly distributed fluorescent beads of $45\,nm$. The simulated sample (A) assumed a series of 20 point emitters with a diameter of $45\,nm$ randomly placed in an area of $10\,\mu m \times 3\,\mu m$. The widefield image (B) was calculated by convolution of the dye distribution $\rho_{dye}(x)$ with a theoretical detection PSF $h(\mathbf{x})$ with a full width at half maximum FWHM $\approx 440\,nm$. The third image (C) shows the GSD image of the beads. Therefore a saturated sine squared pattern of fluorescence emission probability (distance of maxima $D = 1.25\,\mu m$, saturation factor $\xi_{sat} = I_{max}/I_0 = 100$) was assumed, scanned over the beads in $m = 30$ different phase positions, convolved with the detection PSF $h(\mathbf{x})$ and reconstructed as outlined.

The images simulated with structured illumination show much higher resolution in the direction of x than the standard widefield image. Single beads, that are blurred to one bright spot in the widefield image (for example at position 1), can be distinguished in the structured illumination image. This is illustrated by the fluorescence profiles shown in figure 4.4 (1), where two beads are clearly separated and the FWHM is measured as $\approx 110\,nm$. Along the non-structured direction of y though, the FWHM, and therefore the resolution, is not changed by structured illumination, which is illustrated with the y-profiles of a single bead in graph 2.

For this direct reconstruction approach it is essential, that the phase is scanned in m equidistant steps Δs over exactly one period $D = m \cdot \Delta s$. If $D \neq m \cdot \Delta s$ image reconstruction will result in artifacts such as sharp edges or ghost images, which will be exemplified later.

The second possible image resonstruction approach is by the use of Fourier space (representing images by image frequencies $\mathbf{k}$) and the system of linear equations 3.17 derived in chapter 3.1.1:

$$\hat{B}(\mathbf{k}, \varphi_j) = \sum_{n=-N}^{N} |c_n| \cdot e^{-\mathrm{i}\varphi_j} \cdot \hat{\rho}_n(\mathbf{k}) \cdot \hat{h}(\mathbf{k}) \quad \text{with } n \leq N \in Z, j = 0, \cdots + m$$

Here, $\hat{B}(\mathbf{k}, \varphi_j)$ is the Fourier transform of the image taken at one specific phase step φ_j. $\hat{h}(\mathbf{k})$ is the OTF (Fourier transform of the detection PSF) and $\hat{\rho}_n(\mathbf{k})$ is the Fourier transfom of the dye distribution shifted by $n \cdot \mathbf{k}$ in Fourier space. $|c_n|$ are the Fourier coefficients of the saturated sine squared illumination pattern and are derived in appendix A.2.5.

Thus, this method requires exact knowledge of the saturation factors and the illumination pattern, which directly influence the Fourier coefficients c_n and are essential for solving this system of linear equations. This may prove difficult as the saturation behaviour varies greatly with the environmental conditions (i.e. presence of triplet quenchers in the mounting medium). Therefore, Fourier-type reconstruction was not used for reconstruction of the presented images. One advantage of utilizing Fourier space is the possibility to include arbitrary non equidistant phase-steps φ_i easiliy, as long as they are known. Apart from this, Fourier

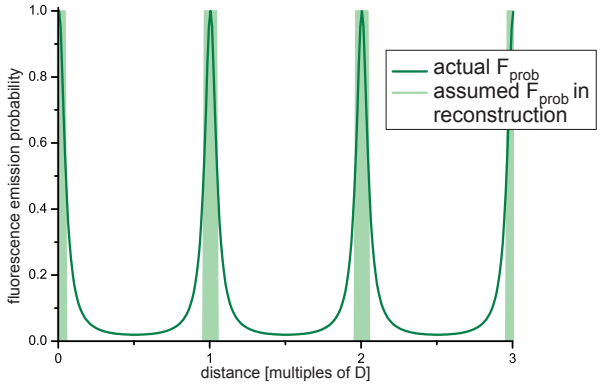

Figure 4.5: **Fluorescence emission probabilities assumed during the reconstruction process**, light green: used for real space reconstruction, dark green: actual, used in Fourier space reconstruction

type reconstruction allows one to use the resolution information contained in the slopes of the fluorescence emission probability $F_{prob}(x)$. In the direct reconstruction, fluorescence emitted from the area of one maximum is added into one pixel, as if the fluorescence emission probability $F_{prob}(x)$ was equally high for every point within that area (see figure 4.5 light green rectangles). In fact $F_{prob}(x)$ varies within the area of one maximum according to the dark green trace. This information is not used in the direct reconstruction, but in the reconstruction including Fourier space.

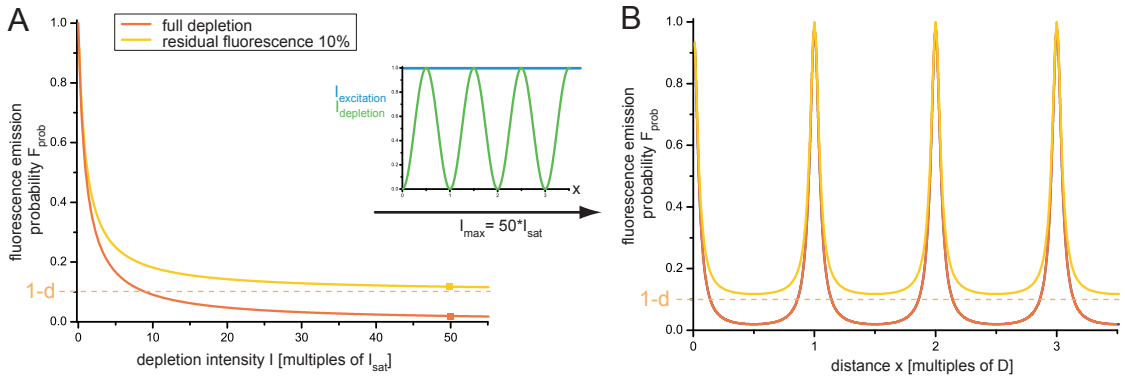

Figure 4.6: **Influence of incomplete depletion on fluorescence emission probability** (A): Saturation curves with complete (orange) and imcomplete (yellow) depletion with a residual fluorescence level of 10% ($d = 0.9$) (B): resulting fluorescence emission probability pattern – exhibits an offset of $(1 - d)$ in the case of incomplete depletion (yellow).

Another general concern which has to be adressed is the apparent incomplete depletion of the fluorescence due to the size of the fluorescence integration time window (gate time), as described previously. Figure 4.6 (A) exemplifies fluorescence depletion with two depletion efficiencies $d = 1$ (orange) and $d = 0.9$ (yellow) (in figure 3.20 d was determined $\approx 92\%$ at a probe pulse of $\approx 3\ ms$). Figure 4.6 (B) shows the effect of incomplete depletion on the fluorescence emission probability $F_{prob}(x)$ (which can be described by the following

equation:

$$\begin{aligned} F_{prob}(x) &= 1 - \frac{d}{1 + \frac{I_0}{I(x)}} \\ &= 1 - d + d - \frac{d}{1 + \frac{I_0}{I(x)}} \\ &= d \cdot \left(1 - \frac{1}{1 + \frac{I_0}{I(x)}}\right) + (1 - d) \end{aligned} \tag{4.1}$$

The first part of the fluorescence emission probability displays the same form as with full depletion, but is scaled down by the depletion factor d (< 1). Underlying the structured fluorescence pattern is a constant offset term of $(1 - d)$. During the imaging process this offset term results in a standard widefield image, which is overlaid in each phase step image. To get rid of this widefield image, which would corrupt the high-resolution information, an additional widefield image is taken before the actual recording. It is downscaled by a factor of $(1 - d)$ and substracted from each single phase shifted frame image during reconstruction.

4.3 Single Beads

4.3.1 Constriction of the Maxima

To be able to see the constriction of the fluorescence signal to subdiffraction-extended positions at the maxima of the sine squared depletion (pumping) light, single silica beads (size $\approx 80nm$) labeled with Atto-532 were imaged at a temperature of $T = 80\ K$. The distance, D, of the interference maxima in the sample plane was $\approx 4.3\mu m$. In figure 4.7 (A) the fluorescence of one single bead is plotted as the phase is changed over 4 periods in $m \approx 24$ steps per period.

When a depletion minimum (zero depletion intensity) is at the position of the bead, its fluorescence will be largest - for example at phase step 20. When a depletion maximum is at the postion of the bead, its fluorescence is depleted and therefore least - for example at phase step 32. With increasing depletion intensity these minima get lower (from blue to red) and the maxima constricted. The depletion level of the minima follow the saturation curves described in figure 3.20. They are optimally zero, but due the incomplete depletion there is some residual fluorescence. Normalization of these data sets (see figure 4.7 (B)) shows a constriction of the fluorescence maxima by a factor of ≈ 2 at the largest applied intensity. With the distance between the intereference maxima D optimized to the lowest possible diffraction limited distance $D = 2 \cdot \Delta x$ (with Δx the FWHM of the detection PSF), imaging using parallelized GSD should result in a resolution enhancement of 2 at a depletion intensity of $\approx 456\ W/cm^2$. Larger intensities should result in even more improved resolution.

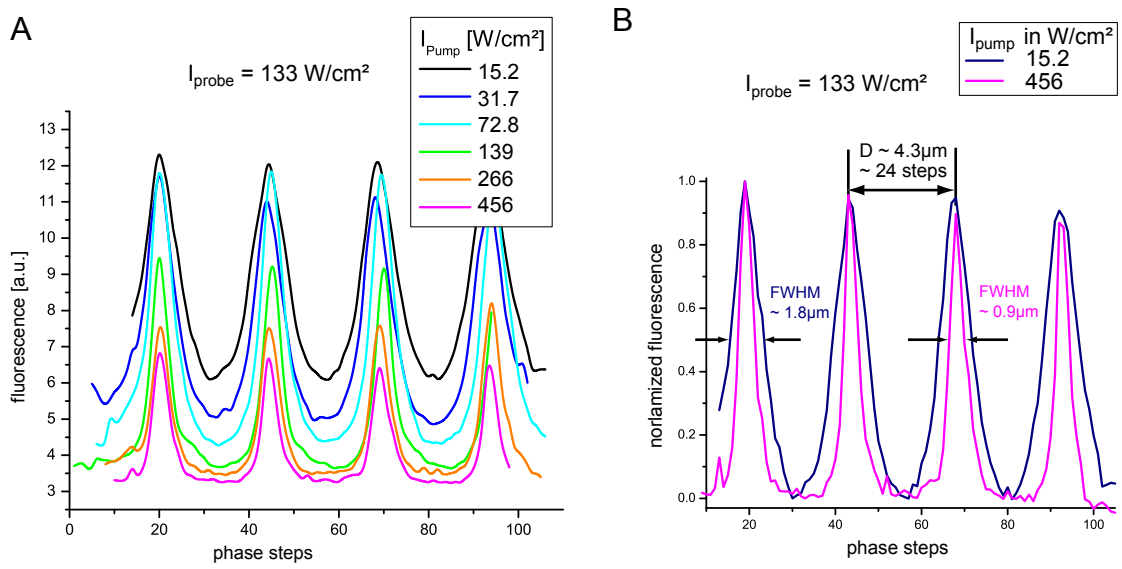

Figure 4.7: **Fluorescence signal of single beads during phase scanning.** (A): fluorescence signal profiles of single beads at different pump (depletion) intensities (B): normalized profiles for two exemplary depletion intensities.

As stated in the previous chapter 2.1 resolution increases with increasing intensity (in the case of GSD, with increasing depletion intensity). It is expected that the width of the fluorescence maxmima decreases with increasing intensity. In part (A) of figure 4.8 the full width at half maximum (FWHM) of the fluorescence traces of figure 4.7 is plotted against the used pump (depletion) intensities (red squares, the red line serves as eye guide only). The FWHM is given in multiples of the distance of the interference maxima $D \approx 4.3\ \mu m \approx 24$ phase steps. $D/2$ the FWHM of the sine squared illumination pattern. The FWHM was determined by imaging one bead as the phase was shifted in $m \approx 24$ steps. The constriction due to the saturation effect decreases the FWHM down to $D/4$, i.e. a factor of 2 below the starting value as stated above. In theory, the FWHM should approach zero for increasing intensities. However, in figure 4.8 the measured FWHM seems to reach a finite value of $0.17 \cdot D$. This is mainly due to optical imperfections as outlined further below. [1]

In figure 4.8 (B) the fluorescence minima are plotted over the applied depletion intensity in black. They follow the saturation curve as measured in the previous chapter, as the depletion intensity in the minima is exactly I_{max}. The green curve displays the difference of fluorescence maximum and minimum of figure 4.7 plotted over the illumination intensity. At low intensities the slope rises and from $\approx 20\ W/cm^2$ falls again. It is expected that the difference between fluorescence maximum and minimum approximates a constant value as the maximum does not change with intensity and the minimum approaches a constant value. The deviation from this behaviour is due to optical imperfections.

The optical imperfections mentioned can stem from a mismatch of the orientation of

[1] In the experimant it is not possible to reach a FWHM of zero, as the imaged beads have a diamter of$\approx 80nm$.

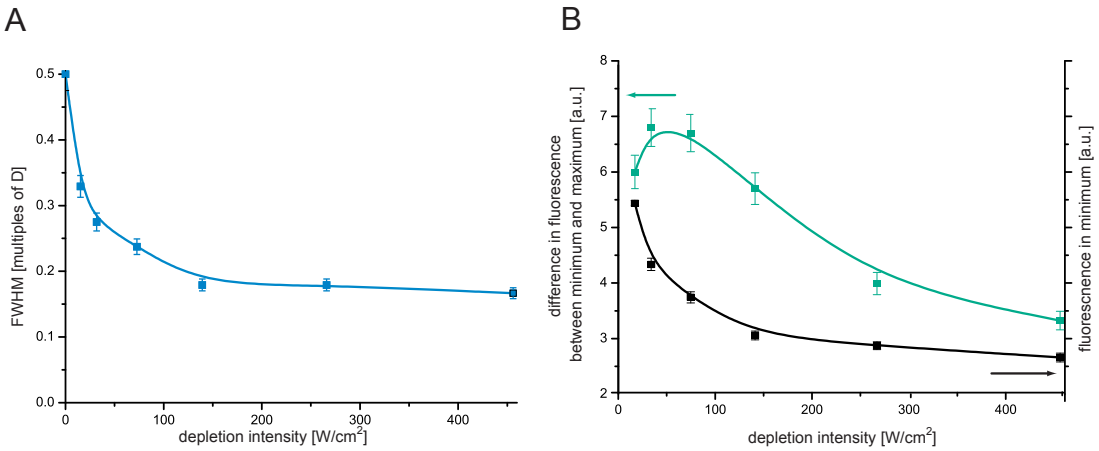

Figure 4.8: **Characterization of measured fluorescence emission probability for increasing depletion intensity**; results of analysis of bead phase scans of figure 4.7; (A): FWHM of single beads in multiples of the distance of maxima of the depletion pattern (B): fluorescence minima over depletion intensity (black) and difference of fluorescence maxima and fluorescence minima over depletion intensity (green).

polarisation of the two interfering beams, scattered light or aberrations. They result in a deviation from the pure sine squared illumination pattern featuring an offset of r (see figure 4.9 (A)). The depletion intensity distribution with a homogeneous offset r can be described by:

$$I(x) = I_{max} \cdot (r + (1 - r) \cdot \sin^2(\pi \cdot \mathbf{x}/D))$$

This illumination pattern is depicted in green in the upper part of figure 4.9. Illumination with this pattern and an intensity of $I_{max} = 50 \cdot I_0$ leads to the fluorescence emission probability pattern of figure 4.9 (B). The purple pattern was simulated with $r = 0$ without any optical imperfections. This case was used for the considerations in chapter 3.1.1. With increasing values for $r = 0.02$ (pink trace) and $r = 0.05$ (yellow trace) the fluorescence emission probability in the maximum is reduced because of the residual depletion light of $0.02 \cdot I_{max}$ and $0.05 \cdot I_{max}$. Figure 4.9 (C) depicts the value of the fluorescence emission probability maxima (i.e. at the depletion minima) over the illumination intensity for the three different values of r. As expected, the maximum is constant at 1 without residual illumination light in the illumination mimimum ($r = 0$), but quenched in case of residual light ($r > 0$). The higher the maximal illumination intensity the more pronounced the quenching of the fluorescence maximum, since the absolute amount of depleting illumination light in the minimum is increasing as well. The black dots display the measured values from figure 4.8 and the blue line the fit using (see appendix for derivation):

$$F_{max} = \frac{\frac{I_{max}}{I_0} \cdot r \cdot (1 - d) + 1}{\frac{I_{max}}{I_0} \cdot r + 1} \tag{4.2}$$

The saturation intensity used was $I_0 = 15W/cm^2$ and the depletion level $d = 0.92$, both determined from the experimental data of figure 3.20. The resulting value from this fit is

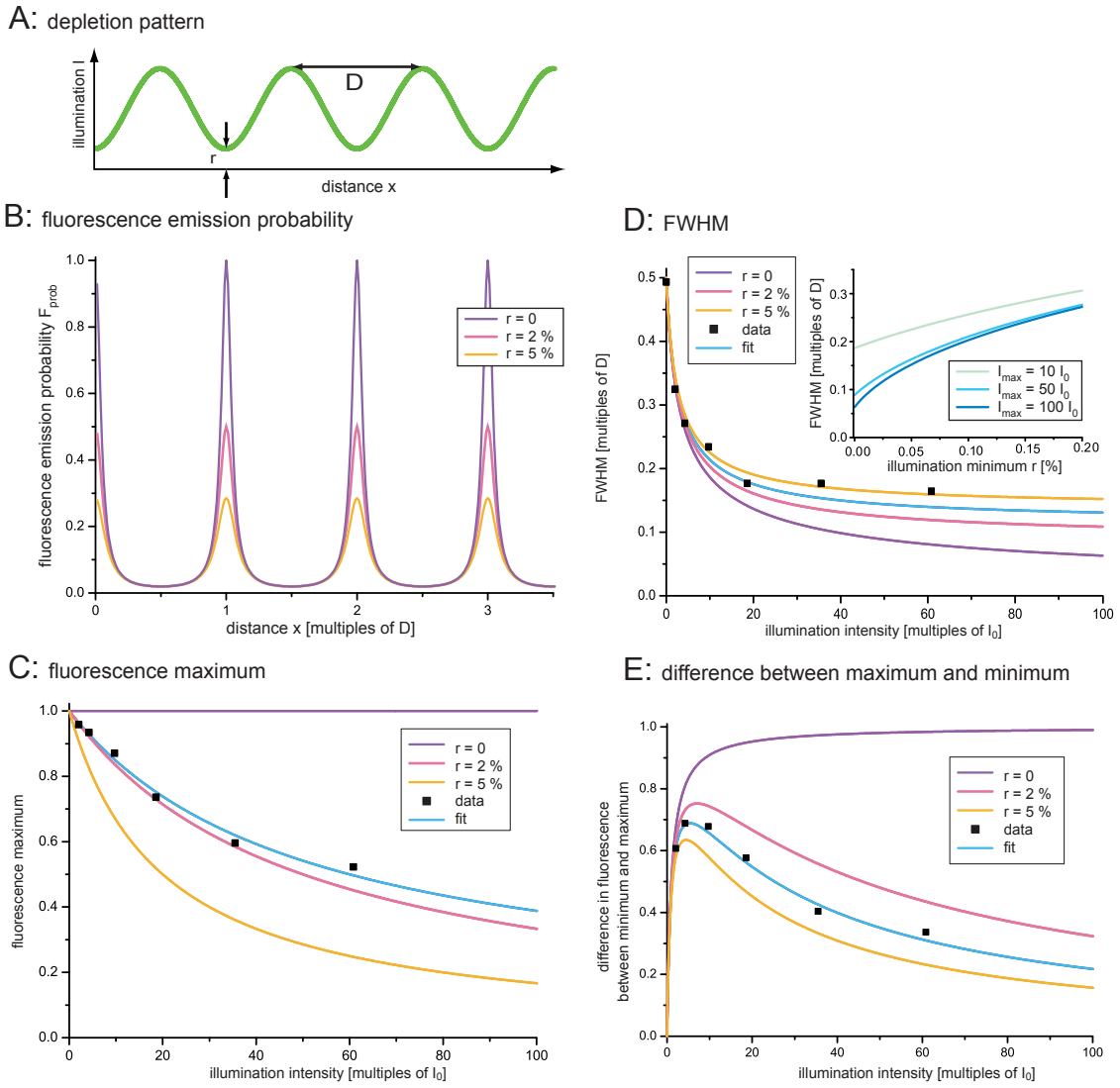

Figure 4.9: **Characterization of theoretical fluorescence emission probability for different levels of r** (A): depletion pattern with imperfect minima (residual intensity in minima r), (B): fluorescence emission probability pattern - peak fluorescence decreases with r, (C): maximum fluorescence including experimental data of figure 4.8 and fit with $r = 2.2\%$, (D): FWHM of the fluorescence emission probability depending on the depletion intensity and the offset r, including experimental data and fit with $r = 3.4\%$, (E): difference of maxima and minima, including experimental data of figure 4.8 and fit with $r = 3.4\%$.

an offset of $r = 2.2\%$. For comparison, the yellow, pink and purple traces were simulated with complete depletion ($d = 1$). The effect of $d < 1$ results in a multiplication of the depletion saturation function with d and the addition of an offset $1 - d$. This offset explains the difference between the simulated pink trace for $r = 2\%, \& d = 1$ and the fitted blue trace for $d = 0.92$.

In figure 4.9 (D) the FWHM is simulated with increasing depletion intensity I_{max} for three different values of r (0, 0.05, 0.05) (for the calculations see appendix A.2.8). Start-

ing at $0.5D$, which is the FWHM of the sinesquared depletion pattern, the FWHM decreases with higher depletion intensity as expected. With higher levels of r there is still a decrease in FWHM, but not as large as for $r = 0$. The inlay shows the dependence of the maximal achievable FWHM on the value of r for three fixed values of I_{max}. The more residual depletion light in the minimum, the worse the resolution, i.e., the larger the FWHM of the fluorescence emission probability. In the case of $r = 0$, the maximal achievable FWHM is zero, hence the possible resolution unlimited, in the case of $r \neq 0$ the FWHM$= 2/\pi \arccos \sqrt{1/(1+r)}$. Since the possible resolution depends on the FWHM, it strongly depends on an optimized illumination pattern with as little illumination offset r as possible. The black dots once more display the measured FWHM from figure 4.8 and the blue line the fit with equation 4.2 and $r \approx 3.4\%$. The incomplete depletion $d < 1$ hardly affects the FWHM (see 4.6), because the factor d only rescales the fluorescence emission probability, and is therefore neglected in the fit.

Part (E) of figure 4.9 shows the difference of maximum and minimum in the fluorescence emission probability over the illumination intensity. This difference is effectively the signal used for imaging. In the case of $r = 0$ this resembles a reverse depletion saturation curve (purple trace), because the maximum is constant at 1 (see part (C)) and the minimum decreases in accordance to the depletion curve from figure 3.20. For $r \neq 0$ the curves are different (pink and yellow trace). For very low illumination intensities there is no difference, but for larger intensities they do not asysmptotically approach the maximum of 1, but drop off again. This is due to the quenching of the fluorescence maxima (see part (C)). This behaviour is seen in the experimental data of figure 4.8 part (B), which has been introduced into this figure. The blue line is a calculation applying $r = 3.4\%$ and $d = 0.92$, with which the data can be overlaid very well.

Comparing the measured data with these simulations for (C)–(E) leads to an estimated offset in the minima of the depletion light $r \approx 2\% - 3\%$. The most direct way of determining the level of r is by the reduction of the fluorescence maxima (i.e. $r = 2.2\%$), the other two methods are indirect and more prone to error due to noise.

Optical imperfections leading to residual light in the minima of the depletion pattern give a reduced FWHM and therefore a lower possible resolution and a reduction of the signal, i.e. the difference of maximum and minimum fluorescence (see figure 4.9). With a certain level of noise present within the measurement the signal to noise ratio strongly depends on the perfection of the minima (r as small as possible). The smaller the signal-to-noise ratio the more noise will affect the quality of the high resolution image. Therefore, the effect of imperfect depletion minima is two-fold, firstly deteriorating the FWHM and secondly reducing the signal and the signal-to-noise ratio.

As stated before, incomplete depletion $d < 1$ merely acts as a scaling factor in the depletion function $F(I)$ and does not alter the FWHM, but it decreases the difference between fluorescence maximum and minimum, leading to a lower signal-to-noise ratio. The decrease in signal-to-noise ratio can be avoided by using longer multiple illuminations and fluorescence acquisitions at one phase position, but this may give rise to stronger bleaching. The effect of imperfect zeros on FWHM and resolution cannot be helped by any imaging method

but has to be avoided from the start, possibly by introducing optical elements to achieve an optimal illumination pattern, which was not done in this project.

4.3.2 Images

Fluorescent beads are the most obvious objects for testing the resolution of an imaging method, since they resemble a pointlike emitter. A cover glass was prepared with beads (Microspheres 540/560, diameter $100\ nm$), whose absorption maximum is at $540\ nm$ and their emission maximum at $560\ nm$. Before imaging, a pump-probe saturation (depletion saturation) curve was taken at a temperature of $T = 80\ K$ (see figure 4.10) to determine the saturation intensity I_0 and the fluorescence depletion level d, as these beads were stained with a different dye. The depletion efficiency is $d \approx 15\%$, leaving a substantial part of still diffraction limited information in the image which has to be subtracted (see figure 4.6 in section 4.2). A saturation intensity $I_0 \approx 8\ W/cm^2$ is determined, which is slightly lower than that measured for beads labeled with Atto-532 ($I_0 \approx 15 W/cm^2$)), but still within in the same order of magnitude.

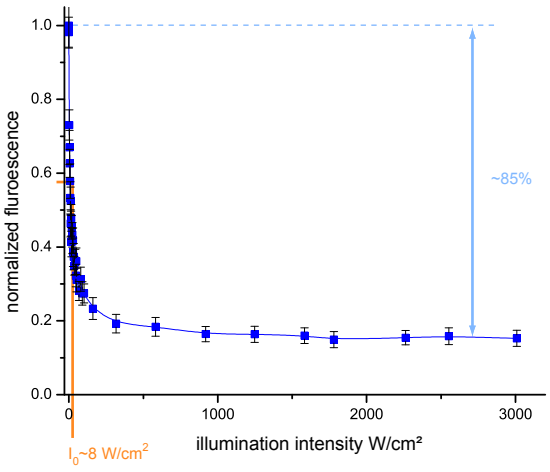

Figure 4.10: **Fluorescence saturation of beads probed with increasng depletion intensity** (Microspheres 540/560), $I_{Probe} = 133\ W/cm^2$, probed for $3\ ms$

Figure 4.11 (A) is an example of a reconstructed image of beads taken with parallelized GSD. The image acquisition process was not completely correct, as the phase scanned by the phase steps was smaller than one period. This leads to abrupt changes in measured fluorescence for objects in the region, where two adjoining stripes meet. Fluorescence profiles show sharp edges (B), which do not reflect dye distributions within the sample. In (B) only the middle peak shows the profile of a complete bead, while the two outer peaks have very sharp edges on their left side, which stem from a mismatch of the phase-scanning distance, $m \cdot \Delta s$,and the period, D.

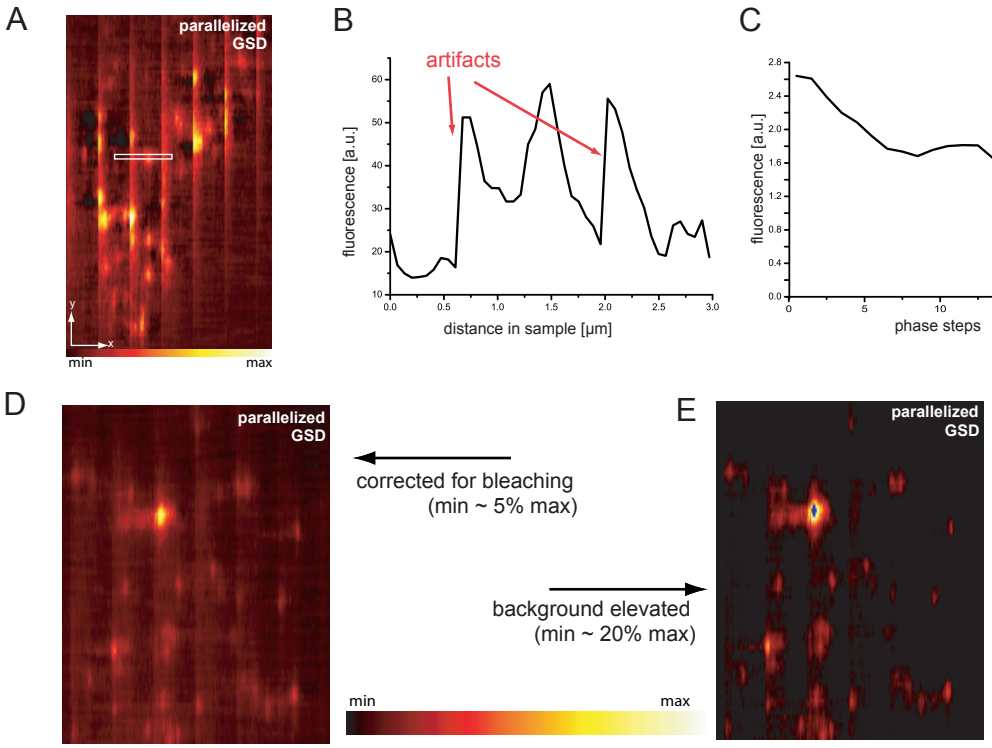

Figure 4.11: **Reconstruction with artifacts** (A): reconstructed image with sawtooth in fluorescence (B): y-profile with sharp edges due to incomplete phase scanning (information missing) (C): fluorescence decay during imaging (over phase steps) (D): image of beads corrected for bleaching (E): image of beads with adapted background

Figure 4.11 (C) shows the total fluorescence of the image of each phase step. The decrease of fluorescence from the first to the last phase step reflects photo-bleaching. In the reconstructed image bleaching imposes a sawtooth-like modulation onto the fluorescence signal. To counteract artifacts by this modulation each phase step image was rescaled by dividing the measured fluorescence signal by the profile of the phase-step images (for example given in (C)). Only the fluorescence signal is bleached, but not the background. Rescaling each phase image by the decrease in signal due to photobleaching corrects the fluorescence signal, but alters the background. In the first phase-step image the original fluorescence signal is larger than in the last phase-step image, therefore, after division, the resulting background of the first corrected phase-step image is lower than the background of the last. Thus the sawtooth modulation is transferred from the fluorescence signal to the background. Figure 4.11 (D) displays an example for such a bleaching-corrected image. The background clearly shows a sawtooth modulation. The max and min values used for representation are exactly the values of the highest and lowest fluorescence photon count rate (with $min/max \approx 5\%$). Figure 4.11 (E) is the same image, but with changed representation. The count rates for min was chosen to be higher, so that $min/max \approx 20\%$, and count rates smaller than min appear black as well. This can be compared with subtracting a constant

value from the whole image. By doing so, the interesting features such as the beads are brought out more clearly, whereas the modulation of the background is suppressed. Bleaching correction and background suppression had to be done in some of the reconstructions.

Figure 4.12 shows an image fluorescent beads taken with widefield illumination (upper part, left) and parallelized GSD (upper part, right). To further highlicht details and suppress background modulations the offset was disguised by choosing $min \approx 15\%$ and $min \approx 20\%$ of max signal for widefield illumination and paralellized GSD, respectively.

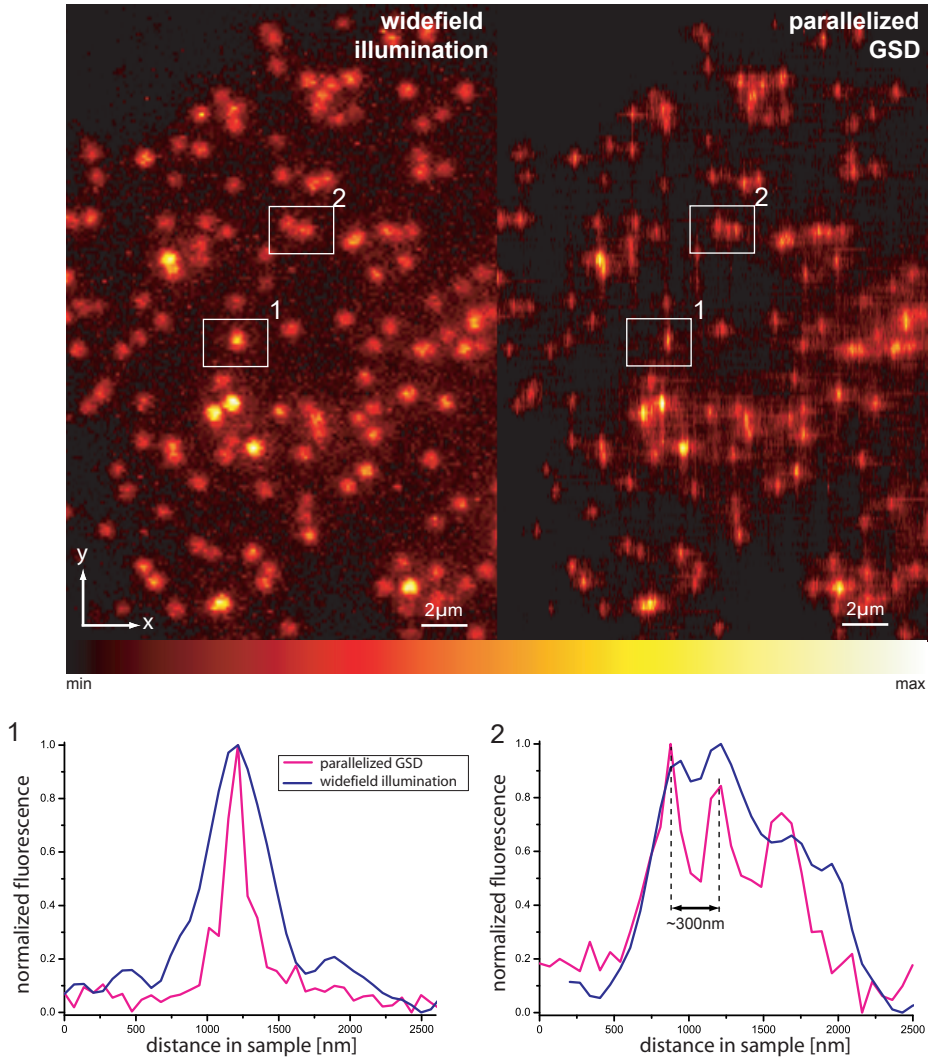

Figure 4.12: **Widefield and high resolution parallelized GSD image of fluorescent beads** Upper part images: widefield illumination (left) and parallelized GSD (right) with $I_{pump} = 450\ W/cm^2$; Lower part: profiles along the direction of x

The resolution enhancement due to parallelized GSD imaging (right part of figure 4.12)

can be clearly seen by comparing single beads with the conventional widefield image (left part). In the direction of the modulation, x, the size of the beads is smaller than in the direction perpendicular to the modulation, y, which is still diffraction limited, and results in oval shapes instead of round shapes in the left part. Additionally, beads can be better separated, as is shown in the line profiles in the lower part of figure 4.12. Number 1 is the profile of one single bead with widefield illumination (blue) and parallelized GSD (pink). The FWHM is reduced by a factor $2-3$ due to parallelized GSD. For the second profile (2) a group of beads has been chosen. With widefield illumination (blue) a slight modulation close to noise level is visible, which could well be due to noise. When the sample is imaged with parallelized GSD the three single beads can be clearly discriminated.

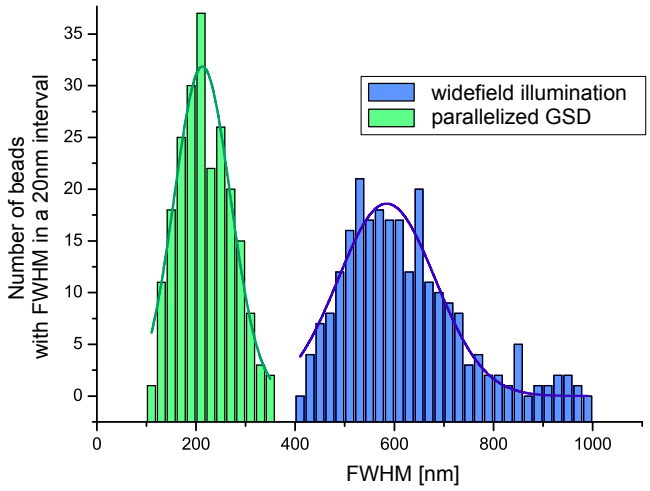

Figure 4.13: **Histogram of measured FWHM of fluorescent beads** (Microspheres 540/560, size 100nm) with widefield illumination($N = 224$, blue) and parallelized GSD ($N = 218$, green) , probe intensity $I_{probe} = 105 W/cm^2$, different pump intensities $I_{pump} = 300 - 1130\, W/cm^2$

To evaluate the enhancement in resolution, the FWHM of 231 beads imaged with widefield illumination and 218 beads imaged with parallelized GSD were determined along x as shown in the histrogram of figure 4.13. The FWHM-histograms were fitted with a gaussian function of the form

$$f(d) = A \cdot \mathrm{e}^{-\frac{(d-d_c)^2}{w^2}}$$

centered around d_c with a width of w. For widefield illumination the center is at $580 \pm 6\, nm$ with a width of $136 \pm 6\, nm$, whereas with parallelized GSD the center is at $213 \pm 4\, nm$ with a width of $79 \pm 4\ nm$. The difference in distribution width and especially the long tail in the case of widefield illumination may stem from estimating the FWHM from two agglomerated beads that could not be discriminated as two single ones in the widefield image and were therefore mistakenly taken as a single bead (with a higher FWHM). Comparison of the centers of the FWHM distributions leads to a resolution enhancement of ≈ 2.7. The

pump (depletion) intensity applied for this resolution enhancement ranged from $I_{pump} = 300 - 1130\,W/cm^2$. Although theoretically a further increase in resolution is expected when the pump (depletion) intensity is increased this could not be seen in the images. This is in good agreement with the experimental results in figure 4.9, as the residual light in the minima of the depletion pattern corrupts the possible resolution. As an example in figure 4.14 the histrograms for $I_{pump} = 300\,W/cm^2$ (blue) and $I_{pump} = 710\,W/cm^2$ (red) are displayed.

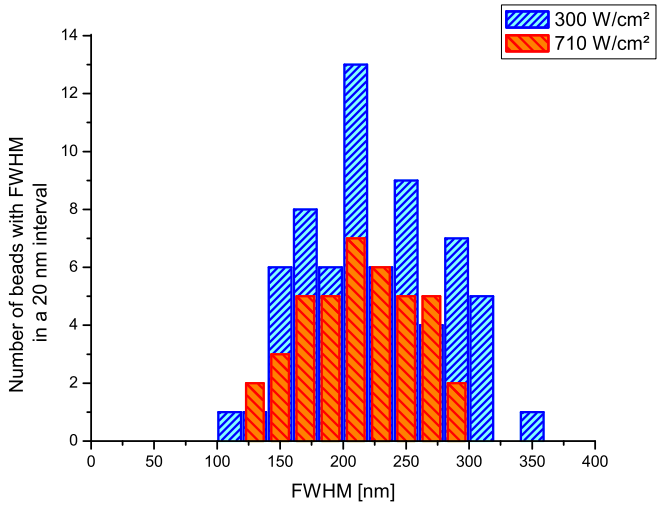

Figure 4.14: **Comparison of FHWM for two different pump intensities**: FWHM of beads (Microspheres 540/560 beads, size 100nm) at two different pump intensities $I_{pump} = 300\,W/cm^2$ (blue) and $I_{pump} = 710\,W/cm^2$ (red), probe intensity $I_{pump} = 105\,W/cm^2$

Gaussian fits show that the centers of these two distributions are approximately the same: $d_c(300W/cm^2) = 210 \pm 9nm \approx d_c(710W/cm^2) = 216 \pm 4nm$, even though their depletion intensities differ by a factor of 2. This is due to the imcomplete minima in the sinesquare illumination pattern described above (see figure 4.9). The effect of a few percent illumination light in the minima leads to a reduction of the fluorescence at these illumination minima. At the same time the FWHM is not reduced by an increase in illumination intensity. Therefore higher pump intensities did not lead to a larger enhancement of resolution.

In summary, the application of structured illumination leads to a resolution enhancment by a factor of ≈ 2.7. This factor could not be further increased due to imperfections in the structured pump illumination pattern. At the same time the fluorescence diminishing effect of bleaching had to be counteracted by a rescaling of the fluorescence signal which caused some artifacts in the reconstructed images.

4.4 Biological Imaging

To prove the capability of parallelized GSD for subdiffraction imaging in biological samples, microtubuli of mammalian cells were stained with Atto532 via secondary antibodies (see appendix A.1.2), mounted in mowiol and imaged at a temperature of $T = 80\ K$ using parallelized GSD (see protocol in appendix A.1.2). Figure 4.15 shows two images of these cells.

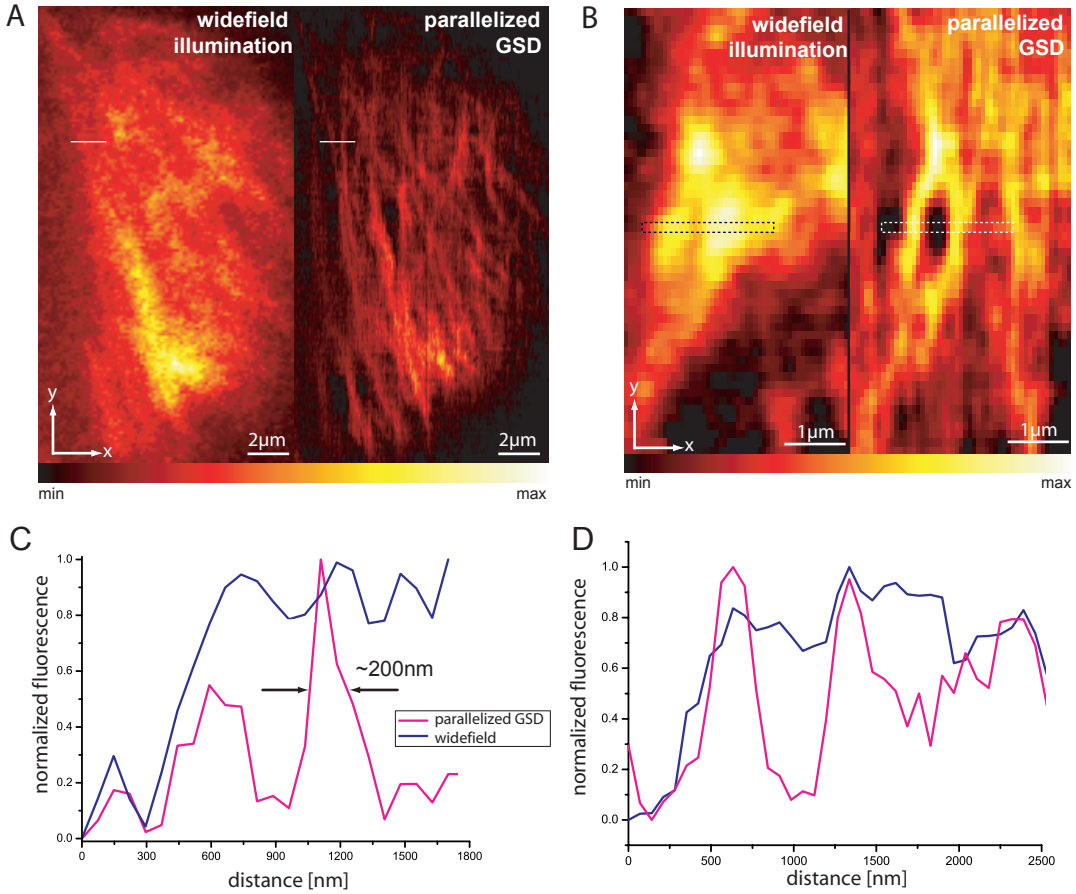

Figure 4.15: **Images of Microtubuli with widefield and parallelized GSD**, (A): left min $\approx 4\%$ of max, (A): right min $\approx 11\%$ of max, (B): left min $\approx 40\%$ of max, (B): right min $\approx 34\%$ of max, $T = 80\ K$, (C): and (D): profiles along x of lines marked respectively (both interpoated using Lagrange 3^{rd} order, factor 1.5)

Microtubuli are hollow tubular structures made of polymerised tubulin with a diameter between $15 - 25\ nm$, but due to secondary antibody staining the radius of the fluorescent structures is larger by $\approx 10 - 20\ nm$. They are part of the cellular cytoskeleton and take part in celldivision. Microtubuli are used by the motorproteins dynein and kinesin for their movement through the cell. Because of these cellular functions they are arranged as quasi-parallel fibers throughout the cell. Being aligned along one spatial dimension within each cell, they present an ideal imaging object for a microscopy technique with increased resolu-

tion along only one lateral dimension. The cells were oriented arbitrarily on the cover slip. Cells were selected for imaging, the orientation of whose microtubuli was perpendicular to the modulation of the parallelized GSD.

Parts (A) and (B) of figure 4.15 show two parts of a microtubular network imaged with widefield illumination (left) and parallelized GSD (right). Part (A) shows a tubular meshwork and the enhancement in resolution can clearly be seen by comparing the images with widefield and parallelized GSD. In the right part single fibers can be discriminated, whereas the same region is blurred in the left part. Exemplarily the profile through two of the microtuli is displayed in part (C). The profile clearly shows that two neighbouring fibers can be distinguished by parallelized GSD (pink trace), whereas the profile at the same position shows only a slight modulation in the widefield image, whose contrast is not sufficient to discriminate the two fibers. The FWHM of one of the fibers in the parallelized GSD image is $\approx 200\,nm$, which agrees very well with the FWHM of the beads, showing the resolution limit of this method (see previous section).

The right part of 4.15 (B) shows a ringlike structure or two fibers crossing each other. In the widefield image (left) these two fibers cannot be discriminated, there is merely a dip in the associated profile (blue trace, part (D)). The profile of the parallelized GSD image (pink trace) clearly allows one to discriminate two fibers and even shows an area without fluorescence staining in between the two fibers.

In conclusion, parallelized GSD in combination with low temperatures is a possibility for high resolution cellular imaging. The achieved FWHM of $\approx 200nm$ is in good agreement with the values measured in beads.

4.5 Improvements

Resolution enhancement in one lateral direction was shown for beads and for a biological sample, but higher resolution in more than one direction and even live-cell imaging is essential for many biological problems. This section will present possible improvements to the current setup.

Objective lenses with higher numerical aperture

The current setup uses a microscope objective lens with a numerical aperture NA$= 0.7$. The resolution achievable with parallelized GSD depends on the distance D of the pattern minima, which in turn depends on the diffraction limit of the detection opticts and therefore on th NA (see figure 4.3). Using microscope objective lenses with larger NA, presently $NA = 1.5$ at max) should entail higher resolution. Nonetheless, the numerical aperture does not influence the resolution enhancement relative to the conventional widefield image taken with the same detection optics of a factor of $\approx 2 - 3$, that was achieved in the presented work.

The reason why using a microscope objective lens of such low NA is the need of a rather long working distance to match the distance between the front lens of the objective lens and the sample. The sample is mounted inside the cryostat, whereas the objective lens is outside, giving a minimum distance of $\approx 2\ mm$. This distance could be decreased by putting the objective lens inside the cryostat. In this case, the objective lens would be cooled down as well, possibly causing mechanical stress to the metallic and glass components of the objective lens. Such an optical setup would probably require the design of special cryo-objectives and a redesign of the cryostat. By including the objective lens into the cryostat the use of an immersion medium (e.g a solid immersion lenses which can increase the NA up to 2.5 by the use of a high-refractive material) would become possible, which would further increase the detection NA.

Correction of optical imperfections

One major obstacle for reaching better improvement in resolution than the observed factor of $2-3$, was the imperfect minima in the depletion pattern, which caused depletion of the fluorescence maxima and did not allow the FWHM to decrease as expected (see figure 4.9). Different approaches were taken to achieve interference pattern in the focal plane of the microscope such as: (1) A Michelson-Morley interferometer, (2) splitting the beam by a polarizing beam splitter and turning the polarization of one arm by a $\lambda/2$ plate, (3) illuminating the sample not via the objective lens, but from the opposite side by two single beams, (4) diffraction gratings to create two single beams and (5) a liquid crystal display for modification of the wavefront. The creation of interference as presented in the beginning of this chapter by the use of a Mach-Zehnder interferometer gave the best results with respect to minimizing light in the minima ($< 1\%$). The quality of the interference pattern in the focal plane is mainly compromised by stray light, aberrations or unwanted reflections, which all could not be avoided in the current setup. Several air-glass surfaces (objective lens – air, air – cryostat window – air, air – front cover slip, back cover slip – air – sample table) cause reflections and aberrations. They are possibly better avoided even more improved optical elements and putting the objective lens inside the cryostat as outlined above. Another possibility to create a structured illumination pattern might be the use of a liquid crystal display, which at the same time can correct wavefront aberrations.

A mismatch in polarization or intensity of the two interfering beams creating the depletion pattern with respect to each other or a slight deviation of both polarization directions from the direction perpendicular to the plane spanned by the two beams can as well result in a residual depletion intensity in the interference minima. Although checked before each image acquisition, such imperfections might still be present.

Image reconstruction via Fourier Space

In the present work, final image reconstruction of the patterned image at different phase positions of the depletion pattern has been performed in real space. This represents a simple and straightforward reconstuction approach. Slightly higher resolution might be achieved by us-

ing the Fourier space for the image reconstruction. The reconstruction approach via Fourier space allows one to exploit the resolution information contained in the steep slopes of the fluorescence emission probability (figure 3.7). In the present approach, using real space, the emitted fluorescence is assumed to originate from a line of a certain width with homogeneous "illumination" intensity. However, in reality the fluorescence emission probability is not homogeneous, but features steep slopes. The slopes are ignored in the present approach, but might contain additional high-resolution information. The image reconstruction applying Fourier space can be compared with the confocal deconvolution, where knowledge of the illumination/detection PSF is used to extract additional high-resolution information available in the image.

As briefly discussed before, the involvement of Fourier space requires exact knowledge of the illumination pattern and of the saturated depletion characteristics, which may prove difficult as the triplet population, and thus the saturation behaviour, might vary strongly with environmental conditions (e.g. mounting medium, presence of oxygen (figure 3.12 and 3.13)). The possible resolution comparing the direct reconstruction method and the deconvolution-type method involving Fourier space cannot be put into numbers, as the second depends strongly on the noise level present during imaging (figure 3.8).

Reconstruction applying Fourier space was not used in this work, because the limitations in resolution due to optical imperfections is larger than the gain expected from Fourier reconstruction.

Expansion into all lateral dimensions

The concept of parallelized GSD was presented for one lateral dimension only, but can easily be expanded to both lateral dimensions by illuminating the sample consecutively with a rotated structured illumination pattern or simultanously with a pattern that is modulated along both lateral dimensions.

The first approach using rotation of the pattern can for example be realized by the use of a dove prism (see right) which leads to an inverted image. A beam of light entering one of the sloped faces of the prism undergoes total internal reflection from the inside of the longest face and emerges from the opposite sloped face. Images passing through the prism are flipped, and because only one reflection takes place, the image's handedness is changed to the opposite sense (see the two "F"'s in figure 4.16). When the prism is rotated along the longitudinal axis, the transmitted image rotates at twice the rate of the prism. This allows one to rotate an image or the interfering beams and thus the depletion pattern by an arbitrary angle. This prism (and additionally two $\lambda/2$- plates to take care of the polarization direction) can be inserted into the setup at the position of the intermediate focal plane. Two or more sets of images (with shifted phases) would be taken consecutively, leading to images with high resolution along the rotated modulation. The necessary recon-

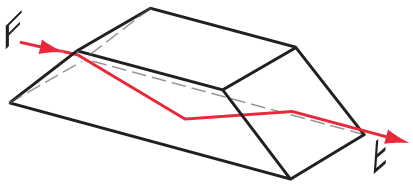

Figure 4.16: **Dove prism for image rotation** by total internal reflection

struction process is more sophisticated and might have to be done with the use of Fourier space.

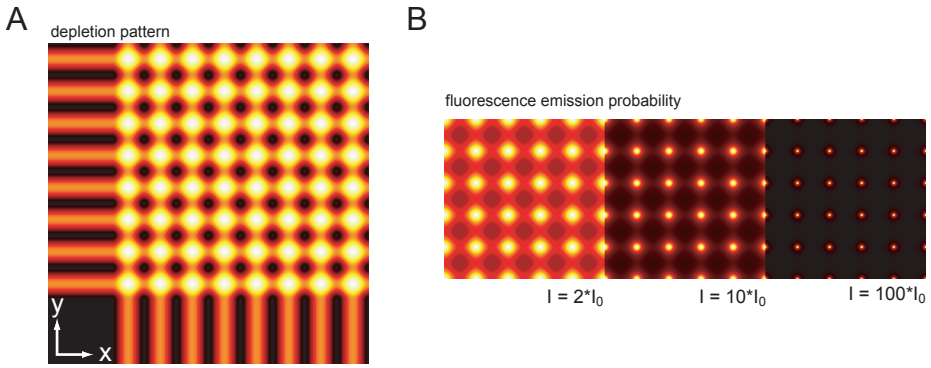

Figure 4.17: **Simulated interference grid** (A:) by overlaying two perpendicular interference pattern in x and y; (B): fluorescence emission probability at three different depletion intensities

Another alternative for multi-lateral high-resolution imaging would be to illuminate with an interference grid, instead of an interference fringe pattern. This can for example be achieved by overlaying two perpendicular interference pattern as illustrated in figure 4.17 A. Therefore, a second interference cavity has to be introduced into the experimental setup in parallel to the first. For optimal interference within one cavity, each polarisation should be parallel to the interference fringes, hence perpendicular to the polarization in the other cavity. Both pattern can then be overlaid by the use of a polarisation beam splitter. The resulting gridlike interference pattern is the sum of the two interference fringes with zero intensity only at the positions where both interference fringes are zero (see figure 4.17 (A:)). The intensity profile along one maximum of the x-modulation is not constant however, but is modulated. The same is true for the direction y. This affects the fluorescence emission probability at depletion intensities close to the saturation intensity I_0, but is not significant at high saturation factors (see figure 4.17 (B)). The different polarisation direction along the two modulations does not alter the resolution as long as there is no polarization anisotropy in the dye molecules in the sample.

Other illumination pattern are possible as well, for example by applying a LCD to manipulate the wavefront. However, it would go beyond the scope of this thesis to discuss that in detail.

Expansion to the third dimension the along optical z-axis

So far the presented method could only increase resolution within the focal plane. The resolution along the optical axis is the same as in conventional widefield microscopy, limiting the possible sample thickness to $< 1\ \mu m$. A rather harsh possibility to counteract this limitation is to cut the samples to slices of $<< 1\ \mu m$ thickness, optimal to below the diffraction limit along the optical axis. Subsequent imaging of each slice and reconstruction to a 3D-image will realize axial resolution $<< 1 \mu m$.

Another less invasive method would be the optical selection of a plane, for example by interference of two beams along the optical axis, as is implemented in 4Pi or the I5M-microscopy ([32], [33]). By adjusting the optical retardation between these two beams to have destructive interference in the focal plane of the detection optics and combining that with fluorescence depletion allows one to select a single plane with sub-diffraction resolution. However, one has to take care of interference sidelobes, e.g. by deconvolution with the known interference pattern along the optical axis.

Live-cell imaging

Real live-cell imaging is not possible at vacuum conditions and $80\ K$. To still be able to get images from cellular processes, it is possible to take an image of a sample at $80\ K$, and subsequently heat the sample locally, for example by exposure to an infrared laser of high power, thus reactivating some processes. After the heat-exposition the sample freezes again and the next image can be taken at low temperature ([34]). Repeating this process several times would allow one to get a series of snapshots of the cellular process with high resolution, providing a movie of cellular mechanisms. Several requirements have to be met for this unfreeze type live-cell imaging to work. First, the applied dye has to exhibit least possible bleaching to allow a series of images to be taken, which is most probable while imaging at low temperatures. Second, the mounting medium of the cell should not become crystalline at low temperatures which would destroy cellular structures and processes. It would have to withstand the forces exerted by evacuating the cryostat, and most importantly it should not stop the cellular process when the sample is locally heated and shock-frozen repetitively.

5 Discussion

To circumvent the limited resolution imposed by the diffraction limit in fluorescence microscopy, RESOLFT microscopy was introduced to go beyond this physical limit. RESOLFT needs as large intensities as possible, which might cause severe photobleaching. Further, the variants of RESOLFT implemented so far rely on single-point scanning, leading to rather long image acquisition times.

This work presented a RESOLFT-type microscope applying parallelized ground state depletion (GSD) to achieve subdiffraction resolution. Parallelization allowed rather fast image acquisition times by simultaneously illuminating and detecting a $20\ \mu m \times 20\ \mu m$ area of the sample. To increase photostability, the sample was evacuated and cooled to approximately $80\ K$. To deplete the fluorophore´s ground state, a steady state population of the singlet and triplet states was prepared by illumination of the sample with a $\approx ms$-long pump pulse of large intensity and the resulting singlet population was immediately probed by a second $\approx ms$-long probe pulse. To reset the sample before the following pump-probe sequence the sample was exposed to light of different wavelength to deplete the triplet state via reverse inter-system-crossing. The fluorescence response during the probe pulse decreased with increasing pump intensities, displaying a saturated depletion behaviour with a saturation intensity of only $I_0 \approx 15 W/cm^2$.

Applying this saturation behaviour to a pattern of line-shaped intensity minima (created by the interfernece of two beams in the sample plane) led to the formation of subdiffraction sized line-shaped regions in which fluorescence was possible. The fluorescence from these regions was imaged onto a camera with neighbouring lines separated by more than the diffraction limit of the fluorescence widefield-detection, avoiding lateral cross talk this way. For the final image construction, the signal recorded in separate areas of the camera could be reassigned to the corresponding subdiffraction areas of signal origin. Scanning the interference pattern across the sample and reconstructing a final image from each single frame realizes an image with sudiffraction resolution at a recording time that is significantly smaller than in previously demonstrated high-resolution point-scanning approaches is achieved. In comparison to RESOLFT applying STED, with saturation intensities as large as $10^8 - 10^9\ W/cm^2$ the presented pump-probe GSD-approach needs only very few W/cm^2 and avoids photostress of both fluorescent marker and sample.

In the RESOLFT experiments applying parallelized GSD a practical resolution of $200nm$ was proven, which is a resolution enhancement of approximately $2 - 3$ compared to conventional imaging. Currently, the relative resolution enhancement is mainly restricted by the optical imperfections of the zero intensity lines due to e.g. aberrations, which can be corrected for by improving e.g. the optical elements. An even more improved absolute resolution would readily be achievable by applying an objective lens with higher NA. Such an

objective lens could not be applied in the current project due to the large working distance necessary in the cryostat setup. A complete redesign of the cryostat would enable to introduce better objective lenses with large NA. Further improvements, such as the expansion of the resolution enhancement to all lateral directions and to the direction along the optical axis are straightforward, as presented in the last chapter. The implementation of heat-shock freeze cycling would even allow one to adapt subdiffraction low temperature GSD imaging to life cells.

Recently, subdiffraction PALM (**p**hoto**a**ctivation **l**ocalization **m**icroscopy) microscopy was developed based on single-molecule fluorescence detection, reaching subdiffraction resolution on a camera-based widefield setup. PALM is based on localizing sparsely activated, single fluorophores at a time well separated in space. However, this stochastic single molecule procedure requires rather long image acquisition times (between $2 - 12\ h$, [35]). As for parallelized GSD, PALM also still lacks enhanced resolution along the direction of the optical axis. The achievable resolution of the PALM method is high down to $40\ nm$, but on the other hand it is prone to artifacts as it relies on single molecules statistics, whereas parallelized GSD microscopy directly utilizes dye ensembles.

Overall, parallelized GSD presented a new straightforward approach to reach subdiffraction resolution in fluorescence imaging with (i) very fast image acquisition (ii) possible utilization of any fluorescence marker, since the triplet state is an intrinsic property of a fluorophore and its population is generally enhanced at low temperatures and vacuum conditions, and (iii) since working at low temperatures realizing highest photostability which is an important requirement in fluorescence microscopy. It is expected that the presented approach will bring resolution towards the molecular scale and offer new exciting insights into biological imaging.

A Appendix

A.1 Materials and Methods

A.1.1 Sample Preparation

Fluorescent Beads

There were two types of beads used in the experiments: Fluospheres from Molecular Probes and self-synthesized fluorescent particles.

1. FluoSpheres® from Molecular Probes are carboxylate-modified polystyrene microspheres of a diameter of 100nm (coefficient of variation $\approx 5\%$) in the colors Nile red (absorption maximum $535nm$, emission maximum $575nm$), Orange ($540nm$, $560nm$), Red-orange ($565\ nm$, $580\ nm$). Stock solutions provided by Molecular Probes (Molecular Probes, Invitrogen Crop., Eugene, OR, USA) with $\approx 1.0 \cdot 10^{10}\ \text{beads}/mL*$ were further diluted by a factor of 100 to 1000. Cover slips were immersed for $\approx 10\ min$ in Poly-L-Lysin, washed with clean water and then immersed to the bead solution for $\approx 10\,min$. The supernatant was siphoned off and the cover slips washed again in clean water.

2. Fluorescent particles were prepared by Mariano Bossi with the dyes Rhodamine-6G and Atto532 (both Molecular Probes, Invitrogen Crop., Eugene, OR, USA) according to the following protocols:

Rhodamine-6G particles: Particles with non-fluorescent cores of diamter of $52\ nm$ (TEM) were synthesized in a water-in-oil microemulsion ([36], [37]). For coupling $0.57\,mg$ ($1\,\mu mol$) of Rhodamine-6G carboxylate NHS esther and $1\ \mu l$ of (3-aminopropyl) triethoxysilane (APS) were dissolved in $200\,\mu l$ of absolute ethanol. The mixture was stirred and allowed to react overnight in the dark. The fluorescent shell was grown onto the cores via microemulsion technique (seeded growth, [38], [39]). The total amount of APS-Dyes reacted overnight were used to grow a fluorescent shell onto the cores of $52\,nm$ diameter previously prepared. The mixture was added to a solution containing $8ml$ of ethanol, $10ml$ of a suspension of the cores ($46\,\mu mol\,\mathrm{SiO_2}/ml$), and $300\,\mu l$ of triethoxysilane (TES) in ethanol. The reaction was started with the addition of $1.5\ ml$ of ammonia ($1.1\ M$ final concentration). The amount of TES was selected to grow the particles to a theoretical radius of $40\ nm$ ($\oslash = 80\ nm$). The ratio TES/Dye was kept low (about 1000), to avoid dye-dye interactions. The experimental diameter measured by transmission

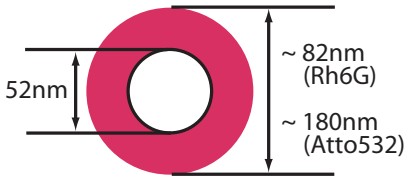

Figure A.1: Core and Shell of fluorescent beads

electron microscopy (TEM) was $82\,nm$.
AttoTEC-532 particles: For coupling $0.5\,mg$ ($0.7\,\mu mol$) of Atto532 NHS esther and $1\,\mu l$ of APS were dissolved in $100\,\mu l$ of absolute ethanol. The mixture was stirred and allowed to react overnight in the dark. The fluorescent shell was grown by the batch technique ([39]). The total amount of APS-Dyes reacted overnight was added to a mixture of $50\,\mu l$ of TES ($0.16\,M$ final concentration) in $1.12\,ml$ of ethanol. The reaction was started with the addition of $90\,\mu l$ of ammonia ($1\,M$ final concentration). The amounts of TES and ammonia were selected to obtain particles of about $200\,nm$ diameter. The experimental diameter measured by TEM was $180\,nm$ (10% polydispersity).

Approximately $100\,\mu l$ of the solution was put onto a cover slip. After $\approx 10\,min$ the supernatant was siphoned off and the cover slips washed in clean water.

Fluorescent Layers

Fluorescent layers were created using either poly-vinyl-alcohol (PVA) or glycerol.
PVA: As a stock solution $50mg$ poly-vinyl-alcohol (PVA) was diluted in $\approx 1ml$ of clean water. $1ml$ of the used dyes (Rhodamine-6G, Atto532) at a concentration of $\approx 1\mu M$ was diluted in $20\mu l$ of the PVA stock solution, $\approx 100\mu l$ of which were spin coated onto a clean cover slip at 4000 Rotations per second for 30s. Fluorescent layers were measured to have a thickness of $\approx 1.1\mu m$ at a standard confocal microscope (SP5, Leica, Mannheim).
Glycerol: The used dyes (Rhodamine-6G, Atto532) were the dissolved in pure glycerol ($\approx 99\%$) to a concentration of $\approx 10\mu M$. A drop of the glycerol-dye solution was put betwen two coversplips and pressed together. The solution pouring out at the edges was wiped off. The thickness of the glycerol-layer was measured by a confocal microscope to be $\approx 20\mu m$. To avoid the glycerol-solution to be succed out between the cover slips, the samples had to be frozen to ≈ -1 °Cbefore evacuation of the cryostat.

Quantum Dots

The stock solution of streptavidin-coated Qdots 655 (Tebu-bio GmbH Offenbach) was diluted with Qdots Incubation Buffer (provided with the Qdots in the package) wo an approximate concentration of $10 - 30\,nM$. Bitinylated cover slips were immersed $\approx 100\,\mu l$ of the prepared solution for $\approx 20 - 30\,min$ and then 3 times rinsed with water or PBS. To avoid degradation of the Qdots the cover slips were kept sonstanly covered with a drop of water during the experiments.

A.1.2 Cell culture and immunocytochemistry

Protocols were used as described by [40]. PtK2 (kidney of adult male rat kangaroo (Potorous tridactylus), epithelial cell line) cells were grown in DMEM high glucose with Glutamax containing 10% FBS, 2% penicillin ($100\,Units/ml$), streptomycin ($100\,mg/ml$) and $1\,mM$ sodium pyruvate. Cells were harvested with trypsin-EDTA (0.05%in PBS) and seeded on standard glass coverslips (diameter $10\,mm$) with a confluency of $50 - 80\%$.

After 24 hours cells were fixed in icecold methanol (-20 °C) followed by several PBS washes. Unspecific binding sites were blocked with PBS containing 1% BSA (Bovine Serum Albumin) for 5 minutes. Cells were incubated with primary antibodies (Mouse Anti-ß-Tubulin IgG (Chemicon International), $1\ \mu g/ml$; Monoclonal mouse Anti-ß-Actin IgG (Sigma), $1\ \mu g/ml$). After 1 h of incubation, cells were washed with PBS with 1% BSA and incubated with secondary antibodies (Sheep Atto532 anti-mouse IgG (H+L) (Jackson Immuno Research, Attotec), $2-5\ \mu g/ml$) for $1\ h$. For imaging cells were mounted in mowiol on top of a second coverslip (diameter $20\ mm$).

A.2 Derivations

A.2.1 Point spread function

Due to the wave nature of light, light passing through a small apterture (radius a) is diffracted and forms a pattern of light and dark regions on a screen some distance (L) away from the aperture (see figure A.2). It has a bright region in the center, known as the Airy disc which together with a series of concentric rings is called the Airy pattern. The diameter of this disc is related to the wavelength of the illuminating light and the size of the circular aperture. Its intensity distribution is described is given by:

$$I(r) = I_0 \left(\frac{2J_1(ka\, r/L)}{ka\, r/L} \right)^2 \quad I(\theta) = I_0 \left(\frac{2J_1(ka \tan\theta)}{ka \tan\theta} \right)^2 \tag{A.1}$$

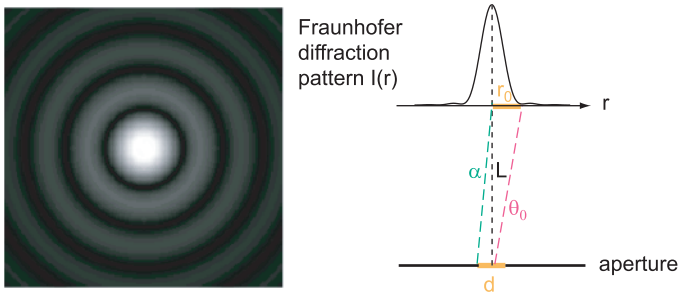

Figure A.2: Fraunhofer diffraction patter of a small aperture

J_1 is a Bessel function of the first kind of order one, a is the radius of the aperture (and d the diameter of the aperture), I_0 is the intensity in the center of the diffraction pattern, and $k = 2\pi/\lambda$ is the wavenumber. The parameter r is the radial distance from the center of the Airy disc and L the distance of the aperture from the screen where the diffraction pattern is observed. Another possible parameter is θ, which is the angle between the axis trough the airy disc and the line from the center of the aury disc to the position r ($tan(\theta) = r/L$). The zeros of $J_1(x)$ are at $x = kar/L = ka \sin\theta \approx 0, 3.832, 7.016, 10.173, 13.324, \cdots$. The first dark ring in the diffraction pattern occurs where

$$k \cdot a \cdot \tan(\theta_0) = 3.832$$

This leads to:

$$\begin{aligned} \tan\theta_0 &= \frac{3.83}{k \cdot a} = \frac{3.83}{\frac{2\pi}{\lambda}a} \\ &= 1.22\frac{\lambda}{2a} = 1.22\frac{\lambda}{d} \end{aligned} \tag{A.2}$$

This equation gives a relationship between the size d of the aperture and the angle θ_0 under which the first minimum of the airy disc occurs. The Rayleigh criterium states that in order to resolve two points one has to be in the first minimum of the Fraunhofer diffration pattern, leading to resolution Δx being defined as the distance r_0 (see figureairy), with $a/L = \tan\alpha \approx \sin\alpha$ and α the half-aperture-angle .

$$\begin{aligned} d &= 2L \cdot \sin\alpha \\ L \cdot \tan\theta_0 \sin\alpha &= 1.22 \cdot \lambda \\ &\text{leading to :} \\ \Delta x = r &= 0.61 \cdot \frac{\lambda}{\sin\alpha} \end{aligned} \tag{A.3}$$

This distance Δx is known as the diffraction limit by Abbe.

A.2.2 RESOLFT rate equations

For the concept of RESOLFT a reversible saturable optical transition between two states is needed. These two states shall be state A and state B.
The transition from A to B is light driven with the rate $k_{AB} = \sigma \cdot I$, with I the intensity of the illumination light and σ the absorption cross-section. The backtransition - whether light or heat induced or spontaneous - happens with rate k_{BA}. The rate equation for the number of molecules in each state N_A and N_B for this system are:

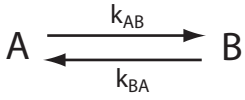

$$\begin{aligned} \dot{N}_A &= -\dot{N}_B = -k_{AB} \cdot N_A + k_{BA} \cdot N_B \\ N_A &+ N_B = 1 \end{aligned} \tag{A.4}$$

After a certain time $t > (k_{AB} + k_{BA})^{-1}$ this system will have reached a dynamical equilibrium at (as much molcules entering each state as are leaving it):

$$\begin{aligned} N_A^\infty &= \frac{k_{BA}}{k_{AB} + k_{BA}} \\ N_B^\infty &= \frac{k_{AB}}{k_{AB} + k_{BA}} \end{aligned} \tag{A.5}$$

At the so-called saturation intensity $I_0 = k_{BA}/\sigma$ the probability to be in either state is equal $N_A^\infty = N_B^\infty = 1/2$. If the illumination intensity is further increased, the population is shifted from state A to state B: $N_A^\infty \to 0$.

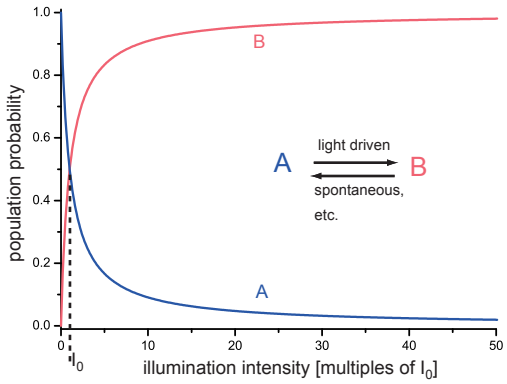

Figure A.3: Population of states A and B depending on the illumination intensity

A.2.3 RESOLFT resolution equation

The extended equation 2.4 for enhanced resolution from chapter 2.1 will be derived in the follwoing section (for details see[7]). The necessary intensity distribution featuring zero intensity at at least one point $I(x_i) = 0$ is in one dimension best achieved by a standing wave like :

$$I(x) = I_{max} \cdot \sin^2(2\pi n(x - x_i)/\lambda)$$

For simplicity the zero intensity will be chosen at $x_c = 0$. I_{max} is the maximal applied intensity, λ the wavelength of the illumination light and n the refractive index. When the dye molecules are illuminated with such a distribution the population of the states A and B in dependence on the position x will be as follows:

$$\begin{aligned} N_B^\infty(x) = 1 - N_A^\infty(x) &= \frac{1}{1 + \frac{k_{BA}}{\sigma \cdot I(x)}} \\ &= \frac{1}{1 + \frac{I_0}{I_{max} \cdot \sin^2(2\pi n x/\lambda)}} \end{aligned} \tag{A.6}$$

with $I_0 = K_{BA}/\sigma$. When B is the fluorescent state, the fluorescence $F(x)$ is proportional to the population of B: $F(x) \propto N_B^\infty(x)$ and the FWHM is determined at the positions $x_{0.5}$, where the fluorescence is half of the maximal possible fluorescence:

$$
\begin{aligned}
F(x_{0.5}) = F_{max}/2 &= F_{max} \cdot N_B^{\infty}(x_{0.5}) \\
\frac{1}{2} &= \frac{1}{1 + \frac{I_0}{I_{max} \cdot \sin^2(2\pi n x_{0.5}/\lambda)}} \\
\sin^2(2\pi n x_{0.5}/\lambda) &= \frac{I_0}{I_{max}} \\
x_{0.5} &= \frac{\lambda}{2\pi n} \cdot \arcsin\sqrt{\frac{I_0}{I_{max}}}
\end{aligned}
\tag{A.7}
$$

When very high intensities are applied the fraction under the squareroot will become very small $\sqrt{\frac{I_0}{I_{max}}} \overset{I_{max} \gg I_0}{\longrightarrow} 0$, allowing the use of the small-angle-approximation $\sin(x) \approx x$:

$$
\begin{aligned}
x_{0.5} &\approx \frac{\lambda}{2\pi n} \cdot \sqrt{\frac{I_0}{I_{max}}} \\
&\Longrightarrow \\
FWHM &\approx 2 \cdot x_{0.5} = \frac{\lambda}{\pi n} \cdot \sqrt{\frac{I_0}{I_{max}}}
\end{aligned}
\tag{A.8}
$$

As the sample has to be illuminated through the objective lense (or any other lense), the wavelength of the illumination pattern is larger than the wavelenght of the illumination light itself. The smallest possible wavelength is determined by the numerical aperture of the lense, that is the half aperture angle α. Therefore λ in equation A.8 has to be replaced by $\lambda/\sin(\alpha)$:

$$
FWHM \approx \frac{\lambda}{\pi n \sin\alpha \cdot \sqrt{\frac{I_{max}}{I_0}}} \tag{A.9}
$$

which is the adapted equation 2.4 from chapter 2.1.

A.2.4 Three state rate equations and steady state levels

The complete three state rate equations including the vibrationally excited states are:

$$
\begin{aligned}
\dot{S}_0(t) &= -k_{ex} \cdot S_0(t) + k_{vib} \cdot S_0^{vib}(t) \\
\dot{S}_0^{vib}(t) &= -k_{vib} \cdot S_0^{vib}(t) + (k_{em} + k_{nf}\cdot) S_1(t) + k_T \cdot T_1(t) \\
\dot{S}_1(t) &= -(k_{em} + k_{nf}) \cdot S_1(t) - k_{ISC} \cdot S_1(t) + k_{vib} \cdot S_1^{vib}(t) \\
\dot{S}_1^{vib}(t) &= k_{ex} \cdot S_0(t) - k_{vib} \cdot S_1^{vib}(t) \\
\dot{T}_1(t) &= k_{vib} \cdot T_1^{vib}(t) - k_T \cdot T_1(t) \\
\dot{T}_1^{vib}(t) &= -k_{vib} \cdot T_1^{vib}(t) + k_{ISC} \cdot S_1(t) \\
S_0(t) + S_0^{vib}(t) + S_1(t) + S_1^{vib}(t) + T_1(t) + T_1^{vib}(t) &= 1
\end{aligned}
\tag{A.10}
$$

As vibrational relaxation k_{vib} is a very fast process ($\tau_{vib} \prec \tau_{em}, \tau_T$) this equations can be simplified setting the vibrationally excited states $S_0^{vib}, S_1^{vib}, T_1^{vib} \cong 0$, which leads to:

$$
\begin{aligned}
\dot{S}_0(t) &= -k_{ex} \cdot S_0(t) + (k_{em} + k_{nf}) \cdot S_1(t) + k_T \cdot T_1(t) \\
\dot{S}_1(t) &= k_{ex} \cdot S_0(t) - (k_{em} + k_{nf}) \cdot S_1(t) - k_{ISC} \cdot S_1(t) \\
\dot{T}_1(t) &= k_{ISC} \cdot S_1(t) - k_T \cdot T_1(t), \\
S_0(t) + S_1(t) + T_1(t) &= 1
\end{aligned}
\tag{A.11}
$$

The steady state case, with $\dot{S}_0 = \dot{S}_1 = \dot{T}_1 = 0$ leads to the steady state levels:

$$
\begin{aligned}
S_0^{SS} &= \frac{(k_{em} + k_{nf} + k_{ISC}) \cdot k_T}{k_{ex} \cdot (k_T + k_{ISC}) + (k_{em} + k_{nf}) \cdot k_T + k_{ISC} \cdot k_T} \\
S_1^{SS} &= \frac{k_{ex} \cdot k_T}{k_{ex} \cdot (k_T + k_{ISC}) + (k_{em} + k_{nf}) \cdot k_T + k_{ISC} \cdot k_T} \\
T_1^{SS} &= \frac{k_{ISC} \cdot k_{ex}}{k_{ex} \cdot (k_T + k_{ISC}) + (k_{em} + k_{nf}) \cdot k_T + k_{ISC} \cdot k_T}
\end{aligned}
\tag{A.12}
$$

No Inter System Crossing

In the case of no inter system crossing $k_{ISC} = 0$, the triplet state T_1 will not be populated and the rate equations result in:

$$
\begin{aligned}
\dot{S}_0(t) &= -k_{ex} \cdot S_0(t) + (k_{em} + k_{nf}) \cdot S_1(t) \\
\dot{S}_1(t) &= k_{ex} \cdot S_0(t) - (k_{em} + k_{nf}) \cdot S_1(t) \\
S_0(t) + S_1(t) &= 1
\end{aligned}
\tag{A.13}
$$

And the steady state equations are reduced to:

$$
\begin{aligned}
S_0^{SS} &= \frac{k_{em} + k_{nf}}{(k_{em} + k_{nf}) + k_{ex}} \\
S_1^{SS} &= \frac{k_{ex}}{(k_{em} + k_{nf}) + k_{ex}}
\end{aligned}
\tag{A.14}
$$

The fluorescence $F \propto S_1$ is proportional to the population of the excited state. With $k_{ex} = \sigma_{ex} \cdot \gamma_{ph} \cdot I$ (σ_{ex} and γ_{ph} cross section for fluorescece excitation and inverse photon energy, respectively), this leads to

$$
F^{SS}(I) \propto S_1 = \frac{1}{1 + \frac{k_{em}+k_{nf}}{\sigma_{ex} \cdot \gamma_{ph} \cdot I}} \tag{A.15}
$$

The mamximum fluorescence value F_{max} on which the population curve converges is:

$$
F_{max} \propto S_1^{max} = \lim_{I \to \infty} \frac{1}{1 + \frac{k_{em}+k_{nf}}{\sigma_{ex} \cdot \gamma_{ph} \cdot I}} = 1 \tag{A.16}
$$

The saturation intensity I_0 is defined as the intensity at which $F^{SS}(I_0) = 1/2 \cdot F_{max}$ or in other terms $S_1^{SS}(I_0) = 1/2 \cdot S_1^{max}$. This leads to:

$$
\begin{aligned}
& F^{SS}(I_0) \propto S_1(I_0) = \frac{1}{1 + \frac{k_{em}+k_{nf}}{\sigma_{ex} \cdot \gamma_{ph} \cdot I_0}} = \frac{1}{2} \\
& \Longrightarrow \\
& I_0^S = \frac{k_{em} + k_{nf}}{\sigma_{ex} \cdot \gamma_{ph}}
\end{aligned}
\tag{A.17}
$$

Using the term for the saturation intensity equation A.15 can be simplified to:

$$
F^S(I) \propto S_1(I) = \frac{1}{1 + \frac{I_0}{I}} \tag{A.18}
$$

With Inter System Crossing

In the case of inter system crossing $k_{ISC} \neq 0$, the steady state fluorescence is derived from the population of S_1^{SS} from equation A.12 results in:

$$
\begin{aligned}
F^{SS}(I) \propto S_1(I) &= \frac{1}{1 + \frac{k_{em}+k_{nf}}{\sigma_{ex} \cdot \gamma_{ph} \cdot I}} \\
&\propto \frac{1}{1 + \frac{k_{ISC}}{k_T} + \frac{k_{em}+k_{nf}+k_{ISC}}{\sigma_{ex} \cdot \gamma_{ph} \cdot I}}
\end{aligned}
\tag{A.19}
$$

The maximum fluorescence is:

$$F_{max} \propto S_1^{max} = \lim_{I\to\infty} \frac{1}{1 + \frac{k_{ISC}}{k_T} + \frac{k_{em}+k_{nf}+k_{ISC}}{\sigma_{ex}\cdot\gamma_{ph}\cdot I}} = \frac{k_T}{k_T + k_{ISC}} < 1 \tag{A.20}$$

and the saturation intensity:

$$\begin{aligned} F^{SS}(I_0) \propto S_1(I_0) &= \frac{1}{1 + \frac{k_{ISC}}{k_T} + \frac{k_{em}+k_{nf}+k_{ISC}}{\sigma_{ex}\cdot\gamma_{ph}\cdot I_0}} = \frac{1}{2}\cdot\frac{k_T}{k_T + k_{ISC}} \\ &\Longrightarrow \\ I_0^S &= \frac{k_T}{k_T + k_{ISC}} \cdot \frac{k_{em} + k_{nf}}{\sigma_{ex}\cdot\gamma_{ph}} \end{aligned} \tag{A.21}$$

Leading to a simplified equation A.19:

$$F^S(I) \propto S_1(I) = \frac{k_T}{k_T + k_{ISC}} \cdot \frac{1}{1 + \frac{I_0}{I}} \tag{A.22}$$

A.2.5 Derivation of fourier coefficients for sinesquare

Non-saturated sinesquare illumination pattern

To understand resolution enhancement due to a sinesquare illumination pattern (as described in section 3.1.1) the fourier transform of the fluorescence emission probability function $F_{prob}(\mathbf{x})$ has to be determined. In the nonsaturated case it is proportional to a sinesquare pattern can be rewritten as a sum of exponential functions or a cosine function:

$$\begin{aligned} F_{prob}(\mathbf{x}) &\propto sin^2(k_I/2\cdot\mathbf{x} + \varphi/2) \\ &= (\frac{\mathrm{e}^{\mathrm{i}\,k_I/2\cdot\mathbf{x}+\varphi/2} - \mathrm{e}^{-\mathrm{i}\,k_I/2\cdot\mathbf{x}-\varphi/2}}{2})^2 \\ &= -\frac{1}{2} + \frac{1}{4}(\mathrm{e}^{\mathrm{i}\,k_I\cdot\mathbf{x}+\varphi} + \mathrm{e}^{-\mathrm{i}\,k_I\cdot\mathbf{x}-\varphi}) \\ &= -\frac{1}{2} + \frac{1}{2}cos(k_I\cdot\mathbf{x} + \varphi) \end{aligned} \tag{A.23}$$

The frequency of the sinesquare pattern was chosen $k_I/2$ and the phase as $\varphi/2$ to simplify the description in fourier space. The fourier transform is defined as:

$$\begin{aligned} \hat{f}(\mathbf{k}) &= \frac{1}{\sqrt{2\pi}}\int_{-\infty}^{\infty} f(\mathbf{x})\cdot\mathrm{e}^{-\mathrm{i}\,\mathbf{k}\cdot\mathbf{x}}d\mathbf{x} \\ f(\mathbf{x}) &= \frac{1}{\sqrt{2\pi}}\int_{-\infty}^{\infty} \hat{f}(\mathbf{k})\cdot\mathrm{e}^{+\mathrm{i}\,\mathbf{x}\cdot\mathbf{k}}d\mathbf{k} \end{aligned} \tag{A.24}$$

Therefore the fourier transfrom of the sinesquare is:

$$\begin{aligned}
\hat{F}_{prob}(\mathbf{k}) &= FT(F_{prob}(\mathbf{x})) \\
&= \frac{1}{\sqrt{2\pi}} \int_{-\infty}^{\infty} (-\frac{1}{2} + \frac{1}{4}(\mathrm{e}^{\mathrm{i}\, k_I \cdot \mathbf{x} + \varphi} + \mathrm{e}^{-\mathrm{i}\, k_I \cdot \mathbf{x} - \varphi})) \cdot \mathrm{e}^{-\mathrm{i}\, \mathbf{k} \cdot \mathbf{x}} d\mathbf{x} \\
&= \frac{1}{\sqrt{2\pi}} \int_{-\infty}^{\infty} -\frac{1}{2} \cdot \mathrm{e}^{-\mathrm{i}\, \mathbf{k} \cdot \mathbf{x}} d\mathbf{x} \\
&\quad + \frac{1}{\sqrt{2\pi}} \int_{-\infty}^{\infty} \frac{1}{4} \mathrm{e}^{\mathrm{i}\, k_I \cdot \mathbf{x} + \varphi} \cdot \mathrm{e}^{-\mathrm{i}\, \mathbf{k} \cdot \mathbf{x}} d\mathbf{x} + \frac{1}{\sqrt{2\pi}} \int_{-\infty}^{\infty} \frac{1}{4} \mathrm{e}^{-\mathrm{i}\, k_I \cdot \mathbf{x} - \varphi} \cdot \mathrm{e}^{-\mathrm{i}\, \mathbf{k} \cdot \mathbf{x}} d\mathbf{x} \\
&= -\frac{1}{2\sqrt{2\pi}} \delta(\mathbf{k}) + \\
&\quad + \frac{1}{4\sqrt{2\pi}} \int_{-\infty}^{\infty} \mathrm{e}^{\mathrm{i}\, (k_I + \mathbf{k}) \cdot \mathbf{x}} \cdot \mathrm{e}^{\mathrm{i}\, \varphi} d\mathbf{x} + \frac{1}{4\sqrt{2\pi}} \int_{-\infty}^{\infty} \mathrm{e}^{-\mathrm{i}\, (k_I - \mathbf{k}) \cdot \mathbf{x}} \cdot \mathrm{e}^{-\mathrm{i}\, \varphi} d\mathbf{x} \\
&= -\frac{1}{2\sqrt{2\pi}} \delta(\mathbf{k}) + \frac{1}{4\sqrt{2\pi}} \delta(\mathbf{k} + k_I) \cdot \mathrm{e}^{+\mathrm{i}\, \varphi} + \frac{1}{4\sqrt{2\pi}} \delta(\mathbf{k} - k_I) \cdot \mathrm{e}^{-\mathrm{i}\, \varphi}
\end{aligned} \tag{A.25}$$

The fourier coefficients of a nonsaturated sinesquare pattern are:

$$\begin{aligned}
c_0 &= -\frac{1}{2\sqrt{2\pi}} \\
c_{+1} &= \frac{1}{4\sqrt{2\pi}} \cdot \mathrm{e}^{+\mathrm{i}\, \varphi} \\
c_{-1} &= \frac{1}{4\sqrt{2\pi}} \cdot \mathrm{e}^{-\mathrm{i}\, \varphi}
\end{aligned} \tag{A.26}$$

Saturated sinesquare illumination pattern

The function that has to be fourier transformed to determine the fourier coefficients of a saturated sinesquare pattern is a saturation curve applied on the sinesquare. Exemplary saturation functions are A.15 for singlet saturation and A.19 for triplet saturation, simplified they have the following form:

$$
\begin{aligned}
F_{prob}^{Ssat}(\mathbf{x}) &\propto \frac{1}{1+\frac{A}{B\cdot I(\mathbf{x})}} \\
&= \frac{1}{1+\frac{A}{B\cdot sin^2(k_I/2\cdot\mathbf{x}+\varphi/2)}}
\end{aligned}
\tag{A.27}
$$

$$
\begin{aligned}
F_{prob}^{Tsat}(\mathbf{x}) &\propto \frac{1}{C+\frac{1}{B\cdot I(\mathbf{x})}} \\
&= \frac{1}{C+\frac{1}{B\cdot sin^2(k_I/2\cdot\mathbf{x}+\varphi/2)}}
\end{aligned}
$$

As the emission probability is a periodic funtion with frequency $\mathbf{k}_I$ and period $D = 2\pi/k_I$ (see figures 3.1 and 3.2 in chpater 3.1.1) it can be written as a fourier series:

$$
\begin{aligned}
F_{prob}(\mathbf{x}) &= \sum_{p=-\infty}^{\infty} s_p \mathrm{e}^{\mathrm{i}\cdot p\cdot k_I \mathbf{x}} \\
&\text{with the coefficients} \\
s_p &= \frac{1}{D}\int_0^D F_{prob}(\mathbf{x})\cdot \mathrm{e}^{-\mathrm{i}\cdot p\cdot k_I \mathbf{x}} d\mathbf{x} \qquad\qquad p \in N
\end{aligned}
\tag{A.28}
$$

Building the fourier transfrom leads to:

$$
\begin{aligned}
\hat{F}_{prob}(\mathbf{k}) &= FT(F_{prob}(\mathbf{x})) \\
&= \frac{1}{\sqrt{2\pi}}\int_{-\infty}^{+\infty}(\sum_{p=-\infty}^{\infty} s_p \mathrm{e}^{\mathrm{i}\cdot p\cdot k_I \mathbf{x}})\cdot \mathrm{e}^{-\mathrm{i}\,\mathbf{k}\cdot\mathbf{x}} d\mathbf{x} \\
&= \frac{1}{\sqrt{2\pi}}\sum_{p=-\infty}^{\infty} s_p \int_{-\infty}^{+\infty} \mathrm{e}^{\mathrm{i}\cdot(p\cdot k_I-\mathbf{k})\mathbf{x}} d\mathbf{x} \\
&= \sum_{p=-\infty}^{\infty} \frac{s_p}{\sqrt{2\pi}}\delta(p\cdot k_I - \mathbf{k})
\end{aligned}
\tag{A.29}
$$

This leads directly to function 3.13:

$$
\begin{aligned}
\hat{F}_{prob}(\mathbf{k}) &= \sum_n c_n \cdot \delta(n\cdot \mathbf{k}_I) \qquad\qquad n \in Z \\
&\text{with} \\
c_n &:= \frac{s_n}{\sqrt{2\pi}} \\
&= \frac{1}{\sqrt{2\pi}D}\int_0^D F_{prob}(\mathbf{x})\cdot \mathrm{e}^{-\mathrm{i}\cdot n\cdot k_I \mathbf{x}} d\mathbf{x}
\end{aligned}
\tag{A.30}
$$

The fourier coefficients of emission probability functions A.27 do not have analytical solutions, but can be determined numerically.

A.2.6 Derivation of the pump-probe characteristics

Three-state steady-state populations of S_0, S_1 and T_1:

$$\begin{aligned} S_0^{SS} &= \frac{(k_{10} + k_{ISC}) \cdot k_T}{(k_{10} + k_{ISC}) \cdot k_T + k_{ex,pump} \cdot (k_T + k_{ISC})} \\ S_1^{SS} &= \frac{k_{ex,pump} \cdot k_T}{(k_{10} + k_{ISC}) \cdot k_T + k_{ex,pump} \cdot (k_T + k_{ISC})} \\ T_1^{SS} &= \frac{k_{ISC} \cdot k_{ex,pump}}{(k_{10} + k_{ISC}) \cdot k_T + k_{ex,pump} \cdot (k_T + k_{ISC})} \end{aligned} \tag{A.31}$$

with k_{10} the singlet deexcitation rate, k_{ISC} ISC rate, k_T triplet relaxation rate and $k_{ex,pump} = \sigma_{ex} \cdot \gamma_{ph} \cdot I_{pump}$ the excitation rate (σ_{ex} and γ_{ph} cross section for fluorescence excitation and inverse photon energy, respectively). Right after the exposure to the pump pulse the molecules in the first excited singlet state S_1 decay to the ground state S_0 within ns ($k_{10} \approx 10^9\ \frac{1}{s}$), whereas the molecules in the triplet state T_1 do not have time to relax to the ground state ($k_T \approx\ \frac{1}{s} \prec k_{10}$), leading to the following populations:

$$\begin{aligned} S_0^{\text{after pump}} &= \frac{(k_{10} + k_{ISC} + k_{ex}) \cdot k_T}{(k_{10} + k_{ISC}) \cdot k_T + \sigma_{ex} \cdot \gamma_{ph} \cdot I_{pump} \cdot (k_T + k_{ISC})} \\ S_1^{\text{after pump}} &= 0 \\ T_1^{\text{after pump}} &= T_1^{SS} = \frac{k_{ISC} \cdot \sigma_{ex} \cdot \gamma_{ph} \cdot I_{pump}}{(k_{10} + k_{ISC}) \cdot k_T + \sigma_{ex} \cdot \gamma_{ph} \cdot I_{pump} \cdot (k_T + k_{ISC})} \end{aligned} \tag{A.32}$$

The peak fluorescence F resulting from illumination with the probe pulse (I_{probe}) can only stem from the molecules in the singlet system:

$$\begin{aligned} F &\propto k_{ex,probe} \cdot S_0^{\text{after pump}} \\ &\propto I_{probe} \cdot S_0^{\text{after pump}} \end{aligned} \tag{A.33}$$

The fluorescence saturation level F_{sat} is determined by the population of the singlet / triplet state after the pump pulse:

$$
\begin{aligned}
F_{sat} &= \lim_{I_{pump}\to\infty} F(I_{pump}) \\
&\propto \lim_{I_{pump}\to\infty} \left(1 - T_1^{SS}\right) \\
&\propto \lim_{I_{pump}\to\infty} \left(1 - \frac{k_{ISC}\cdot\sigma_{ex}\cdot\gamma_{ph}\cdot I_{pump}}{(k_{10}+k_{ISC})\cdot k_T + \sigma_{ex}\cdot\gamma_{ph}\cdot I_{pump}\cdot(k_T+k_{ISC})}\right) \\
&\propto \left(1 - \frac{k_{ISC}}{k_{ISC}+k_T}\right) = \frac{k_T}{k_{ISC}+k_T}
\end{aligned}
\tag{A.34}
$$

I_0 can be calculated from the rate equations 3.20 as:

$$
I_0 = \frac{k_T}{k_T + k_{ISC}} \cdot \frac{k_{10}+k_{ISC}}{\sigma_{ex}\cdot\gamma_{ph}} \tag{A.35}
$$

which leads to the simplification:

$$
\begin{aligned}
F(I_{pump}) &\propto \frac{1}{1+\frac{I_{pump}}{I_0}} + \frac{k_T}{k_T+k_{ISC}} \cdot \frac{1}{1+\frac{I_0}{I_{pump}}} \\
&\propto \left(1 - \frac{k_T}{k_T+k_{ISC}}\right) \cdot \frac{1}{1+\frac{I_{pump}}{I_0}} + \frac{k_T}{k_T+k_{ISC}}
\end{aligned}
\tag{A.36}
$$

A.2.7 Derivation of the plateau fluorescence with reverse ISC

The plateau fluorescence – the steady state fluorescence of beads labeled with Atto532 at vacuum conditions and $80\ K$ was simulated with the use of Labview (National Instruments Germany GmbH, Muenchen, Germany) and a system of extended rate equations including reverse ISC:

$$
\begin{aligned}
\dot{S}_0(t) &= -k_{ex}\cdot S_0(t) + k_{10}\cdot S_1(t) + k_T\cdot T_1(t) \\
\dot{S}_1(t) &= k_{ex}\cdot S_0(t) - k_{10}\cdot S_1(t) - k_{ISC}\cdot S_1(t) + k_{T1->Tn}\cdot\Phi_{revISC}\cdot T_1(t) \\
\dot{T}_1(t) &= k_{ISC}\cdot S_1(t) - k_T\cdot T_1(t) - k_{T1->Tn}\cdot\Phi_{revISC}\cdot T_1(t) \\
S_0(t) &+ S_1(t) + T_1(t) = 1
\end{aligned}
\tag{A.37}
$$

The parameters are chosen as before, the additional excitation rate from $T_1 \rightarrow T_n$ is given by $k_{T1->Tn} = \sigma_{T1->Tn}\cdot\gamma_{ph}\cdot I$ with $\sigma_{T1->Tn}$ the excitation cross-section for $T_1 \rightarrow T_n$ and the parameter Φ_{revISC} determines the probability for reverse ISC, as the triplet state T_n can be deexcited via different channels, one of which is reverse ISC and relaxation to S_1 and finally S_0. The steady-state solutions are:

$$S_0^{SS} = \frac{k_{10} \cdot (k_T + k_{T1->Tn} \cdot \Phi_{revISC}) + k_T \cdot k_{ISC}}{k_{ex} \cdot (k_T + k_{T1->Tn} \cdot \Phi_{revISC}) + k_{10} \cdot (k_T + k_{T1->Tn} \cdot \Phi_{revISC}) + k_T \cdot k_{ISC} + k_{ex} \cdot k_{ISC}}$$
$$S_1^{SS} = \frac{k_{ex} \cdot (k_T + k_{T1->Tn} \cdot \Phi_{revISC})}{k_{ex} \cdot (k_T + k_{T1->Tn} \cdot \Phi_{revISC}) + k_{10} \cdot (k_T + k_{T1->Tn} \cdot \Phi_{revISC}) + k_T \cdot k_{ISC} + k_{ex} \cdot k_{ISC}}$$
$$T_1^{SS} = \frac{k_{ex} \cdot k_{ISC}}{k_{ex} \cdot (k_T + k_{T1->Tn} \cdot \Phi_{revISC}) + k_{10} \cdot (k_T + k_{T1->Tn} \cdot \Phi_{revISC}) + k_T \cdot k_{ISC} + k_{ex} \cdot k_{ISC}} \quad \text{(A.38)}$$

The plateau fluorscence is proportional to the population of S_1, the paramters used for figure A.4 were:

- $\sigma_{ex} \cdot \gamma_{ph} = 1030\, cm^2/J$
  with $\gamma_{532nm} = \frac{\lambda}{h \cdot c} = 2.68 \cdot 10^{18} \frac{1}{J}$ ($\lambda = 532\, nm$, h: Planck´s constant, c: velocity of light)
  and $\sigma_{ex} = 3.85 \cdot 10^{-21} \cdot \epsilon(\lambda)$ and $\epsilon(532nm) \approx 10^5 (M \cdot cm)^{-1}$
- $k_{10} = 5.9 \cdot 10^8 \frac{1}{s}$ (kindly provided by Arnold Giske (personal communication))
- $k_T = 1.4 \frac{1}{s}$ (from figure 3.14 $\tau_T \approx 716\, ms$)
- $k_{ISC} = 3 \cdot 10^6 \frac{1}{s}$ (determined from the momoexponential fit to the fluorescence decay over time which is due to the build-up of triplet population, fitparameter $k_{monoexp} = \frac{k_{ex}}{k_0} \cdot k_{ISC} + k_T$ measured at different intensities (different k_{ex}))

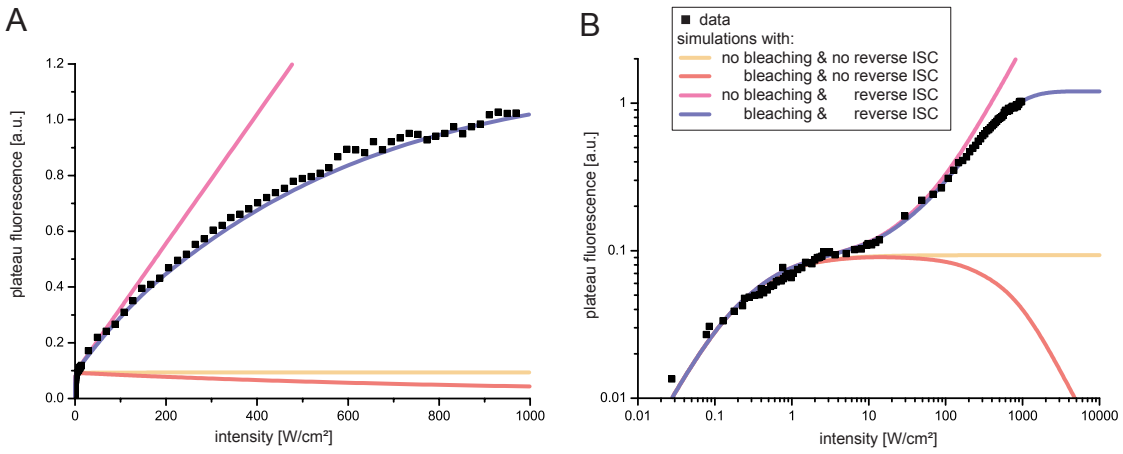

Figure A.4: Plateau saturation for different cases

The black dots in figure A.4 are data points measured for beads labeles with Atto532 at vacuum conditions and $80\, K$. The yellow curve is the population of the fluorescence $F \propto S_1$ with population of the triplet state but without reverse ISC $k_{ISC} = 0$, determined by equation

A.38 and the given parameters. A constant proportionality factor was chosen ("'simulated quantum yield"'), so that the yellow curve overlaid the data points in the inital part of the curve ($I < 2\ W/cm^2$, see logaratihmic representation in part (B)). Above $2\ W/cm^2$ the orange curve did not follow the measured data any more. When reverse ISC was included in the model the deviation from the plateau could be mimicked. The best overlay the data points and the simulation (pink) in the intenstity region from $2\ W/cm^2 - 100\ W/cm^2$ was achieved by choosing

$$\sigma_{T1->Tn} \cdot \gamma_{ph} \cdot \Phi_{revISC} = 0.035 cm^2/J.$$

Above $100\ W/cm^2$ the measured fluorescence was lower than the fluorescence expected from the simulations, which is probably due to photo-bleaching. Therefore a simple bleaching mechanism was added to the simulation, by multiplying the fluorescence with a bleaching functions $f_{bleach} = 1/k_{bleach} \cdot (1 - e^{-k_{bleach} \cdot t_{bleach}})$ and the exposure time $t_{bleach} = 10\ ms$ (as used in the experiment). Bleaching was asumed to occur from the triplet system only with a rate $k_{bleach} = \Phi_{bleach,T1} * T_1$. A bleaching probability of $\Phi_{bleach,T1} = 0.2$ resulted in the best overlay of the simulation and the experimental data (purple). For the sake of completeness fluorescence saturation without reverse ISC but including bleaching is plotted as well (orange). For simulations and fits presented in the previous chapter, the rate constants and photokinetical paramteres given and derived here were used.

A.2.8 Characterization of the fluorescence emission probability pattern

FWHM

The illumination pattern for the depletion light is given by:

$$I(x) = I_{max} \cdot (r + (1 - r) \cdot \sin^2(\pi \cdot x/D))$$

The factor r determines the amount of illumination light in the minimum ($0 < r < 1$). The saturation curve for depletion is:

$$F(I) = 1 - \frac{1}{1 + \frac{I_0}{I}}$$

The combination of these two equations leads to:

$$\begin{aligned} F_{prob}(x) &= 1 - \frac{1}{1 + \frac{I_0}{I_{max} \cdot (r + (1-r) \cdot \sin^2(\pi \cdot x/D))}} \\ &= 1 - \frac{1}{1 + \frac{1}{\xi \cdot (r + (1-r) \cdot \sin^2(\pi \cdot x/D))}} \\ \text{with } \xi &= \frac{I_{max}}{I_0} \end{aligned} \tag{A.39}$$

To determine the full width at half maximum (FWHM) the maximal and minimal fluorescence emission probability have to be known. The maximal fluorescence is at a position, where the illumination intensity is at a minimum, that is, where $x = 0$, and the minimal fluorescence is achieved at position $x = D/2$, leading to:

$$\begin{aligned} F_{prob}^{max} &= \frac{1}{\xi r + 1} \\ F_{prob}^{min} &= \frac{1}{\xi + 1} \\ F_{prob}^{FWHM} &= 1/2 \cdot (F_{prob}^{max} + F_{prob}^{min}) \\ &= \frac{\xi(r+1)+2}{2 \cdot (\xi r + 1) \cdot (\xi + 1)} \end{aligned}$$

The poxition value x_{FWHM} at which the value F_{prob}^{FWHM} is assumed can be determined from the following equation as:

$$F_{prob}(x_{FWHM}) = 1 - \frac{1}{1 + \frac{1}{\xi \cdot (r + (1-r) \cdot \sin^2(\pi \cdot x_{FWHM}/D))}} = \frac{\xi(r+1)+2}{2 \cdot (\xi r + 1) \cdot (\xi + 1)}$$

$$\begin{aligned} x_{FWHM,1} &= \frac{1}{\pi} \arccos\left(\sqrt{\frac{\xi + 1}{\xi(r+1)+2}}\right) \\ x_{FWHM,2} &= \frac{1}{\pi}\left(1 - \arccos\left(\sqrt{\frac{\xi + 1}{\xi(r+1)+2}}\right)\right) \end{aligned}$$

From geometric considerations followsthe full width at half maximum in dependence on the applied intensity and the illumination intensity in the minimum r:

$$FWHM = 2 \cdot x_{FWHM,1} = \frac{2}{\pi} \arccos\left(\sqrt{\frac{\xi + 1}{\xi(r+1)+2}}\right) \tag{A.40}$$

This relationship was used to plot the graphs for FWHM in chapter 4.3.1.

Maximum

The fluorescence in the mimina of the depletion pattern is the highest possible fluorescence. It occurs at those positions, where the $\sin^2(\pi \cdot x/D)$ is zero:

$$\begin{aligned} F_{max} = F_{prob}(0) &= 1 - \frac{d}{1 + \frac{I_0}{I_{max} \cdot (r + (1-r) \cdot 0)}} \\ &= 1 - \frac{d}{1 + \frac{I_0}{I_{max} \cdot r}} \\ &= \frac{\frac{I_{max}}{I_0} \cdot r \cdot (1-d) + 1}{\frac{I_{max}}{I_0} \cdot r + 1} \end{aligned} \tag{A.41}$$

The incomplete depletion is characterized by the parameter d.

Minimum

The fluorescence in the maxima of the depletion pattern is the lowest possible fluorescence. It occurs at those positions, where the $\sin^2(\pi \cdot x/D)$ is 1:

$$\begin{aligned} F_{min} = F_{prob}(1) &= 1 - \frac{d}{1 + \frac{I_0}{I_{max} \cdot (r + (1-r) \cdot 1)}} \\ &= 1 - \frac{d}{1 + \frac{I_0}{I_{max} \cdot 1}} \\ &= \frac{\frac{I_{max}}{I_0} \cdot (1-d) + 1}{\frac{I_{max}}{I_0} + 1} \end{aligned} \tag{A.42}$$

The incomplete depletion is characterized by the parameter d.

Difference of Maximum and Minimum

The difference of fluorescence mimina and minima is:

$$\begin{aligned} F_{diff} &= F_{max} - F_{min} \\ &= \frac{\frac{I_{max}}{I_0} \cdot d \cdot (1-r)}{(\frac{I_{max}}{I_0} \cdot r + 1) \cdot (\frac{I_{max}}{I_0} + 1)} \end{aligned} \tag{A.43}$$

The incomplete depletion is characterized by the parameter d.

A.3 Spectra

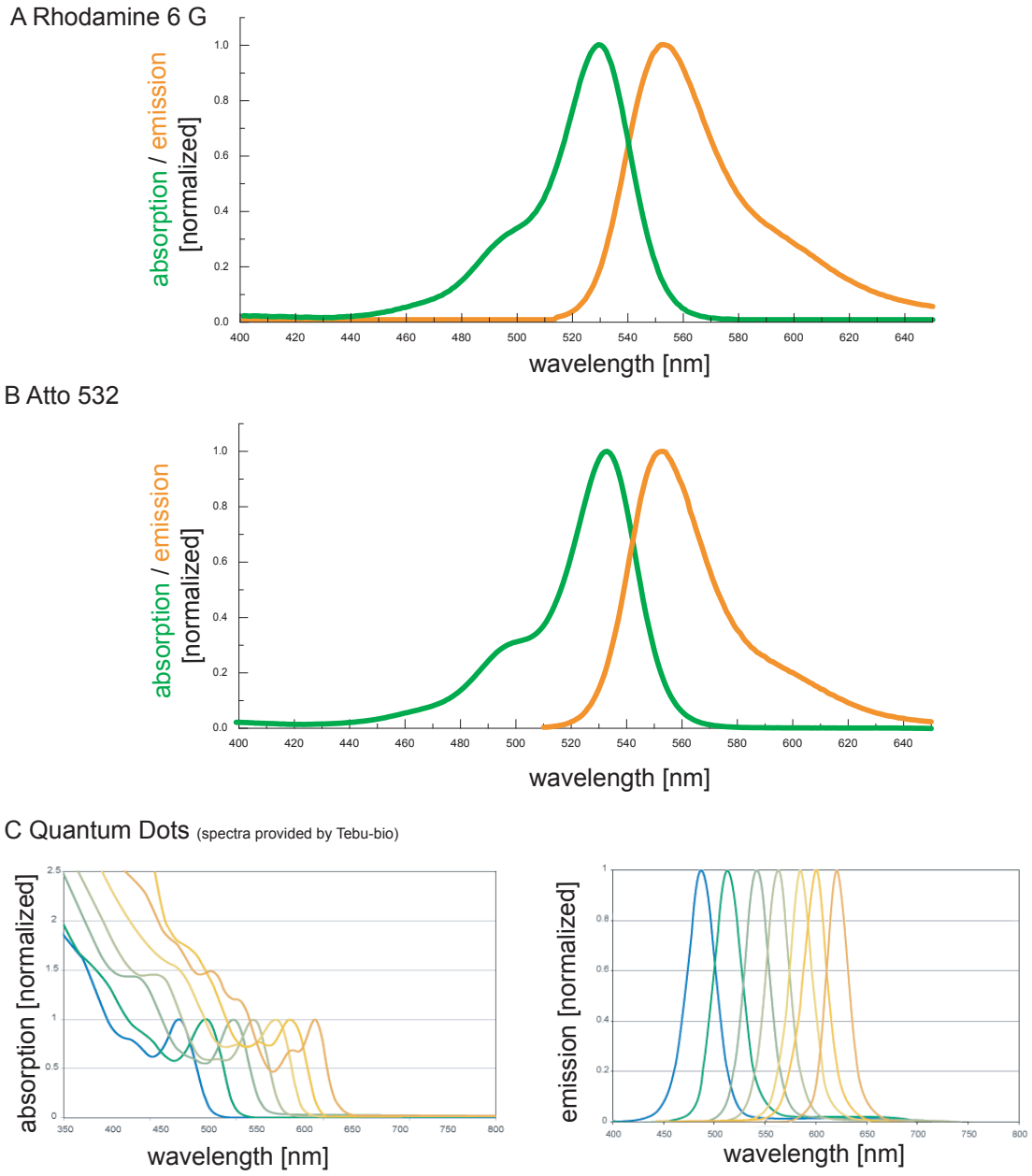

Figure A.5: Absorption and Emission Spectra some of the used dyes, **(A):** Rhodamine 6G in ethanol, **(B):** Atto 532 in water, **(C):** CdSe/ZnSe Evidot Quantum Dots

Glossary

AFM	**A**tomic **F**orce **M**icroscopy [4]
APD	**A**valanche **P**hoto **D**iode
APS	(3-aminopropyl)triethoxysilane
EM	**E**lectron **M**icroscopy [3]
FWHM	**F**ull **W**idth at **H**alf **M**aximum
FT	**F**ourier **T**ransform
GSD	**G**round **S**tate **D**epletion
ISC	**I**nter-**S**ystem **C**rossing
IC	**I**nternal **C**onversion
NA	**N**umerical **A**perture
OTF	**O**ptical **T**ransfer **F**unction
PALM	PhotoActivation Localization Microscopy
PSF	**P**oint **S**pread **F**unction
revISC	**rev**erse **I**nter-**S**ystem **C**rossing
RESOLFT	**R**eversible **S**aturable **O**ptical (**F**luorescence) **T**ransitions
SNOM	**S**canning **N**ear-Field **O**ptical **M**icroscopy
STED	**ST**imulated **E**mission **D**epletion
TEM	**T**ransmission **E**lectron **M**icroscopy

Bibliography

[1] E. Abbe. Belträge zur Theorie des Mikroskops and der mikroskopischen Wahmehmung. *Schultzes Archiv Mikr Anat*, pages 413–468, 1873.

[2] K. Konig, Y. Tadir, P. Patrizio, M.W. Berns, and B.J. Tromberg. Andrology: Effects of ultraviolet exposure and near infrared laser tweezers on human spermatozoa. *Human Reproduction*, 11(10):2162, 1996.

[3] S. Wischnitzer. *Introduction to electron microscopy*. Pergamon Press New York, 1970.

[4] G. Binnig, CF Quate, and C. Gerber. Atomic Force Microscope. *Physical Review Letters*, 56(9):930–933, 1986.

[5] D.W. Pohl and D. Courjon. Near field optics. 1993.

[6] JB Pawley and B.R. Masters. Handbook of Biological Confocal Microscopy. *Optical Engineering*, 35:2765, 1996.

[7] SW Hell, KI Willig, M. Dyba, S. Jakobs, L. Kastrup, and V. Westphal. Nanoscale Resolution with Focused Light: STED and Other RESOLFT Microscopy Concepts. *Handbook of Biological Confocal Microscopy, edited by James B. Pawley*, pages 571–579, 2006.

[8] SW Hell, S. Jakobs, and L. Kastrup. Imaging and writing at the nanoscale with focused visible light through saturable optical transitions. *Applied Physics A: Materials Science & Processing*, 77(7):859–860, 2003.

[9] V. Westphal and S.W. Hell. Nanoscale Resolution in the Focal Plane of an Optical Microscope. *Physical Review Letters*, 94(14):143903, 2005.

[10] S.W. Hell. Toward fluorescence nanoscopy. *Nature Biotechnology*, 21(11):1347–1355, 2003.

[11] S.W. Hell and J. Wichmann. Breaking the diffraction resolution limit by stimulated emission: stimulated-emission-depletion fluorescence microscopy. *Opt. Lett*, 19(11):780–782, 1994.

[12] T.A. Klar, S. Jakobs, M. Dyba, A. Egner, and S.W. Hell. Fluorescence microscopy with diffraction resolution barrier broken by stimulated emission. *Proceedings of the National Academy of Sciences*, 97(15):8206–8210, 2000.

[13] V. Westphal, L. Kastrup, and SW Hell. Lateral resolution of 28 nm (?/25) in far-field fluorescence microscopy. *Applied Physics B: Lasers and Optics*, 77(4):377–380, 2003.

[14] M. Bossi, J. Fölling, M. Dyba, V. Westphal, and S.W. Hell. Breaking the diffraction resolution barrier in far-field microscopy by molecular optical bistability. *New Journal of Physics*, 8:275, 2006.

[15] M. Hofmann, C. Eggeling, S. Jakobs, and S.W. Hell. Breaking the diffraction barrier in fluorescence microscopy at low light intensities by using reversibly photoswitchable proteins. *Proceedings of the National Academy of Sciences*, 102(49):17565–17569, 2005.

[16] M.A. Schwentker, H. Bock, M. Hofmann, S. Jakobs, J. Bewersdorf, C. Eggeling, and S.W. Hell. Wide-field sub-diffraction RESOLFT microscopy using fluorescent protein photoswitching. *Micr. Res. Tech.*, 70(3):269–280, 2007.

[17] SW Hell and M. Kroug. Ground-state-depletion fluorscence microscopy: A concept for breaking the diffraction resolution limit. *Applied Physics B: Lasers and Optics*, 60(5):495–497, 1995.

[18] R. Zondervan, F. Kulzer, M.A. Kolchenko, and M. Orrit. Photobleaching of Rhodamine 6G in Poly (vinyl alcohol) at the Ensemble and Single-Molecule Levels. *J. Phys. Chem. A*, 108(10):1657–1665, 2004.

[19] S.W. Hell. Increasing the resolution of far-field fluorescence light microscopy by point-spread-function engineering. *Topics in Fluorescence Spectroscopy*, 5:361–422, 1997.

[20] KI Willig, J. Keller, M. Bossi, and SW Hell. STED microscopy resolves nanoparticle assemblies. *New Journal of Physics*, 8(6):106, 2006.

[21] M. Andresen, M.C. Wahl, A.C. Stiel, F. Grater, L.V. Schafer, S. Trowitzsch, G. Weber, C. Eggeling, H. Grubmuller, S.W. Hell, et al. Structure and mechanism of the reversible photoswitch of a fluorescent protein. *Proceedings of the National Academy of Sciences*, 102(37):13070–13074, 2005.

[22] M.G.L. Gustafsson. Nonlinear structured-illumination microscopy: Wide-field fluorescence imaging with theoretically unlimited resolution. *Proceedings of the National Academy of Sciences*, 102(37):13081–13086, 2005.

[23] S. Bretschneider, C. Eggeling, and S.W. Hell. Breaking the diffraction barrier in fluorescence microscopy by optical shelving. *Phys. Rev. Lett.* `accepted`.

[24] M.G.L. Gustafsson, D.A. Agard, and J.W. Sedat. Doubling the lateral resolution of wide-field fluorescence microscopy using structured illumination. *Three-dimensional and multidimensional microscopy: image acquisition and processing VII*, pages 141–150.

[25] F. Kohn, J. Hofkens, R. Gronheid, M. van der Auweraer, and F.C. de Schryver. Parameters influencing the on-and off-times in the fluorescence intensity traces of single cyanine dye molecules. *J. Phys. Chem. A*, 106(19):4808–4814, 2002.

[26] R. Heintzmann, T.M. Jovin, and C. Cremer. Saturated patterned excitation microscopy-a concept for optical resolution improvement. *Journal of the Optical Society of America A*, 19(8):1599–1609, 2002.

[27] R. Heintzmann. Saturated patterned excitation microscopy with two-dimensional excitation patterns. *Micron*, 34(6-7):283–91, 2003.

[28] M.G.L. Gustafsson. Surpassing the lateral resolution limit by a factor of two using structured illumination microscopy. *J. Microsc*, 198:82–87, 2000.

[29] G. Donnert, J. Keller, R. Medda, M.A. Andrei, S.O. Rizzoli, R. Luhrmann, R. Jahn, C. Eggeling, and S.W. Hell. Macromolecular-scale resolution in biological fluorescence microscopy. *Proceedings of the National Academy of Sciences*, 103(31):11440, 2006.

[30] G. Donnert, C. Eggeling, and S.W. Hell. Major signal increase in fluorescence microscopy through dark-state relaxation. *Nature Methods*, 4:81–86, 2006.

[31] J. Widengren, U. Mets, and R. Rigler. Fluorescence correlation spectroscopy of triplet states in solution: a theoretical and experimental study. *The Journal of Physical Chemistry*, 99(36):13368–13379, 1995.

[32] M. Nagorni and S.W. Hell. 4Pi-confocal microscopy provides three-dimensional images of the microtubule network with 100-to 150-nm resolution. *J. Struct. Biol*, 123:236–247, 1998.

[33] MGL Gustafsson, DA Agard, and JW Sedat. I 5 M: 3D widefield light microscopy with better than 100 nm axial resolution. *J. Microsc*, 195(1):10–16, 1999.

[34] R. Zondervan, F. Kulzer, H. van der Meer, J.A.J.M. Disselhorst, and M. Orrit. Laser-Driven Microsecond Temperature Cycles Analyzed by Fluorescence Polarization Microscopy. *Biophysical Journal*, 90(8):2958–2969, 2006.

[35] E. Betzig, G.H. Patterson, R. Sougrat, O.W. Lindwasser, S. Olenych, J.S. Bonifacino, M.W. Davidson, J. Lippincott-Schwartz, and H.F. Hess. Imaging Intracellular Fluorescent Proteins at Nanometer Resolution. *Science*, 313(5793):1642, 2006.

[36] K. Osseo-Asare and FJ Arriagada. Preparation of SiO_2 nanoparticles in a non-ionic reverse micellar system. *Colloids and surfaces*, 50:321–339, 1990.

[37] FJ Arriagada and K. Osseo-Asare. Synthesis of Nanosize Silica in a Nonionic Water-in-Oil Microemulsion: Effects of the WaterSurfactant Molar Ratio and Ammonia Concentration. *Journal of Colloid and Interface Science*, 211(2):210–220, 1999.

[38] GH Bogush, M. Tracy, and IV Zukoski. Preparation of Monodisperse Silica Particles: Control of Size and Mass Fraction. *J. Non-Cryst. Solids*, 104:95106, 1988.

[39] A. Van Blaaderen and A. Vrij. Synthesis and characterization of colloidal dispersions of fluorescent, monodisperse silica spheres. *Langmuir*, 8(12):2921–2931, 1992.

[40] M. Osborn, W.W. Franke, and K. Weber. Visualization of a System of Filaments 7-10 nm Thick in Cultured Cells of an Epithelioid Line (Pt K2) by Immunofluorescence Microscopy. *Proceedings of the National Academy of Sciences*, 74(6):2490–2494, 1977.

**VIELE MENSCHEN HABEN MIR GEHOLFEN UND MICH UNTERSTÜTZT.
STELLVERTRETEND MÖCHTE ICH DANKEN:**

Prof Stefan Hell für die Möglichkeit, dieses Projekt durchzuführen,
und seinen ansteckenden Enthusiasmus für die Physik im Allgemeinen und
insbesondere für unsere Arbeit.

Prof Josef Bille für seinen Einsatz als Gutachter und Prüfer
und dafür, mich schon während des Studiums für die Optik zu interessieren.

Prof Iring Bender und Prof Rainer Fink für ihre unkomplizierte Bereitschaft,
mich zu prüfen.

Christian Eggeling für die Antworten auf meine Fragen,
die vielen lehrreichen Diskussion
und alle verständnisvollen Momente.

Jörg Bewersdorf für die Einarbeitung in die Optik und seine humorvolle Sicht auf
die Arbeit und das Leben.

Norbert Quaas und Arnold Giske für die Hilfe mit Vakuum- und Kältetechnik.
(Auch wenn das bei uns weder ein Vakuum noch richtig kalt ist.)

Andreas Schönle für Imspector und Unmengen von Diskussionen über den Fourierraum
und das Elterngeld.

Rebecca Medda und Silvia Löbermann für die Präparation der Zellen
und viele musikalische Momente.

Brian Rankin und Chaitanya Ullal für die viele Mühe mit dem Korrekturlesen.

der ganzen Gruppe für verständnisvolles Zuhören, fachliche Diskussionen
und den vielen Spaß.

meinen Eltern, denen ich so vieles verdanke.

Björn für alles.
(Du willst ja nur der Herr Doktor sein.)